INTERACTION AND SELF-ASSEMBLY OF NANOPARTICLES FOR BIOMEDICAL, NANODEVICE, AND MATERIAL APPLICATIONS

by

Jong Hyun Park

A dissertation submitted in partial fulfillment
of the requirements for the degree of
Doctor of Philosophy
(Mechanical Engineering)
in The University of Michigan
2009

Doctoral Committee:

Associate Professor Wei Lu, Chair
Professor Jwo Pan
Associate Professor Lingjie Jay Guo
Assistant Professor Samantha Hayes Daly

2009

ACKNOWLEDGEMENTS

As I write the draft of my thesis, I have looked back on the past years and many pictures came and went in my eyes. Among the many people who made it possible for me to complete my thesis, I would like to express my deepest gratitude to my advisor, Professor Wei Lu. I had tremendous support from him through his encouragement, inspiration, and invaluable advice in the research. Whenever I was faced with difficulties, he was always there with deep physical insights, sharp eyes, and extensive knowledge of engineering. I learned so many things from him, how to think independently as a scientist and how to develop physical meanings from the problems we had. It is a valuable and an enjoyable experience for me to work with him.

Many thanks must also go to the wonderful professors and lecturers who have helped me during my academic career. Particular thanks go to my dissertation committee, Professor Jwo Pan, Professor Lingjie Jay Guo, and Professor Samantha Daly. I wish to thank Professor Ann Marie Sastry and Dr. Chia-Wei Wang who have given me helpful advice on my research.

Finally, I would like to give my thanks to my parents, sisters, and brothers for their love. Without their love I would not have been able to complete this work.

My love Yeonsin and another love Seoryeong, thank you for being together with me.

Jonghyun Park
Ann Arbor
November, 2008

TABLE OF CONTENTS

LIST OF FIGURES

ABSTRACT

INTERACTION AND SELF-ASSEMBLY OF NANOPARTICLES FOR BIOMEDICAL, NANODEVICE, AND MATERIAL APPLICATIONS

by

Jonghyun Park

Chair: Wei Lu

The goal of this thesis is to investigate the use of nanoparticles as a means of self-assembly into target structures and as candidates for a variety of applications such as advanced materials, nanodevices, and drug delivery systems. In order to achieve and exploit the immense potential of the nanoparticles, the majority of the investigation

introduces an electrostatic field for controlling the behavior of nanoparticles. Materials with a well-organized distribution and an orientation provide superior properties that cannot be achieved by the current uniformly or randomly dispersed nanocomposites. An approach to rigorously calculate the driving force and to predict the behavior of the system may suggest a significant degree of the experimental control and contribute to materialization of the distinguished properties. This work focuses on the behavior of lossless and lossy core-shell nanoparticles, which makes the behavior more complicated but enhances its strength and improves the assembly. Taking into account the thermal motion of the particles, it is possible to investigate the stability, internal structure, and rheological properties of nanoparticle dispersions. Electrostatic interactions also demonstrate that organizing different nanoparticles systematically into ordered binary superlattices can lead to functional materials. The work presented here, through the theoretical and computational investigation, elucidates how parameters including permittivity, volume fraction, particle size, and the frequency of the field can be utilized to control the morphology of the superlattice structures. The study explores rich patterning dynamics and a wide range of superlattices from functional gradient columns to an alternating chain-network. Nanoparticles have also been used as agents of change in various phenomena. Poly (amidoamine) dendrimer nanoparticles have been employed extensively in biomedical applications such as gene and drug delivery systems. They disrupt cell membranes and allow the transportation of agent materials into cells. The results of a three dimensional phase field model, including elastic energy, demonstrate that an amine-terminated G7 dendrimer, which has positive charges on the surface, causes a hole in the membrane. The molecules removed from the membrane encircle the

dendrimer and form a dendrimer-filled membrane vesicle. This behavior is significantly reduced for a smaller dendrimer. An acetamide-terminated dendrimer, which has a different surface end-group with a neutral charge, does not induce a hole effectively. These results agree with the experimental observations. Relatively larger particles, such as liquid droplets, also have diverse applications such as ‘lab-on-a-chip’ systems for biomedical diagnostics. Practical application of those devices requires complex surfaces and morphologies of the droplet and electrodes. The dynamic aspect of the phenomenon is also an important factor for designing devices. Computational works may provide a useful tool for the design and extend the window of observation. A phase field model, combining the thermodynamics and hydrodynamics, predict the evolution of morphology of the droplet with or without an electric field. Furthermore, it predicts the instability occurrence at above-critical external field strength, which is observed from experiments. A parametric study, combined with a stability analysis, shows a tendency of the instability to depend on the surface energy and the strength of the applied field.

CHAPTER 1

INTRODUCTION

This research has its origin in the significant and growing interest in nanoscale science, engineering and technology. Fundamentally, nanotechnology is the science and technology of precisely constructing structures of matter at the nanoscale level and controlling the morphology of them, which brings inherent advantages, such as faster response time, lower power consumption, and greater density. That is why nanotechnology is widely viewed as the most significant technological frontier currently being explored. Nanostructures usually refer to those structures with a physical dimension smaller than 100 nanometers, ranging from clusters of atoms to dimensional

layers. Nanostructures exhibit unique properties, such as the quantum supercurrent transistor [1], single-electron tunneling [2], and charge transport/electron-hole recombination phenomena [3], which have generated great interest in nanostructures for potential application in electronics, optics, and biomedical sciences. Generally, there are two approaches available for producing nanostructures. The first way is to start with a bulk material and then modify it into smaller pieces using mechanical, chemical or other forms of energy, which is referred to as the 'top-down' approach. Because the conventional optical or ultraviolet photolithography has difficulties shrinking the feature size of structures, other forms of lithography technologies such as UV, X-ray, ion beams, and electron beams continue to grow. An opposite approach is to synthesize the material from atomic/molecular species via chemical or physical reactions, allowing for the precursor particles to arrange themselves into a structure which induce a specific functionality into that material. This 'bottom-up' approach is motivated by self-assembly.

Some recent progresses have demonstrated the potential of self-assembly technology by various periodic patterns on the nanoscale level. Li *et al*. [4] grew ferromagnetic iron films on the oxygen-striped copper substrate and Parker *et al*. [5] used the self-assembled pattern to form metallic nanowires. Furthermore, Bacteria [6], macromolecules [7], diblock copolymers [8], and nanoparticles [9] can also self-assemble into ordered structures with precision. Self-assembly of nanoparticles is regarded as one of the most promising approaches for generating nanostructures because the current synthetic technologies develop a wide variety of shapes and morphologies of nanoscale particles. In addition to rods, wires, and core-shell particles, the latest synthetic techniques demonstrate the possibility of making diverse shapes of nanoparticles such as

rings, cubes, triangular prisms, and many other unique shapes. Moreover, the self-assembly of nanoparticles provides advantages, compared to the top-down approach. First, the generated structures from the self-assembly may be thermodynamically stable. Second, a large number of nanoparticles can be arranged simultaneously. Here, we need to pose a question: How do we organize these nanoparticles into more complex structures? How do we control the morphology of those structures? Consequently, the present challenge of nanotechnology is to organize them in one-, two-, and three-dimensional structures and how to design them to have specific functions. In order to address this challenge, we introduce an electric field, which has recently raised great interest in controlling nanoscale features, to a number of material systems such as ellipsoidal nanoparticles which have core-shell structures and dielectric binary nanospheres.

Nanoparticles are also seen as agents of changes of various phenomena and processes. For instance, nanoparticles have a large impact on the development of diverse biomedical applications due to their ease of preparation and comparable size to the biological organs, which brings less interference with the biological units. Also, in order to reduce possible side effects, the agents should have selective interfaces coupled with the target cells, for example, a tumor. The approaches used for this purpose include nanoparticles with a functionalized surface chemistry and a coating with monolayers of molecules. Several classes of polymer nanoparticles [10, 11] are employed for this purpose and play a similar role including cell penetrating peptides. However, the details of these actions are only partially understood. In this thesis, we focus on the poly (amidoamine) dendrimer nanoparticles, which are considered to be very promising candidates for biomedical applications.

In addition, many prototype devices, such as the nanoparticle logic gate [12], are related to nanoparticles. Also, due to the wide range of the UV-visible spectrum, nanoparticles are excellent candidates for photovoltaic devices [13]. Another application is related to miniaturization of the devices. The reduced size may bring inherent advantages, such as increased reaction speed, portability, and low power consumption. One prominent example includes “lab-on-a-chip” for applications [14, 15] such as DNA analysis and biomedical diagnostics which is increasingly receiving more attention. Those applications require manipulation of small droplet volumes within the range of nanoliters or less.

This dissertation addresses the physics related to nanoparticles, focused on the self-assembly of nanoparticles and interactions with nanostructures. The topic includes an electric processing for nanoparticles, the self-assembly of nanoparticles, the interaction of a dendrimer nanoparticle with a lipid-layer, and the electrowetting phenomenon of a droplet particle.

1.1 ELECTRIC FIELD PROCESSING OF CORE-SHELL NANOPARTICLES

A suspension of nanoparticles in a dielectric fluid has great potentials for a wide spectrum of materials and device applications [16]. The functional properties of the suspension can be tuned by controlling the orientation of the particles with an applied electric field. An electric field has recently raised great interest in the application of controlling nanoscale features due to the strength and long range effect of the

electrostatic interactions. Studies showed that a particle with an anisotropic geometry can rotate preferentially with an applied electric field [17-21]. Spherical particles were shown lined up in a chain because of the attraction between induced dipole moments [22-24].

These phenomena suggest the possibility of bringing about controlled changes in the nanoparticle arrangement to achieve desirable physical properties. Particle light valves [25] or suspended-particle devices [26] are examples that use these phenomena. These devices change light transmission properties in their response to an applied external field and thus control the amount of light allowed to pass through. A smart glass, which changes from transparent to opaque, partially blocks light while maintaining a clear view of what lies behind the window.

Another application uses polymer cholesteric liquid crystal flakes [27], which exhibit selective reflection by causing light of specific wavelengthes and polarization to be reflected from the flake surface. Thus, a large visual effect is created if the flakes are viewed off-axis or if they are tipped with respect to normal direction of the incident light.

In material science applications, reorientation of inclusions in the presence of an electric field can be used for local optimization of micro/nanostructures in a polymeric composite. In the process, nanoparticles are aligned in a fluidic polymeric precursor and then cured to a solid state. This field-aided micro-tailoring approach may produce composite materials with multifunctional properties [28]. Figure 1.1 shows a micro-photograph of an epoxy-graphite composite processed in the electric field of two planar electrodes. Graphite particles arranged in chainlike structures are seen in area (1) of Figure 1.1(b).

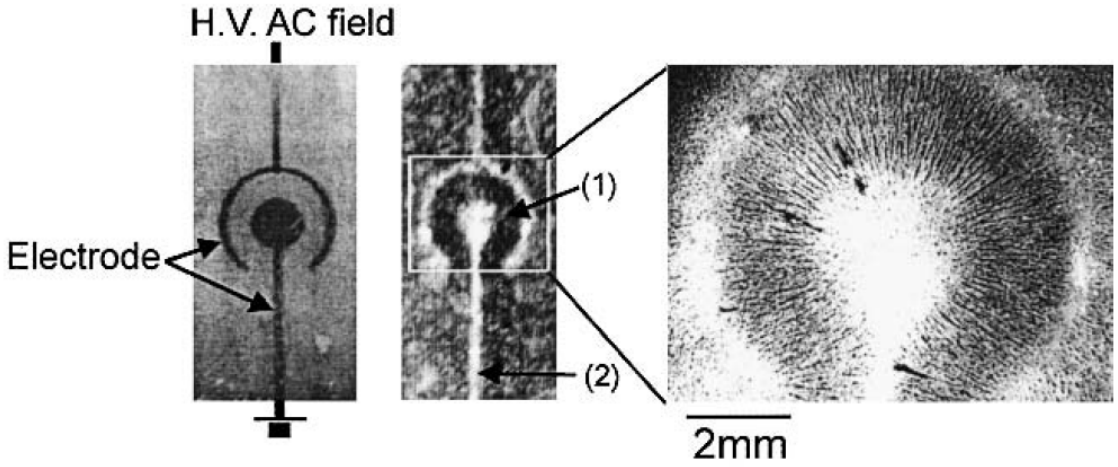

(a) (b)

Figure 1.1 (a) Graphite-epoxy composite in the field of planar electrodes (b) enlarged area has chain-like structure of the graphite [28]

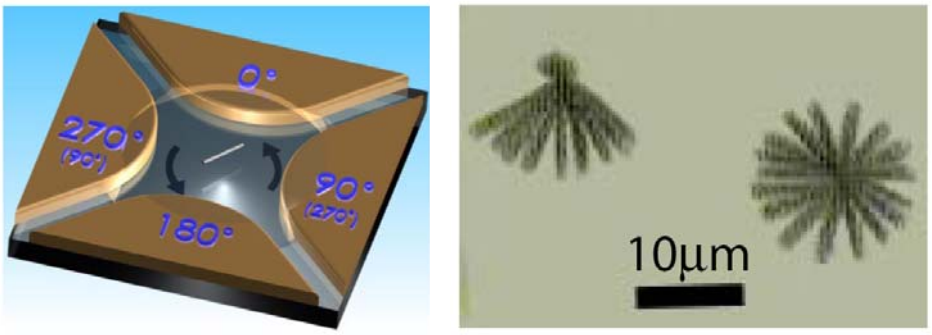

(a) (b)

Figure 1.2 (a) Schematics of a nanowire suspended in DI water set to rotation by quadruple electrodes, at which four phase-shifted ac voltages are simultaneously applied with a sequential phase shift of 90°. (b) Overlapped images at 1=30 sec interval of free (right) and one end fixed (left) rotating Au nanowires at 2.5 V, 80 kHz [29].

A nanowire rotating with a high speed is another example. Novel devices at nanoscale level need to manipulate small objects, such as those rotating with high speeds. Small entities are usually suspended in a proper liquid to avoid adhering to the surface by the van der Waal forces. However, it is challenging to control the rotation of small objects because of the viscosity and Brownian motion from the liquid. Here, an electric field provided by patterned electrodes can accommodate this challenge. Fan *et al*. [29] demonstrated that a nanowire in suspension can be rotated at a specific rotation speed. Figure 1.2 shows a schematic of the device and rotating images of the nanowire.

Despite the technical promise, colloidal nanoparticles demonstrate complicated behaviors in response to an applied field. Practical applications call for an extensive understanding of the physical mechanism and dynamic processes [30, 31]. Chapter 2 will explore the possibility of utilizing an electric field to control the rotational behavior of a core-shell nanoparticle. In this research, we developed an approach to rigorously calculate the induced torque of core-shell nanoparticles. We will also show that the Brownian motion of many nanoplates and nanofibers make it possible to investigate the rheological properties of nanoparticle dispersions.

1.2 SELF-ASSEMBLY OF NANOPARTICLES

Technology of precisely constructing and controlling structures in nanoscale may have a promising potential for generating functional materials and novel devices [32-34]. Self-assembly of nanobuilding blocks into a specific structure is generally regarded as the most effective way to design and control nanoscale structures. Among diverse driving forces for self-assembly, such as chemical bonds [35], electromagnetic fields [36], fluidic forces [37], and capillary forces [38], the electrostatic interaction has raised great interest because of the long-range effects and simplicity of control. Examples include patterning molecules [39], promoting the exfoliation of nanoplates [40], and controlling the rotating of nanoparticles [41]. Figure 1.3 shows microwire assembly by dielectrophoresis from the suspension of metallic nanoparticles [24]. The gold nanoparticles are attracted to and aggregate on the metallic part of the wire tip, thereby forming a complex structure. Another important application is an eletrorheological (ER) fluid [42], which is composed of nanoparticles dispersed in a dielectric liquid. Monodispersed spherical particles acquire electric moments, then line up into a chain which is parallel to the applied field. In this phenomenon, a pair-wise dipolar interaction between particles plays an important role.

Binary mixtures may provide a much richer class of nanocomposite materials. Solid mixtures of polymers at nanoscale can exhibit mechanical, optical, and electro-optical properties that are not attainable with a single polymer. Binary nanoparticle superlattices enhance the possibility of combining the properties of individual components with new functionalities that arise from the interactions between different

nanoparticles. Examples include an enhancement of the energy product in the nanocomposite materials by exchange coupling between nanoparticles of magnetically soft and hard materials. Figure 1.4 shows one example of nanoparticle assemblies of Fe_3O_4 (12 nm) and $Fe_{58}Pt_{42}$ (4 nm) [43]. A large difference in sizes results in clear phase segregation with particles forming their own lattice arrays.

The formation of nanostructures, through the use of electrostatically induced self-assembly of nanoparticles, are investigated in Chapter 3. Brownian dynamics will be outlined, which allows for observation of the rich patterning dynamics and a number of superlattices from core-shell columns to well-dispersed alternating structures. In addition, it also presents how parameters such as relative permittivity, volume fraction and particle size can be utilized to tune the superlattice structures.

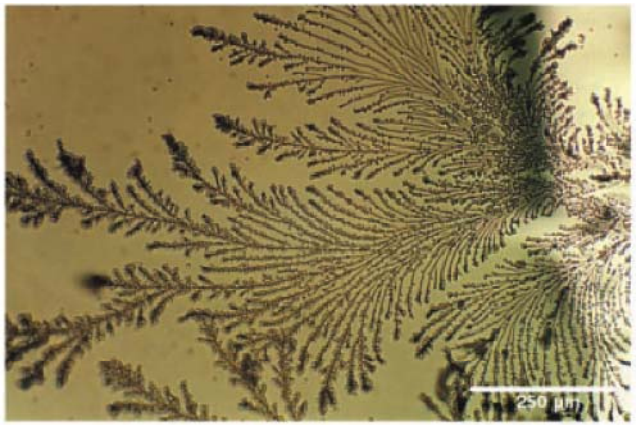

Figure 1.3 Composite wires: a thin fractal gold structure grown on the surface and surrounded by a half-shell of latex microspheres [24].

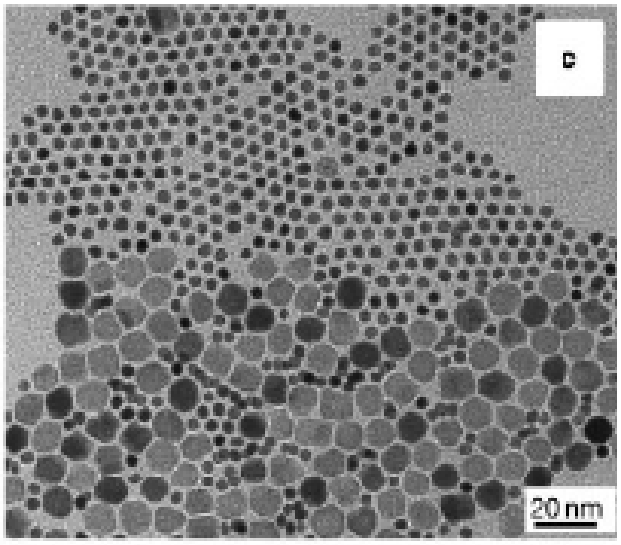

Figure 1.4 TEM images showing binary nanoparticle assemblies of Fe_3O_4 (12 nm) and $Fe_{58}Pt_{42}$ (4 nm). The assembly contained Fe_3O_4 and FePt binary nanoparticles with a mass ratio of Fe_3O_4:FePt=1/10 and was formed by solvent evaporation of the mixed nanoparticle dispersions on amorphous carbon-coated TEM grids [43].

1.3 INTERACTION OF POLY (AMIDOAMINE) DENDRIMERS WITH LIPID BILAYERS

Dendrimers are a new class of branched, synthetic macromolecules with layered architectures that show potential for diverse biomedical applications such as gene therapy and targeted drug delivery [44, 45]. Dendrimers consist of a series of chemical shells, called generations, that are built on a small core molecule. Each shell consists of two chemicals which are always in the same order. Poly(amidoamine) (PAMAM) dendrimers, in particular, have been considered to be very promising nanoparticle candidates for biomedical applications because they have excellent monodispersity, well-defined mass and size, and surfaces that are chemically functionalized [46-48]. The success of PAMAM dendrimers, however, in biomedical applications poses a question regarding how dendrimers interact with cell membranes. In some cases, nanoparticles can result in cytotoxicity, which can be beneficial [49] or harmful [50]. Previous studies [51, 52] have addressed the biocompatibility of dendrimers by investigating the interaction with lipid visicles and cultured cells. It was found that dendrimers are able to cause a disruption of membranes and that the interaction became stronger for dendrimers of higher generations carrying positive charges. Using a atomic force microscopy (AFM), enzyme assays and a fluorescence microscopy , Hong *et al.* [53, 54] observed that amine-terminated generation 7 (G7) PAMAM dendrimers caused holes to form in aqueous and supported lipid bilayers. Whereas acetylated dendrimers (G5) did not cause holes, but expanded holes at existing lipid bilayers. Those observations suggest that the surface end group plays an important role in the interactions between the dendrimers and the membranes. Mecke *et al.*[55, 56] investigated the interaction of DMPC-supported lipid bilayers by AFM. They observed

that the dendrimer size influences the interactions with lipid bilayers. As can be seen in Figure 1.5, high-generation dendrimers caused formation and growth of holes in the membranes, whereas the ability to remove lipids from bilayer was reduced for lower generation dendrimers. In addition, they also found an effect of surface chemistry on the propensity for hole formation, which is similar to the observation of Hong *et al.* [53, 54].

Despite the experimental observations, the fundamental mechanism of the interaction is still not understood well. We have proposed a three-dimensional phase field model to account this interaction between a dendrimer particle and a membrane. Attention is focused on the hole-formation process on the membrane. We seek a way to elucidate formation of a hole in a membrane due to a dendrimer particle and to provide the physical understanding for the mechanism from the fundamental of thermodynamics. The details are described in Chapter 4.

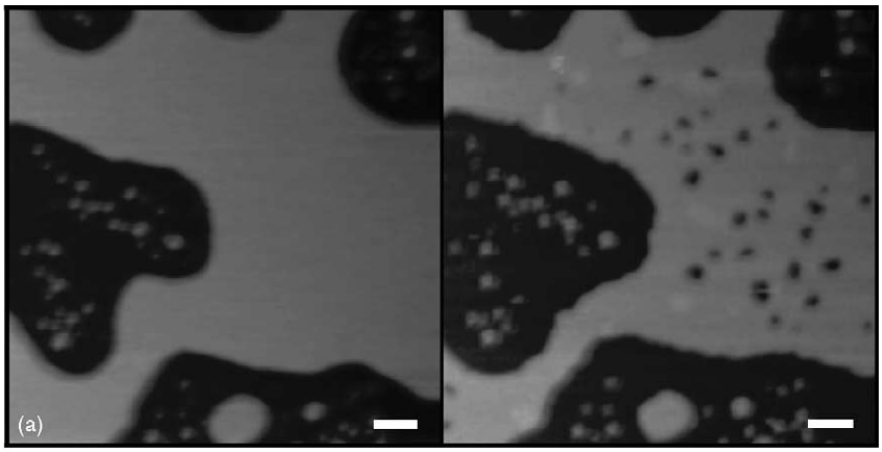

Figure 1.5 Supported DMPC bilayer imaged in water before (left images) and after (right images) adding G7 PAMAM dendrimers with amine capping group (injection method; estimated final dendrimer concentration 10–15 nM; time between the two images of each set is several minutes). Scale bars: 100 nm [55].

1.4 ELECTROWETTING OF A DROPLET PARTICLE ON A DIELECTRIC

Miniaturization has been a continuing trend in the production-technology because it may bring inherent advantages such as lower cost, higher speed, and greater density. The 'lab-on-chip' system for biomedical diagnostics [57, 58] is one example fueled by the above advantages. One significant result from the reduction in size is an increase in the surface-to-volume ratio, which makes the surface energy dominate the system. In order to experience the utmost potential, a small structure needs to control surface morphology [59] and morphological transitions [60]. Electrowetting, wherein the wettability of a droplet can be controlled by applying an electric field, has become an especially successful mechanism to control the surface morphology with controllable wettability.

Electrowetting allows one to design an optical system [61-63], such as camera lens, with variable focal length that can be achieved by electricity. Hayes *et al*. [64] introduced a potential use of electrowetting in reflective display technology. Figure 1.6 shows the principle; an oil film ruptures upon the applied voltage then contracts into one corner, as a result, the reflectivity can be increased.

A fluidic motion also can be used for assembly of nanowire by using a droplet inside microchannels. The droplet motion creates flow patterns which are responsible for the nanowire's alignment. A recent work [65] demonstrated that suspended rod-like particles in a shear flow spend most of their time aligned with the streamlines and rotate occasionally in closed orbits. Combining those results with the electrowetting effect may provide a more powerful control tool in the self-assembly of nanowires.

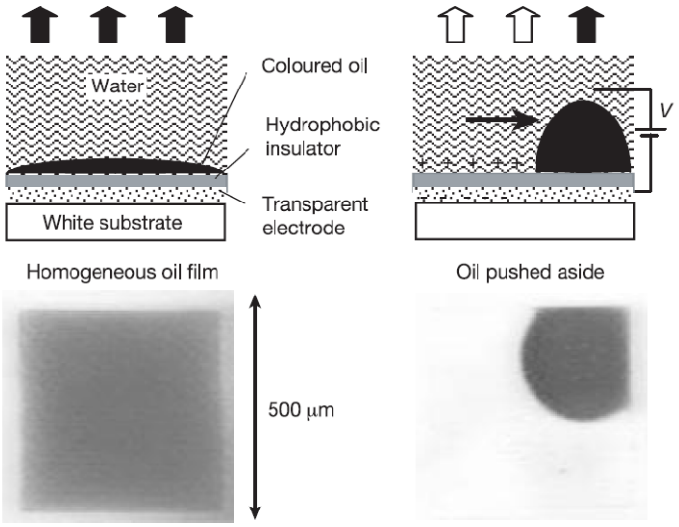

Figure 1.6 Electrowetting display principle. a) No voltage applied, therefore a coloured homogeneous oil film is present. b) d.c. voltage applied, causing the oil film to contract. Top row, diagrams; bottom row, photographs. The photographs show typical oil motion obtained with a homogeneous pixel electrode [64].

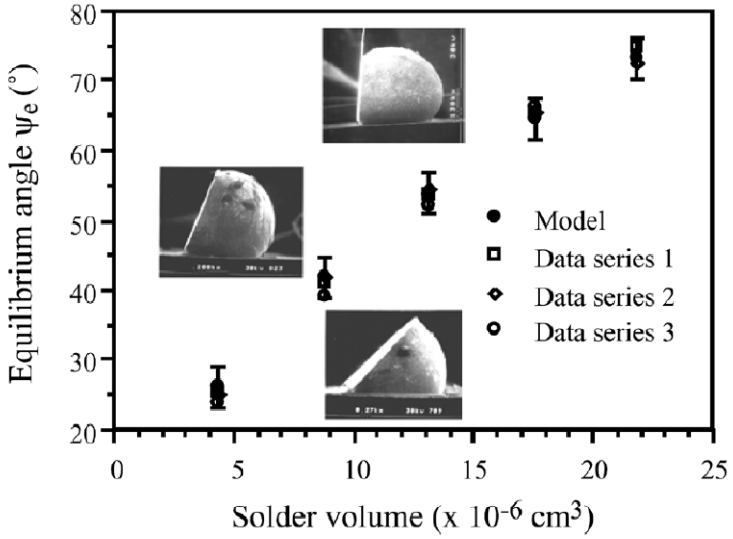

Figure 1.7 Surface tension powered self-assembly. The variation of final angle with liquid volume [66].

The surface tension is appropriate for carrying out reshaping and assembly in the microstructure size domain because of the low dimensional power of its force scaling law. Syms *et al*. [66] have devised methods for self-organization of randomly oriented parts and for their controllable attachment to the MEMS structures or circuitry. Figure 1.7 shows the contact angle variations within the liquid volume. In addition, the surface tension may provide a liquid motor which has many advantages compared to ECF or the tilting motion of microplates. They proposed a liquid motor using electrowetting actuation. By electro-wetting, the liquid is deformed and the floating plate is rotated at 180 rpm.

While electrowetting has become one of the most widely used tools for manipulating small amounts of liquid droplets on surfaces, there are many practical limitations to this method. Those include the saturation of the contact angle and the instability of the contact line. Specifically, the instability phenomenon is still not well understood and may be an obstacle for the practical applications. Chapter 5 will provide a physical understanding for the instability phenomenon and a useful guide for the control of that phenomenon. In addition, the dynamic responses of the droplet and the effect of patterned electrodes, which are important for designing practical devices, will be also discussed.

CHAPTER 2

ELECTRIC FIELD PROCESSING OF CORE-SHELL NANOPARTICLES

Dispersion of functionalized nanoparticles with surface coatings in a dielectric medium has a wide spectrum of applications from advanced materials to nanodevices [16]. Morphology control is key to achieving the full potential. Materials with designed distribution and orientation of nanoparticles offer superior properties, unique functionalities and maximum flexibilities that cannot be achieved by the current uniformly/randomly dispersed nanocomposites. Recent studies have shown that nanoparticles with anisotropic geometries may rotate preferentially under applied electric fields [21, 29, 67], suggesting an approach to bring about controlled particle orientations

in a matrix. The observations pose interesting scientific problems and call for a quantitative understanding of the phenomena. The rotation of a micro or larger sized particle in an electric field has been investigated by many researchers. Several theories and experiments have been reported on micro or larger sized particles [21, 68-70]. Stratton calculated the potential energy of a lossless dielectric placed in an electric field and derived the torque from it [71]. Due to the anisotropic geometry of the particle, the potential energy of the system depends on the orientation with respect to the applied field. The direction corresponding to the minimum potential energy determines the stable orientation. It was shown that the magnitude of the torque depends on the permittivities of the particle and its medium. A particle will orient its longest axis parallel to the applied field. The behavior of a lossy dielectric particle in an alternating field is more complicated since it depends on both material properties and field frequency. Teixeira-Pinto *et al*. observed the frequency-dependent orientation of conductive ellipsoids [72]. Schwarz *et al.* [73] and Saito *et al.* [74] relied on the calculation of the potential energy of a lossy dielectric particle to find the stable orientation, which corresponds to the lowest potential state of the system. However, some researchers pointed out that the energy method is invalid in dissipative media [75, 76]. Gruzdev suggested that when the applied field is quite uniform (the wavelength of the spatial variation of the field is much larger than the particle size), a particle can be treated as an effective dipole to calculate the interaction [77]. Maxwell stress tensor method can be used to rigorously calculate the torque on a particle in arbitrary situations [78]. However, the approach requires the computation of surface integrals, which can be cumbersome for general geometric shapes.

Thus the effective dipole method has been frequently employed for the calculation of the torque of single micro-meter or larger sized particles.

Nanoparticles possess several unique aspects that distinguish their behaviors from microscale counterparts. First, nanoparticles are often coated. This process is often necessary to prevent agglomeration. In addition, studies show that coating can increase the lifetime of a fiber under static fatigue, greatly delay the onset of the fatigue knee, and reduce the strength degradation due to zero stress aging [79]. Coated nanoparticles form a core-shell structure, which makes their rotational behaviors complicated. Secondly, the effect of Brownian motion and rotation becomes important due to the small particle size [80]. Thus simulations taking into account the thermal motion of the particles play an important role in investigating the stability, internal structure, and rheological properties of nanoparticle dispersions.

In this chapter, we develop an approach to rigorously calculate the induced torque of core-shell nanoparticles with anisotropic geometries subjected to an applied electric field. The study shows that the shell of a nanoparticle has an important effect on the rotational behavior, even when the shell is thin and takes only a small portion of the total volume. For lossy dielectrics, we show that the permittivities and conductivities of both the shell and core of a particle determine the magnitude and direction of the induced torque. The core-shell structure is found to lead to frequency dependent behavior that is quite different from that of bare nanoparticles. The study also investigates the competition between the rotational alignment due to electric field and randomization due to Brownian rotation, which revealed the evolution of the orientation distribution function of many Brownian core-shell nanoparticles suspended in a fluid.

2.1 TORQUE ON A CORE-SHELL NANOPARTICLE

The fundamental mechanism of nanoparticle rotation can be understood in the following. Imagine a dielectric nanoparticle in vacuum. An applied electric field will induce electric moments inside the particle. Generally speaking, when the particle has an anisotropic geometry, the direction of the total induced moments does not coincide with that of the applied field. Thus the moments interact with the field and cause the particle to rotate. The torque on the particle, $\mathbf{T}$, can be obtained by considering the virtual rotation and the associated free energy change. The expression takes the form of $\mathbf{T} = \int \mathbf{P} \times \mathbf{E}_0 dV + \int \mathbf{r} \times (\mathbf{P} \cdot \nabla)\mathbf{E}_0 dV$ [75]. Here, $\mathbf{P}$ is dielectric polarization, $\mathbf{E}_0$ is the applied external field, and $\mathbf{r}$ is a position vector. The integration extends over the volume of the particle. In an almost uniform applied field, which may be regarded as constant over the dimensions of the particle, the second term can be neglected. When a particle is inside a dielectric medium, an applied electric field can induce polarization in both the particle and the medium. The polarizations interact with each other and change the field distribution. An effective dipole method has been developed for a lossless particle under a uniform external field [68], which is consistent to the result from the energy variational approach [71]. However, the effective dipole method does not apply to the situation where two dielectric bodies are very close, which requires the consideration of multi-poles. To rigorously calculate the torque on a core-shell nanoparticle, we apply the Maxwell stress tensor approach. The Maxwell stress tensor, $\boldsymbol{\sigma}$, is defined by $\boldsymbol{\sigma} = \varepsilon_m \left(\mathbf{EE} - 0.5 \left| \mathbf{E} \right|^2 \mathbf{I} \right)$, where $\mathbf{E}$ is the electric field, ε_m is the permittivity of the

medium, and **I** is the identity tensor. The torque is obtained by an area integration over a closed surface which surrounds the particle, namely [78],

$$\mathbf{T}=\int_A \mathbf{r}\times(\boldsymbol{\sigma}\cdot\mathbf{n})dA \tag{2.1}$$

where $\mathbf{r}$ is a position vector and $\mathbf{n}$ the unit normal vector of the closed surface.

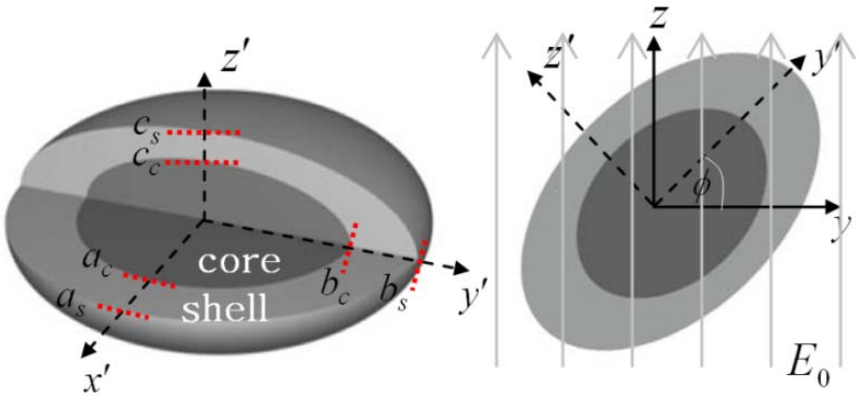

(a) (b)

Figure 2.1 (a) A confocal core-shell ellipsoid (b) the rotation of a nanoparticle around its local *x* axis.

Consider a confocal core-shell ellipsoid shown in Figure 2.1(a), which can represent a wide range of particle shapes from disks to rods. The principal semi-axes are a_c, b_c, c_c for the core surface and a_s, b_s, c_s for the outer shell surface. Any confocal ellipsoidal surface can be expressed by $x^2/(a_s^2+u)+y^2/(b_s^2+u)+z^2/(c_s^2+u)=1$ ($a_s>b_s>c_s$). This equation, a cubic in *u*, has three real roots ξ, η, and ζ that define the ellipsoidal coordinates. The coordinate ξ is normal to the surface, i.e. each ellipsoidal surface is defined by a constant ξ. Define $\xi_c \equiv a_s^2-a_c^2=b_s^2-b_c^2=c_s^2-c_c^2$. Note that $\xi=0$

on the outer shell surface. Thus the shell occupies the space of $-\xi_c \le \xi \le 0$. The electric field can be solved analytically using Laplace's equation and ellipsoidal coordinates. Consider a uniform applied field E_0 along the *x* direction. Theoretical analysis shows that the potentials ϕ_c in the core, ϕ_s in the shell, and ϕ_m in the medium can be expressed by

$$\phi_c = C_{cx} x\,,\ \ \phi_s = C_{sx} x + D_{sx} x \int_{\xi}^{\infty} \frac{dt}{R_t (a_s^2 + t)}\,,\ \phi_m = C_{mx} x + D_{mx} x \int_{\xi}^{\infty} \frac{dt}{R_t (a_s^2 + t)} \qquad (2.2)$$

The subscripts *c*, *s*, and *m* denote physical quantities in the three regions of the core, of the shell, and of the medium, respectively. Here $R_t = \sqrt{(a_s^2 + t)(b_s^2 + t)(c_s^2 + t)}$ and the constants C_{cx}, C_{sx}, D_{sx}, C_{mx}, D_{mx} are determined by the continuity and boundary conditions, i.e. the electric potentials and normal components of the electric displacements are continuous at the core-shell interface and shell-medium interface; the potential gradient at infinity must be equal to the applied electric field. The continuality of the tangential electric field at the interfaces is satisfied automatically due to the form of Eq. (2.2). Similarly, we can solve the potential field when the applied field is in the *y* or *z* direction, and denote the constants with corresponding subscripts. Thus an applied field in an arbitrary direction relative to the particle axis can be treated by superposition. For an applied uniform field $\mathbf{E}_0$, the electric field on the particle surface (i.e. $\xi = 0$) is given by

$$\mathbf{E} = \mathbf{E}_0 - \mathbf{A}\mathbf{D}_m + \frac{8\pi}{3V}\mathbf{n}(\mathbf{n} \cdot \mathbf{D}_m) \qquad (2.3)$$

Here, V is the particle volume (core plus shell), **A** is a diagonal matrix in which the elements are $A_1 = \int_0^\infty dt/R_t\sqrt{a_s^2+t}$, $A_2 = \int_0^\infty dt/R_t\sqrt{b_s^2+t}$, and $A_3 = \int_0^\infty dt/R_t\sqrt{c_s^2+t}$, and $\mathbf{D_m} = [D_{mx}, D_{my}, D_{mz}]^{\mathbf{T}}$. Note that the electric field inside the core is uniform. A disk or a fiber involves a degenerated coordinate system [75]. If $a_s = b_s > c_s$ (disk), the ellipsoidal cubic equation becomes quadratic, $\rho^2/(a_s^2+u) + z^2/(c_s^2+u) = 1$, where $\rho^2 = x^2 + y^2$. This equation has two real roots ξ and η that define the degenerated ellipsoidal coordinates, which lie in the ranges of $\xi \geq -c_s^2$ and $-c_s^2 \geq \eta \geq -a_s^2$. The coordinate ξ is normal to the surface and has $\xi = 0$ on the outer shell surface. The relation between ρ, z and ξ, η is given by $z = \pm\sqrt{(\xi+c_s^2)(\eta+c_s^2)/(c_s^2-a_s^2)}$,

$\rho = \sqrt{(\xi+a_s^2)(\eta+a_s^2)/(a_s^2-c_s^2)}$. To calculate the surface integration in Eq. (2.1), we need to know the normal vector **n** and area dA. Define $x = \rho\cos\phi$ and $y = \rho\sin\phi$, where ϕ is an angle in $x-y$ plane. By coordinate transformation we obtain the following results,

$$\mathbf{n} = \frac{1}{\sqrt{-\eta}}\left\{c_s\sqrt{\frac{\eta+a_s^2}{a_s^2-c_s^2}}\cos\phi, c_s\sqrt{\frac{\eta+a_s^2}{a_s^2-c_s^2}}\sin\phi, a_s\sqrt{\frac{\eta+c_s^2}{c_s^2-a_s^2}}\right\}^{\mathbf{T}} \tag{2.4}$$

$$dA = \frac{1}{2}\sqrt{\frac{a_s^2\eta}{\left(a_s^2-c_s^2\right)\left(\eta+c_s^2\right)}}d\phi d\eta \tag{2.5}$$

In the case of a fiber, $a_s > b_s = c_s$, the ellipsoidal cubic equation becomes $x^2/(a_s^2+u) + \rho^2/(b_s^2+u) = 1$, $\rho^2 = y^2 + z^2$. This equation has two real roots ξ and ζ that define the degenerated ellipsoidal coordinates, which lie in the ranges of $\xi \geq -b_s^2$ and

$-b_s^2 \geq \zeta \geq -a_s^2$. The relation between ρ , z and ξ , ζ is given by $x = \pm\sqrt{(\xi + a_s^2)(\zeta + a_s^2)/(a_s^2 - b_s^2)}$, $\rho = \sqrt{(\xi + b_s^2)(\zeta + b_s^2)/(b_s^2 - a_s^2)}$. Define $y = \rho\cos\varphi$, $z = \rho\sin\varphi$, where φ is an angle. The normal vector $\mathbf{n}$ and dA are given by

$$\mathbf{n} = \frac{1}{\sqrt{-\zeta}}\left\{b_s\sqrt{\frac{\zeta + a_s^2}{a_s^2 - b_s^2}}, a_s\sqrt{\frac{\zeta + b_s^2}{b_s^2 - a_s^2}}\cos\varphi, a_s\sqrt{\frac{\zeta + b_s^2}{b_s^2 - a_s^2}}\sin\varphi\right\}^{\mathrm{T}} \tag{2.6}$$

$$dA = \frac{1}{2}\sqrt{\frac{b_s^2\zeta}{\left(b_s^2 - a_s^2\right)\left(\zeta + a_s^2\right)}}d\varphi d\zeta \tag{2.7}$$

The torque on a core-shell nanoparticle can then be calculated by Eq. (2.1) and Eq. (2.3).

2.2 NUMERICAL RESULTS

2.2.1 Torques on the lossless particles

First look at the rotation of a lossless dielectric nanoparticle about the *x*-axis when an electric field $\mathbf{E}_0$ is applied along the fixed z_0 axis, as shown in Figure 2.1(b). The torque calculated from Eq. (2.1) depends on the shape of the particle and the permittivity ratios of the core/ medium, $\beta_c = \varepsilon_c / \varepsilon_m$, and shell/medium $\beta_s = \varepsilon_s / \varepsilon_m$. Figures 2.2 and 2.3 show representative results for axially symmetric particles about the z axis (i.e. $a_c = b_c$) at $\theta = 45^\circ$. It can be observed from Eq. (2.1) that the torque is proportional to the particle volume V , the square of the applied electric field E_0^2, and the permittivity of the

medium. Superposition of $\mathbf{E}_0$ along the local y and z directions shows that the torque takes the form of $T = (V\varepsilon_m E_0^2)H \sin\theta\cos\theta$, where H is a shape function. Thus the normalized torque $T/(\varepsilon_m E_0^2 V)$ at $\theta = 45^\circ$ is essentially half of H. The thin shell is given by $\xi_c / a_c^2 = 0.001$, or $a_s / a_c = 1.0005$. In the case of $\beta_c = \beta_s$, i.e. the shell and core have the same dielectric property, the particle is essentially a bare particle.

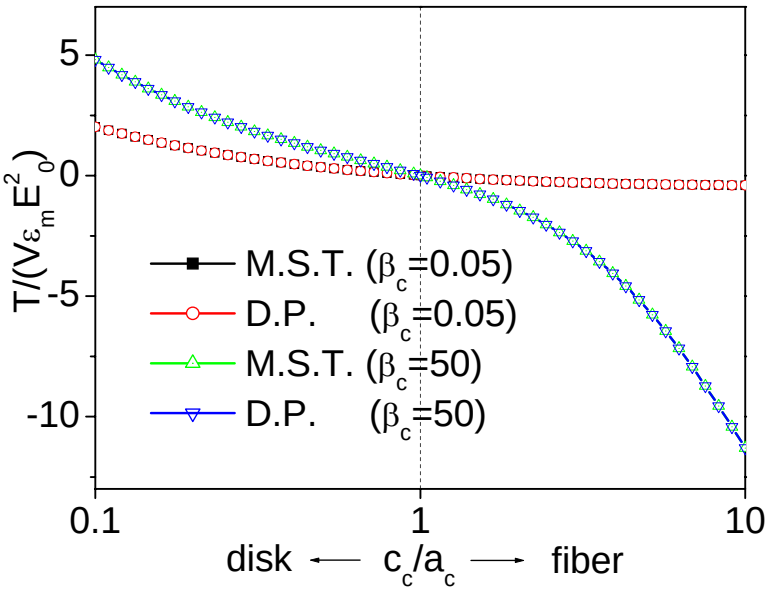

Figure 2.2 For a bare particle in a uniform external field, the effective dipole method and the Maxwell stress method give the same results.

We have used both the Maxwell stress tensor method and the effective dipole method to calculate the torque in such situations. Figure 2.2 shows that the two methods give exactly the same results for bare particles. The comparison also serves as verification of our algorithm.

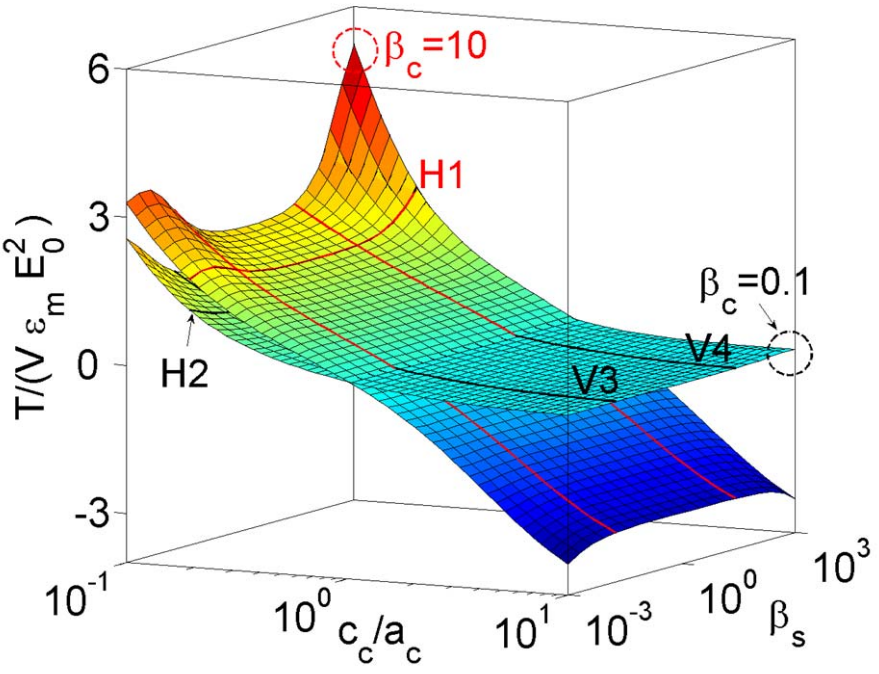
β_c=10
H1
β_c=0.1
V4
H2
V3
6
3
0
-3
T/(V ε_m E_0^2)
10^-1
10^0
c_c/a_c
10^1
10^-3
10^0
β_s
10^3

(a)

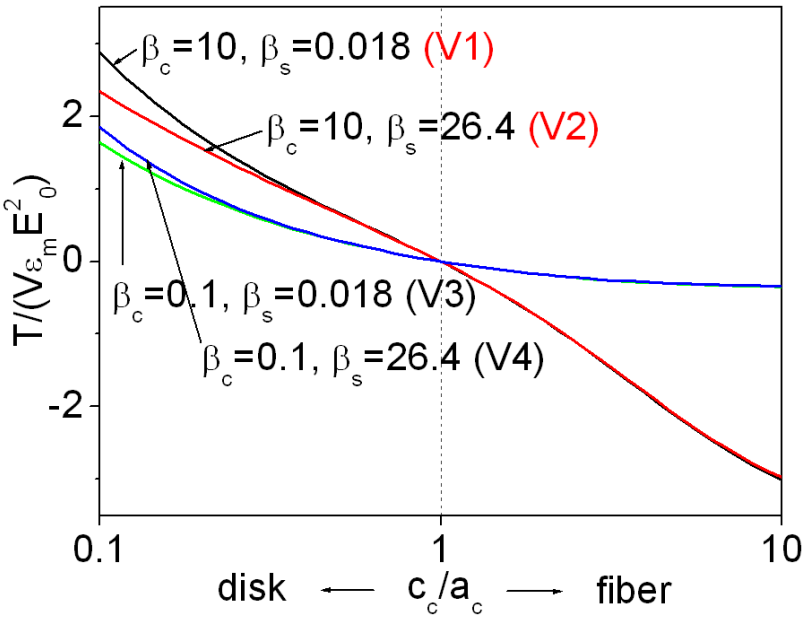
β_c=10, β_s=0.018 (V1)
β_c=10, β_s=26.4 (V2)
β_c=0.1, β_s=0.018 (V3)
β_c=0.1, β_s=26.4 (V4)
2
0
-2
T/(Vε_m E_0^2)
0.1
1
10
disk
c_c/a_c
fiber

(b)

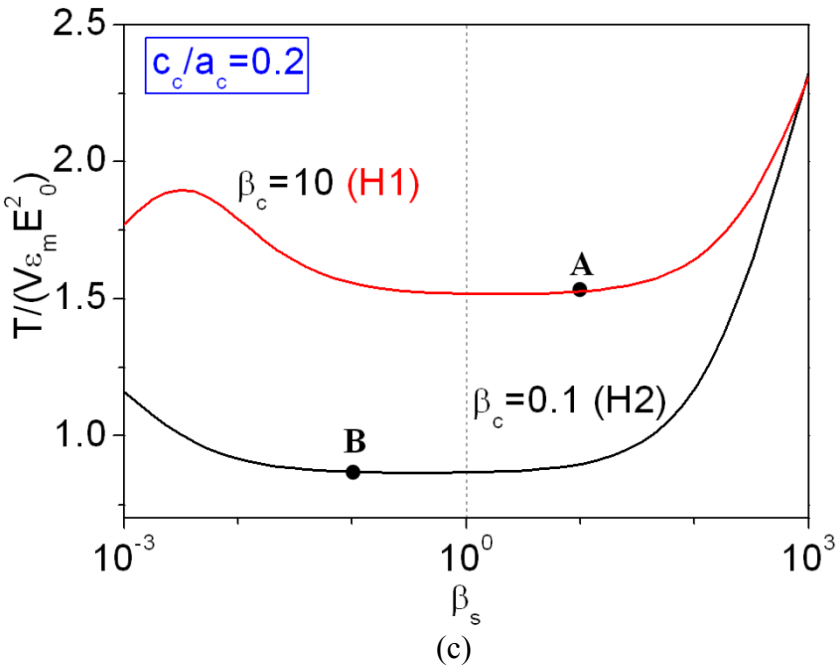

(c)

Figure 2.3 (a) Normalized torque as a function of the aspect ratio c_c/a_c and β_s for the situations of $\beta_c = 10$ and $\beta_c = 0.1$. The thin shell is given by $\xi_c/a_c^2 = 0.001$, i.e. $a_s/a_c = 1.0005$. (b) Dependence of torque on the aspect ratio for selected core and shell properties. (c) Dependence of torque on shell property β_s for a particle with aspect ratio of $c_c/a_c = 0.2$ at selected core property β_c.

Figure 2.3 reveals the effect of shell on induced torques. Figure 2.3(a) shows the normalized torque as a function of the aspect ratio c_c/a_c and β_s for the situations of $\beta_c = 10$ (the surface extends from upper left to lower right) and $\beta_c = 0.1$ (the surface extends from lower left to upper right). The $T \sim c_c/a_c$ curves at selected β_s (V1, V2, V3, V4) and $T \sim \beta_s$ curves at selected c_c/a_c (H1, H2) are shown in Figure 2.3(b) and (c). Figure 2.3(a) shows that in all situations the torque is positive for a disk ($c_c/a_c < 1$) and negative for a fiber ($c_c/a_c > 1$). This feature is consistent with that of a bare particle, which suggests that a particle tends to align its longest axis to the direction of the applied

field. As observed in Figure 2.3(a) and (b), the magnitude of the torque decreases (for disk) or increases (for fiber) with the aspect ratio. This feature is also consistent with that of a bare particle. However, the effect of shell on the magnitude of the torque demonstrates interesting behavior and strong dependence on the material properties. Our computations suggest that when both the permittivities of the core and shell are larger than that of the medium ($\beta_c > 1$ and $\beta_s > 1$) , a larger shell permittivity helps to increase the torque. In contrast, when both permittivities are smaller than that of the medium ($\beta_c < 1$ and $\beta_s < 1$), a smaller shell permittivity helps to increase the torque. The curves of $\beta_c = 10$ (right half, $\beta_s > 1$) and $\beta_c = 0.1$ (left half, $\beta_s < 1$) in Figure 2.3(c) clearly demonstrate the trend. If the core has larger and the shell has smaller permittivity than that of the medium ($\beta_c > 1$, $\beta_s < 1$), or vice versa ($\beta_c < 1$, $\beta_s > 1$), the trend will depend on particle geometry. This behavior can be seen in Figure 2.3(a) by comparing the torques of disk ($c_c / a_c < 1$) and fiber ($c_c / a_c > 1$). Figure 2.3(c) shows an example for a disk. The curve of $\beta_c = 10$ reaches maximum at a certain β_s when $\beta_s < 1$, suggesting a competition of the core and shell contribution to the torque. Note that point A ($\beta_c = 10$, $\beta_s = 10$) and point B ($\beta_c = 0.1$, $\beta_s = 0.1$) correspond to bare particles. Take point A and the $\beta_c = 10$ curve as an example. When the shell permittivity is a little less than that of the core, i.e. a point to the left of A, the torque reduces. However, the torque eventually increases when the shell permittivity is much smaller, even less than of the medium. Analogical behavior exists for point B and the $\beta_c = 0.1$ curve. Both curves suggest that the shell dominates the torque when its permittivity is much different from that of the medium.

2.2.2 Torques on the lossy particles

In general, nanoparticles and the surrounding medium are not ideal dielectrics. In this case we must take into account the effect of electric conductivity. The response of a lossy dielectric to an external field depends on the field frequency. This frequency dependence reflects the fact that a material's polarization does not respond instantaneously to the applied field. For this reason, the permittivity is often treated as a complex function of the frequency. Define complex dielectric properties $\varepsilon_m^*(\omega) = \varepsilon_m - i\sigma_m/\omega$, $\varepsilon_s^*(\omega) = \varepsilon_s - i\sigma_s/\omega$ and $\varepsilon_c^*(\omega) = \varepsilon_c - i\sigma_c/\omega$, where ω is the frequency of the applied electric field, σ_m, σ_s, and σ_c are the electric conductivities of the medium, shell, and core, respectively. The time-averaged Maxell stress tensor is given by $\boldsymbol{\sigma} = 0.25\,\mathrm{Re}\{\varepsilon_m\}(\mathbf{E}\mathbf{E}^* + \mathbf{E}^*\mathbf{E} - |\mathbf{E}|^2\,\mathbf{I})$ [78]. While the torque is still calculated by Eq. (2.1), the results are more complicated; the frequency-dependent torque now combines the relaxation phenomena of the core and shell.

Normalize the permittivity and conductivity of the core and shell by those of the medium. Define $\beta_{\varepsilon c} = \varepsilon_c/\varepsilon_m$, $\beta_{\sigma c} = \sigma_c/\sigma_m$ for the core and $\beta_{\varepsilon s} = \varepsilon_s/\varepsilon_m$, $\beta_{\sigma s} = \sigma_s/\sigma_m$ for the shell. Equations (2.1) and (2.2) show that the torque becomes frequency-independent in the special case of $\beta_{\varepsilon c} = \beta_{\sigma c}$ and $\beta_{\varepsilon s} = \beta_{\sigma s}$. To demonstrate the frequency effect, Figure 2.4 shows an example of a core-shell disk with $c_c/a_c = 0.1$. The thin shell is given by $\xi_c = 0.001a_c^2$. In Figure 2.4(a) the material parameters are $\beta_{\varepsilon c} = 1.5$, $\beta_{\sigma c} = 0.8$, $\beta_{\varepsilon s} = 0.5$. The frequency is normalized by $\omega_m = \sigma_m/\varepsilon_m$. Note that at high frequencies the complex permittivity converges to real permittivity. Thus a particle

behaves more dielectric at high frequencies. In contrast, conductivity dominates the behavior at low frequencies. Figure 2.4(a) clearly demonstrates the trend. The surface is almost flat at high frequency, where the shell conductivity has little effect on the torque. At high frequency the shell conductivity can significantly affect the torque, even though the shell only takes a very small percentage of the total particle volume. Figure 2.4(b) shows the results of gold-coated SiO_2 and TiO_2 nanoparticles suspended in water. In the simulation, we took $\varepsilon_m = 80\varepsilon_0$ and $\sigma_m = 0.05$ S/m for water, $\varepsilon_c = 3.8\varepsilon_0$ and $\sigma_c = 10^{-18}$ S/m for SiO_2, and $\varepsilon_s = 6.9\varepsilon_0$, $\sigma_s = 4.3\times10^7$ S/m for the gold coating. Here, $\varepsilon_0 = 8.85\times10^{-12}$ F/m is the permittivity in vacuum. We took $\varepsilon_c = 90\varepsilon_0$ and $\sigma_c = 300$ S/m for TiO_2. The particles represent two situations where the permittivity and conductivity of the core is larger or smaller than that of the medium. Bare particles are considered by assigning the core permittivity and conductivity to the shell. In this way the bare particles and coated particles have exactly the same volume.

The torque on a bare SiO_2 particle demonstrates frequency dependence. However, after the highly insulating SiO_2 particle is coated with highly conductive gold, the torque becomes almost frequency independent in the shown frequency range. The magnitude of the torque is also much larger. The torque is essentially dominated by the shell due to its high conductivity. This behavior is reflected even at relative high frequencies. Similar effect can also be observed in the case of coated TiO_2 particle.

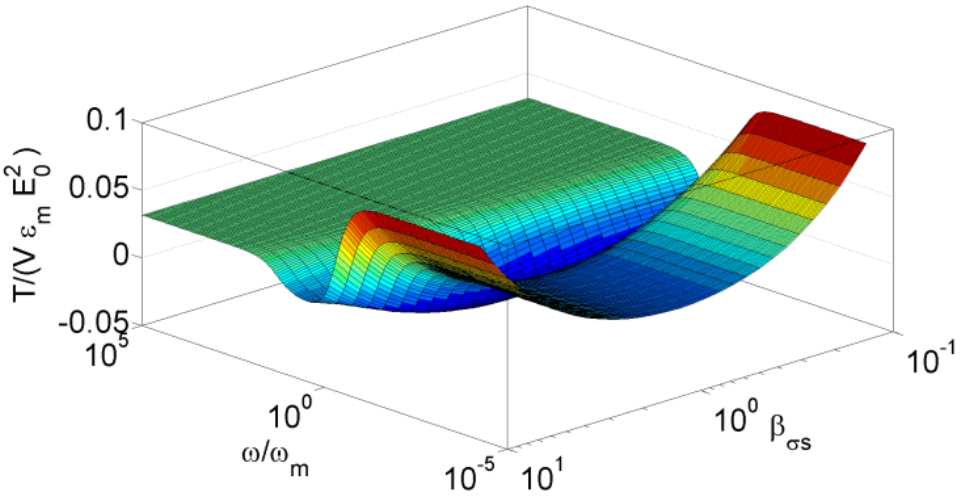

(a)

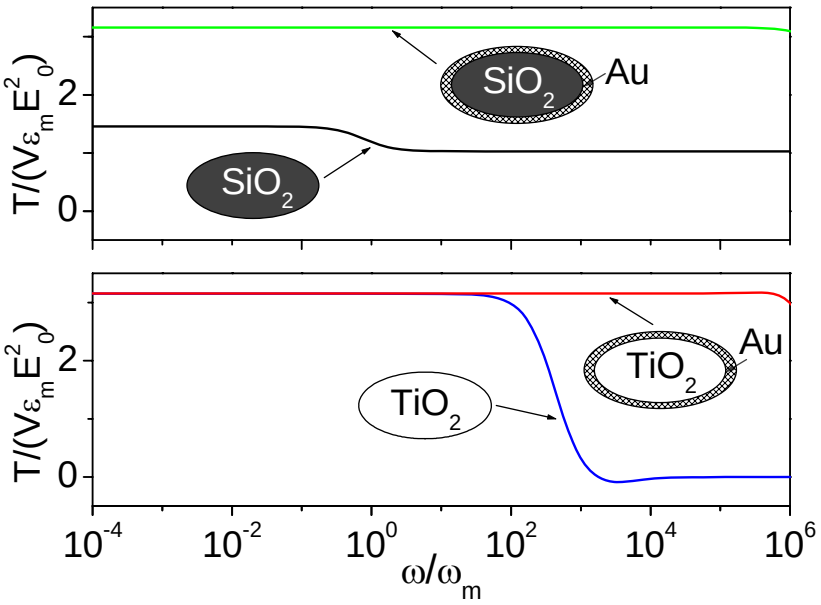

(b)

Figure 2.4 (a) Normalized torque on a lossy dielectric core-shell disk-like ($c_c/a_c = 0.1$) particle as a function of the electric field frequency and shell conductivity. $\beta_{\varepsilon c} = 1.5$, $\beta_{\sigma c} = 0.8$, $\beta_{\varepsilon s} = 0.5$. The thin shell is given by $\xi_c = 0.001 a_c^2$. (b) Torques on gold-coated SiO_2 and TiO_2 nanoparticles suspended in water. In the simulation we took $\varepsilon_m = 80\varepsilon_0$ and $\sigma_m = 0.05$ S/m for water, $\varepsilon_c = 3.8\varepsilon_0$ and $\sigma_c = 10^{-18}$ S/m for SiO_2, and $\varepsilon_s = 6.9\varepsilon_0$, $\sigma_s = 4.3\times10^7$ S/m for the gold coating. Here $\varepsilon_0 = 8.85\times10^{-12}$ F/m is the permittivity in vacuum. We took $\varepsilon_c = 90\varepsilon_0$ and $\sigma_c = 300$ S/m for TiO_2.

Note that the bare TiO_2 particle demonstrates a frequency window, where the torque becomes negative. In this case the particle will rotate so that its longest axis is orthogonal to the applied field direction. At certain frequency the torque becomes zero so that a particle will stay at the current orientation. This phenomenon suggests the possibility to combine material properties and field frequency to control the torque and the rotation of a particle. Similar phenomenon also occurs in a core-shell particle, as shown in Figure 2.4(a). In fact, choosing appropriate coating property offers more flexibility to tune the frequency window.

2.3 ROTATIONAL BEHAVIOR OF BROWNIAN NANOPARTICLES

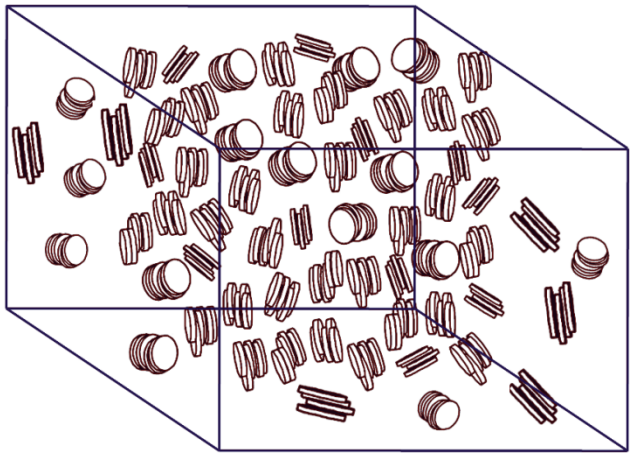

Figure 2.5 A schematic diagram for many nanoplates dispersed in a fluid. The particles are subjected to a uniform electric field

Consider lossless disk or fiber like nanoparticles dispersed in a dielectric fluid, shown in Figure 2.5, and subjected to a uniform electric field. The induced torque will drive them to rotate. Their rotation will be resisted by the viscosity of the fluid. In addition, they undergo incessant collisions with liquid molecules. These collisions cause a random torque. Consequently, the total torque acting on a nanoparticle consists of three major contributions: $\mathbf{T}_E$ due to the electric field, $\mathbf{T}_V$ due to the viscosity of the medium, and $\mathbf{T}_B$ due to the rotational Brownian motion. The torque $\mathbf{T}_E$ is given by Eq. (2.1). Superposition of $\mathbf{E}_0$ along the local y and z directions show that the torque takes the form of

$$\mathbf{T}_E = (V\varepsilon_m E_0^2) H_E(\beta_s, \beta_c) \sin\theta\cos\theta \mathbf{e}_x \tag{2.8}$$

where $H_E(\beta_s, \beta_c)$ is a shape function and $\mathbf{e}_x$ is a unit vector along the local x axis (Figure 2.1). The torque due to viscous resistance, $\mathbf{T}_V$ can be expressed by [81],

$$\mathbf{T}_V = -V\eta H_V \Omega \mathbf{e}_x \tag{2.9}$$

Here $H_V = -2\left(b_s^2 + c_s^2\right)/\left(b_s^2 A_2 + c_s^2 A_3\right)$ is another shape function relevant to viscous resistance, η the viscosity of the fluid, Ω the angular velocity, $A_2 = \frac{a_s b_s c_s}{2}\int_0^\infty \frac{dt}{(t+b_s^2)R_t}$, and $A_3 = \frac{a_s b_s c_s}{2}\int_0^\infty \frac{dt}{(t+c_s^2)R_t}$. The time scale of Brownian motion is much shorter comparing to the time characterizing the motion of nanoparticles driven by external fields. Thus we can analyze the motion by a stochastic approach. Using an Orientation Distribution Function (ODF), Ψ, which represents the probability of the particle being

found in a specific orientation, we can express the torque due to the Brownian motion [82],

$$\mathbf{T}_B = -k_B T \mathbf{u} \times \frac{\partial(\ln \Psi)}{\partial \mathbf{u}} \tag{2.10}$$

where k_B is Boltzmann's constant, T the absolute temperature of the fluid, and $\mathbf{u}$ the unit orientational vector of the particle (a unit vector along the local z axis in Figure 2.1(b)). The moment of inertia can be negligible since the small particle size leads to small Reynolds number. The angular velocity can be obtained from the balance of moment, $\mathbf{T}_E + \mathbf{T}_V + \mathbf{T}_B = 0$, which gives

$$\mathbf{\Omega} = C \sin 2\theta \mathbf{e}_x - D\mathbf{u} \times \frac{\partial \ln(\Psi)}{\partial \mathbf{u}} \tag{2.11}$$

Here we have $C = \left(\varepsilon_m H_E E_0^2\right)/\left(2\eta H_V\right)$ and $D = \left(k_B T\right)/\left(V\eta H_V\right)$. Now consider the rotation of many particles and the corresponding evolution of ODF. The orientation distribution function has to satisfy the equation of continuity[83],

$$\frac{\partial \Psi}{\partial t} + \frac{\partial}{\partial \mathbf{u}} \cdot (\mathbf{\Omega} \times \mathbf{u}\Psi) = 0 \tag{2.12}$$

Equations (2.11) and (2.12) lead to

$$\frac{\partial \Psi}{\partial t} + C\frac{\partial}{\partial \theta}(\Psi \sin 2\theta) - D\frac{\partial^2 \Psi}{\partial \theta^2} = 0 \tag{2.13}$$

We solve Eq. (2.13) by the Fourier spectral method. Denote the Fourier transform of $\Psi(\theta,t)$ by $\hat{\Psi}(k,t)$, where k is the coordinate in reciprocal space. Taking the Fourier transform on both sides of Eq. (2.13), we obtain

$$\frac{\partial \hat{\Psi}}{\partial t} = C\frac{k}{2}\left\{\hat{\Psi}(k+2) - \hat{\Psi}(k-2)\right\} - Dk^2\hat{\Psi}(k) \tag{2.14}$$

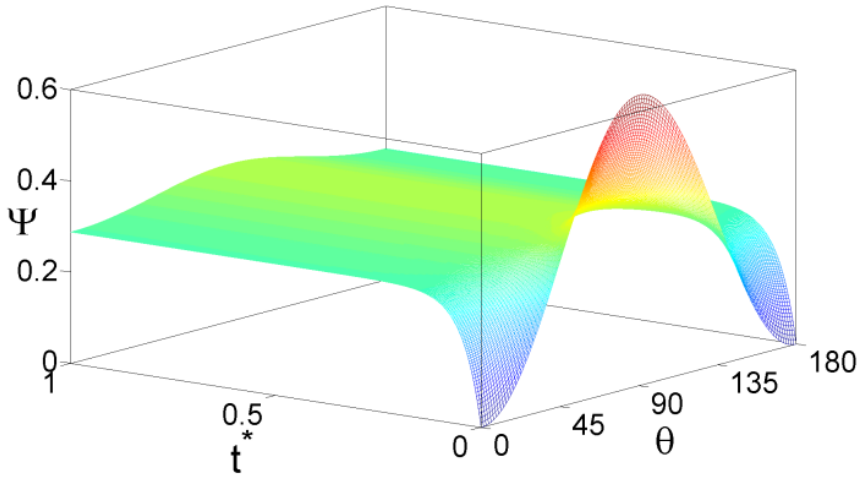

(a)

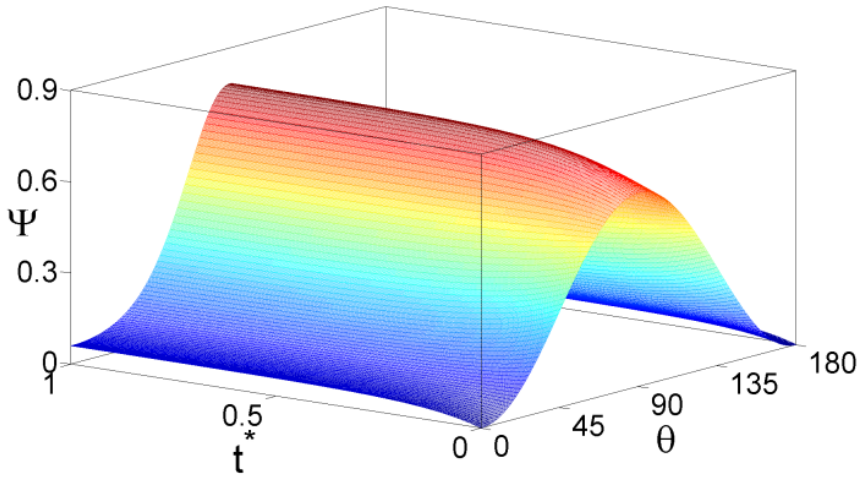

(b)

Figure 2.6 The evolution of orientation distribution function of disk-like particles (a) $D/C = 5.5$ (b) $D/C = 0.39$

Figure 2.6 shows the evolution of ODF for disks with $c_s / a_s = 0.1$. Two competing effects, the alignment due to the applied electric field and randomization due to the rotational Brownian motion, determine the time evolution of Ψ. The system eventually reaches an equilibrium Ψ distribution. Define normalized time by $t^* = t|C|$. In terms of the normalized time t^*, Equation (2.14) becomes a partial differential equation that depends on the ratio of D/C. A lager ratio means stronger diffusional effect versus alignment. Figure 2.6(a) shows the result for $D/C = 5.5$. Initially many particles are oriented close to θ=90°. Due to the relative weak electric torque, Ψ spreads and distributes more uniformly on θ over the time. In Figure 2.6(b), we increase the electric field strength so that $D/C = 0.39$. In this case the stronger electric torque drives more particles to orient close to θ=90°. Note that Ψ almost stops evolution after a certain time, which means that an equilibrium state has been reached. Rotational Brownian motion makes it impossible to align all the particles in the same direction.

Figure 2.7 shows evolution of ODF for fibers with $c_s / a_s = 10$. In this case C is negative and $D/C = -0.45$. Initially most fibers are distributed close to θ=90°. Over time more fibers orient to follow the applied field (i.e. θ=0° or θ=180°). Both Figure 2.6 and Figure 2.7 demonstrate the dynamic rotation of many particles to orient their longest axis close to the applied field direction.

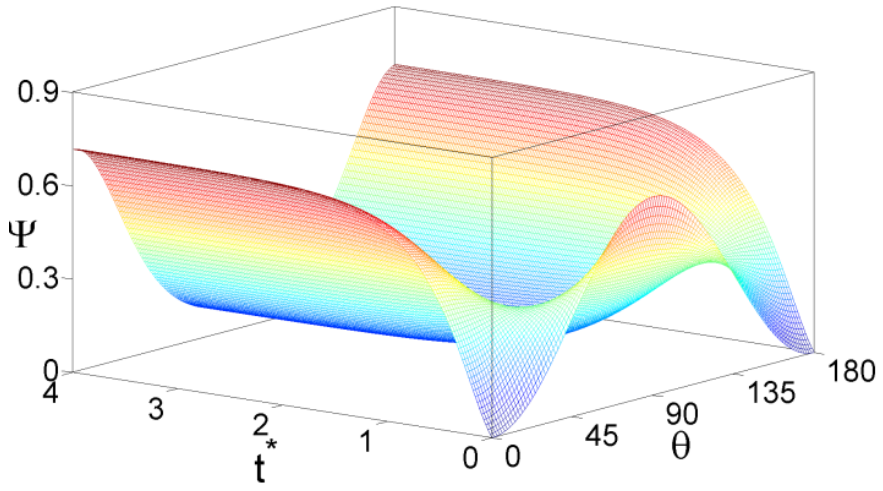

Figure 2.7 The evolution of orientation distribution function of fiber particles, $D/C = -0.45$. Here, the negative sign indicates the fiber particles.

2.3 NANOPARTICLE ROTATION CONCLUSIONS

Nanoparticles are often coated to prevent agglomeration or to achieve functional properties such as increased fatigue strength. This thesis studies the rotational behavior of core-shell nanoparticles suspended in a fluid and under an applied electric field. We calculated the electric field-induced torque rigorously by a Maxwell stress tensor method. The study showed that the shell of a nanoparticle has an important effect, even when the shell is thin and takes only a small portion of the total volume. For instance, a thin layer coating of highly conductive materials can dramatically change the induced torque on a nanoparticle. In this case the shell can shield the core and thus its property dominates the magnitude of the torque. For lossy dielectrics, the core-shell structure demonstrated

frequency dependent behavior. The preferential orientation of a particle can be changed at a frequency window. This window is important since appropriate design of frequency and material parameters may control a particle to orient in any directions.

To describe the dynamic rotation and distribution of many particles, we considered torques induced by the electric field, the viscosity of the fluid, and the rotational Brownian motion. A partial deferential equation was obtained to describe the time evolution of ODF. The equation was solved in Fourier space. The simulations suggest that two competing effects, the alignment due to the applied electric field and randomization due to the rotational Brownian motion, determine the evolution of ODF. A strong electric field leads to more preferred orientations for both disk and fiber like particles. The particle orientation distributes more randomly when the applied field is weak.

CHAPTER 3

SELF-ASSEMBLY OF BINARY NANOPARTICLES IN AN ELECTRIC FIELD

Self-assembly of nanoparticles into superlattice structures is a promising approach to construct functional materials or novel devices [32-34]. Among a variety of driving forces for self-assembly, electrostatic interaction plays an important role due to its long-range nature and simplicity of control [39]. Electric field can cause organized nanostructures in an electroreological (ER) fluid which is composed of nanoparticles dispersed in a nonconducting liquid. The monodispersed spherical particles tend to line up and form a chain parallel to the applied field [42]. Such a behavior can be attributed to the electric polarization interaction, a pair-wised dipolar interaction, between particles. The potential energy of the system depends on the orientation of the superlattice with respect to the applied field, the arrangement of the particles, and the distance between the particles. Tao *et al*. [84] suggested that under a strong field the ground state of the superlattice has a body-centered-tetragonal (BCT) structure, which has been observed in simulations [85] and experiments [86]. The phase diagram for dipolar hard spheres

obtained from Monte Carlo simulations shows the possibility of multiple phases including fluidic, face-centered-cubic, hexagonal-close-packed, and BCT phases [87].

The superlattice structures of binary nanoparticles can lead to a wide class of nanocomposite materials with properties not attainable by a single particle component. The behavior of binary nanoparticles in an electric field is still not well understood. The goal of this paper is to elucidate how parameters such as relative permittivity, volume fraction and particle size can be utilized to tune the superlattice structures.

3.1 MODELS

3.1.1 Brownian dynamics

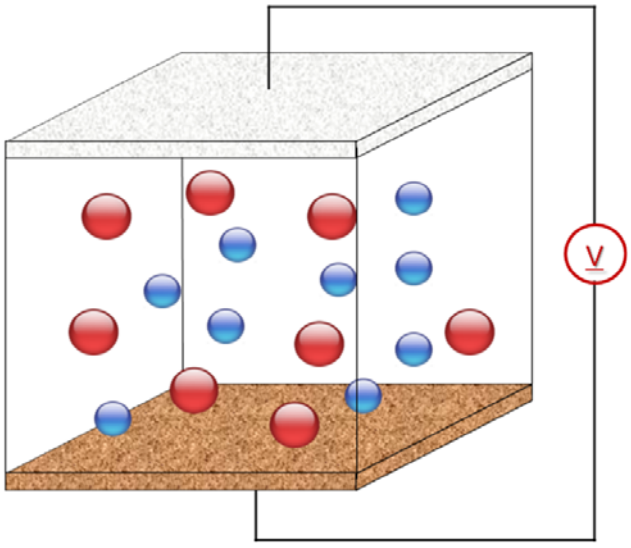

Figure 3.1 A schematic diagram of binary nanoparticles under an electric field. Initially, the particles are in random distribution.

For nanocrystals suspended in a solvent shown in Figrue 3.1, diffusive motions are typically observed in quiescent state. To model nanoparticle interactions in that state, the Brownian dynamics method [88] is used without explicitly considering the solvent particles. The solvent influences the behavior of the nanoparticles through random collisions and through imposing a frictional drag force on the motion of the nanoparticles. The trajectories of the nanoparticles are governed by the Langevin equation, $m_i\ddot{\mathbf{r}}_i(t) = \mathbf{F}_i^D + \mathbf{F}_i^R(t) + \mathbf{F}_i^E$. Here m_i and $\mathbf{r}_i$ denote the mass and position of particle i. The inertia term can be neglected for nanoparticles due to the small size and corresponding low Reynolds numbers. The force $\mathbf{F}_i$, which acts on the particle, includes drag force, random force, and electrostatic force expressed by superscript *D*, *R*, and *E*, respectively. Stoke's law gives $\mathbf{F}_i^D(t) = -3\pi\eta d_i \mathbf{V}_i(t)$, where η is the viscosity of the medium, d_i is the diameter, and $\mathbf{V}_i(t)$ is the velocity of particle i. The random force $\mathbf{F}_i^R(t)$ has a Gaussian distribution and obeys the fluctuation dissipation theorem[88], yielding $\left\langle \mathbf{F}_i^R(t) \cdot \mathbf{F}_j^R(t') \right\rangle = 6\pi\eta d_i k_B T \delta(t-t')$, where t and t' are time, k_B is Boltzmann's constant, and T is the temperature. The dipolar interaction energy between two dipoles, i at $\mathbf{r}_i$ and j at $\mathbf{r}_j$, is given by

$$U_{ij}(\mathbf{r}_{ij}) = [\mathbf{p}_i \cdot \mathbf{p}_j - 3(\mathbf{n}\cdot\mathbf{p}_i)(\mathbf{n}\cdot\mathbf{p}_j)]/(4\pi\varepsilon_m |\mathbf{r}_i - \mathbf{r}_j|^3) \tag{3.1}$$

where $\mathbf{p}_i = (\pi d_i^3/2)\varepsilon_m \alpha_i \mathbf{E}$ is the induced dipole in particle *i* under an applied electric field $\mathbf{E}$. Here, $\alpha_i = (\varepsilon_i - \varepsilon_m)/(\varepsilon_i + 2\varepsilon_m)$ while ε_i and ε_m represent the dielectric permittivity of particle i and the medium, and $\mathbf{n}$ is a unit vector in the direction of $\mathbf{r}_i - \mathbf{r}_j$. The dipoles in the nanoparticles near the electrodes redistribute the charge configuration

in the electrode, as a result, they disturb the uniform electric field. To consider this effect, we employed the image-method. The image charges are placed systematically so that the isopotential condition on the electrodes can be satisfied. A dipole $\mathbf{p}_i$ in the particle at position $\mathbf{r}_i = (x_i, y_i, z_i)$ produces an finite number of image-dipoles at positions $(x_i, y_i, -z_i)$ and $(x_i, y_i, 2kL \pm z_i)$, where $k = \pm 1, \pm 2, \ldots$ is a non-zero integer. The induced images also interact with the dipole itself and other dipoles in-between the electrodes. We shall assume the particles and the electrodes are "hard", so a short-range repulsive force is introduced between a particle and an electrode as well as between two particles. In order to reduce computational cost, a combination of Verlet list and cell lists method[89], with a cut-off length, is adopted. In the simulations, the periodic boundary conditions are used in x, y directions. The simulations are performed on the dimensionless parameter. We use a subscript '1' to denote a reference particle, where its diameter d_1 defines the length scale. The competition between electrostatic force and the drag force defines a time scale, $\tau = \eta_1 / (\varepsilon_m (\alpha_1 E)^2)$. Here, $\alpha_1 E$ can be treated as an effective electric field. The electrostatic force versus the random force defines a dimensionless number, $\Lambda = d_1^4 \alpha E \sqrt{\varepsilon_m / k_B T}$, which determines the behaviors of the nanoparticles. A larger electric field or particle diameter reduces the relative contribution from Brownian motion. However, Brownian motion can shake the nanoparticles to avoid trapping them into a local minimum. Nevertheless, a system may lose its order when Λ is too small due to the random movement of the particle, so an appropriate Λ could be helpful to form a more ordered structure.

3.1.2 Interactions

Next, let us define the permittivity ratios of the particles '1' and '2' to that of the medium by $\beta_1 = \varepsilon_1 / \varepsilon_m$ and $\beta_2 = \varepsilon_2 / \varepsilon_m$. Equation (3.1) suggests that the direction of an induced dipole is aligned with the applied field ($\beta_1 > 1$) or opposite to the applied field ($\beta_1 < 1$). Also, the interactive energy between two dipoles is proportional to $p_1 p_2 (1 - 3\cos^2\theta)$, where θ is the angle between the unit vector in the direction of two dipoles and the applied field. For a monodispersed system, the energy will always be minimized when the two particles line up along the direction of the electric field so that $\theta = 0$ or $\theta = \pi$, no matter whether they are more polarizable than the medium or not. As a result, the nanoparticles form chains spanning the electrodes. For a binary nanoparticle system, however, the chain formation is strongly dependent on the ability of polarization of the nanoparticles compared with that of the surrounding medium, which can be summarized into two cases: 1) Both of the particles are more polarizable ($\beta_1, \beta_2 > 1$) or less polarizable ($\beta_1, \beta_2 < 1$) than the medium; 2) One particle is more polarizable than the medium ($\beta_1 > 1$) while the other is less polarizable ($\beta_2 < 1$)

In the first case, the interactive energy is minimized when two particles line up along the electric field, which is similar to the case of the monodispersed system. As a result, the nanoparticles tend to form a chain along the direction of the field. Eventually, the chain can span the electrodes if there are enough particles. In this way, multiple chains form simultaneously. Consider two chains, each of them is composed of two particles. There are just two possible arrangements; either each chain is composed of

same particle, or both of the chains are composed of two different particles. Comparing the system energy from Eq. (3.1) can verify that the formation of pure chains, each of them is composed of single kind of particles, is energetically favorable. When two chains are close, the interaction depends on their relative position; it could be attractive or repulsive. From Eq. (3.1), the interaction is attractive when $\theta < 54.7^{\circ}$ or $\theta > 125.3^{\circ}$, and repulsive when $54.7^{\circ} < \theta < 125.3^{\circ}$. Thus, this attraction may drive chains to assemble into columns. Furthermore, as Halsey suggested, thermal fluctuations may lead to the coarsening process via a long-range, power-law interaction between chains spanning the electrodes.

In the second case, however, the opposite direction of the polarization leads to an interactive energy scales as $-|p_1 p_2|(1-3\cos^2\theta)$. Thus the energy is lower when $\theta = 90^{\circ}$; Two particles would prefer to be in a plane perpendicular to the applied field and attract each other. As a result, chains of alternating particles of both kinds are formed, oriented across the field. For the interactions between the same nanoparticles, the situations are the same as the case of pure single nanoparticle, so chains are formed along the applied field direction.

3.2 SIMULATION RESULTS

3.2.1 Lossless nanoparticles

Representative results are shown in Figure 3.2, which shows three-dimensional views (left column) and top views (right column) of the structures. The systems were allowed to evolve for a long time until no significant changes in the potential energy could be observed. The two kinds of particles are denoted by red (subscript 1) and blue (subscript 2) colors. They have the same diameter and are both more polarizable than the medium with $\beta_1 = 50$ and $\beta_2 = 5$ (Figure 3.2(a), (b)). The spacing between the electrodes is $L = 14d_1$ and the box size is $27d_1 \times 27d_1 \times 14d_1$. The system has $N = 2000$ particles (Figure 3.2(a)) and $N = 6000$ particles (Figure 3.2(b)). Thus the volume fractions of the particles are 10.3% and 30.8%, respectively. Under these situations, the particles assemble into isolated columns with a core-shell configuration. The core is composed of the more polarizable red particles, while the shell is composed of the blue ones. From an energetic point of view, the attraction between two red particle chains is stronger than the interaction between a red particle chain and a blue particle chain. As a result, the red chains aggregate to form columns. The blue chains tend to get close to the red columns as much as possible, leading to the formation of shells. It is important to note that this self-organized functionally gradient structure offers a gradual transition of the permittivity from the core to that of the medium. This approach could be potentially very useful to construct functional gradient nanocomposites using a bottom up methodology. Figure

3.2(b) shows the results for the higher volume fraction of particles. The system evolves into a continuous structure with isolated holes in between. The blue particles enclose the red particles, and form the peripheral regions around the holes. We have observed from the simulation that the particle columns demonstrate local BCTs and sheet-like structures which were already observed from experiments[90]. Figure 3.1(c) demonstrates the case, where the red particle is more polarizable than the medium while the blue particle is less polarizable. The parameters are the same as those in Figure 3.2(a) except for $\beta_1 = 2.8$ and $\beta_2 = 0.28$. The particles also form pure chains along the field direction with each chain composed of single kind of particles. A distinct feature in Figure 3.2(c) is that the red and blue chains are highly dispersed and form an alternating network. This morphology is in contrast to that in Figure 3.2(a), where the same color chains aggregate.

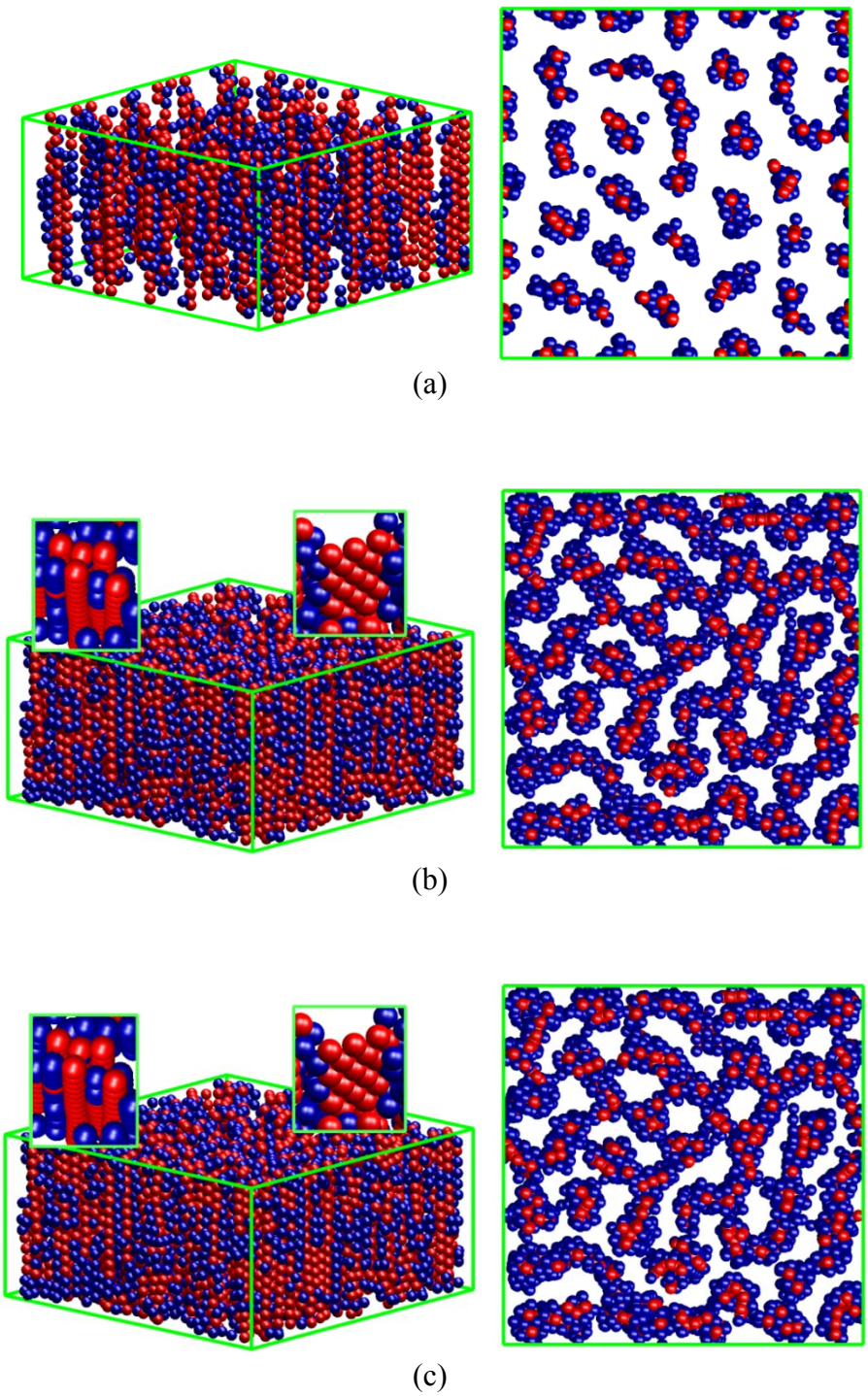

Figure 3.2 Fig. 1 The 3D views (left column) and top views (right column) of structures by red (subscript 1) and blue (subscript 2) particles. (a) $\beta_1 = 50$, $\beta_2 = 5$, $\Lambda = 175$, $N = 2000$ (b) $\beta_1 = 50$, $\beta_2 = 5$, $\beta_2 = 5$, $\Lambda = 175$, $N = 6000$ (c) $\beta_1 = 2.8$, $\beta_2 = 0.28$, $\Lambda = 175$, $N = 2000$

As mentioned before, the opposite dipole directions cause the red and blue particles to stay in a plane perpendicular to the field direction, which minimizes the interactive energy with $\theta = 0$. In the plane the same kind of particles repel each other while different kind particles attract each other. As a result, particles appear more dispersed.

3.2.2 Annealing process

One obstacle in generating a well-organized superlattice, composed of binary particles, is that two particles interact with each other simultaneously. We have found that an annealing process can promote the structure order. Figure 3.3(a) shows the mean square displacement of the binary system. The average square displacement of the nanoparticles is proportional to the translational diffusion coefficient, D_t, and time. At a specific value of Λ, the 'A' particles which have larger permittivity become solidified and well-ordered, and the 'B' particles, which have less permittivity, remain in a liquid state because the interaction between 'B' particles is weak. As a result, the 'A' particles form crystal structures first. Then, through the quenching of the system, 'B' particles also form similarly well-organized superlattices. Quenching the system can be accomplished by decreasing the temperature or by increasing the electric field. Figure 3.3(b) shows the structure formed by an annealing process. As can be seen in the figures, the structures in Figure 3.3(b) are more isolated than those in Figure 3.2(a), and the red particles occupy the center of each isolated structure more than in the case of Figure 3.2(a).

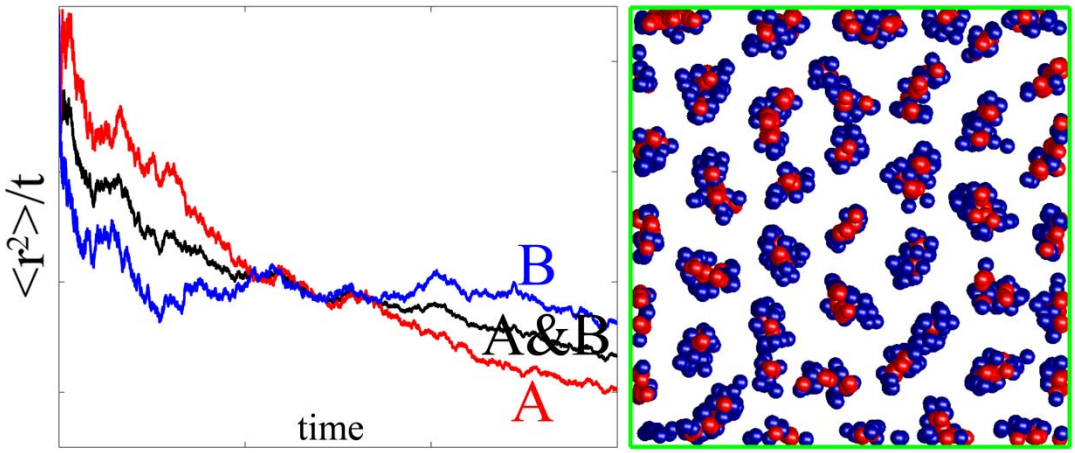

(a) (b)

Figure 3.3 An annealing process (a) The mean square displacement of each particle (A, B) and total particles (A&B), $\beta_1 = 50$, $\beta_2 = 5$, $\Lambda = 100$, $N = 2000$, (b) Top view of the final structure after quenching ($\Lambda = 500$), $\beta_1 = 50$, $\beta_2 = 5$, $N = 2000$

3.2.3 Single layer

Assembling a single layer of nanoparticles on a substrate has many potential applications. Relevant simulations are shown in Figure 3.4(a) and (b) for a layer of two kinds of particles. The parameters are the same as those in Figure 3.2(a) except that the diameter of the red particle becomes three times as large, and the system is much more dilute with 16 red particles among 200. Equation (3.1) suggests that the interaction increases quickly as the particle diameter also increases. Thus stronger interactions between red particles are expected. Initially, we put the red and blue particles randomly between the electrodes which are located vertically (Figure 3.4(a)) and horizontally

(Figure 3.4(b)). When the electrodes are located vertically, as time goes on, the repulsion between the red particles leads them to form a nicely ordered triangular lattice. The attraction between the blue and red particles causes the formation of blue rings surrounding the red cores. When the electrodes are located horizontally (Figure 3.4(b)), the red particles connect vertically first, then blue particles form chains and attach to the red particle chains.

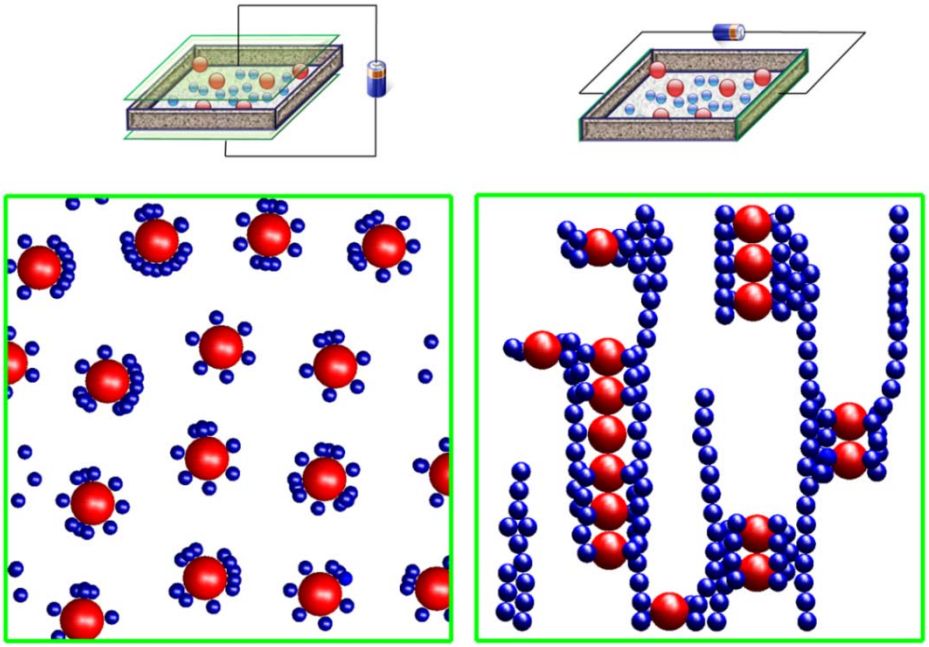

(a) (b)

Figure 3.4 Top view of structures in a single layer $\beta_1 = 50$, $\beta_2 = 5$, $\Lambda = 50$, $N = 200$ (a) The electrodes are in vertical direction (b) The electrodes are in horizontal direction

3.2.4 Frequency effects

In general, nanoparticles and the surrounding medium are not ideal dielectrics. In this case, we must take into account the electric conductivity. The response of a lossy dielectric to an external field depends on the frequency since the material's polarization does not respond instantaneously to the applied field. This property provides one with more powerful tools to control the morphologies of the nanostructures. Although the system is intrinsically dissipative, there is an effective potential energy for the particle interaction. The complex effective dipole moment can be expressed as $\mathbf{p}_i = (\pi d_i^3 / 2)\,\mathrm{Re}[\tilde{\varepsilon}_m]\tilde{\alpha}_i \mathbf{E}$, where $\tilde{\alpha}_i = (\tilde{\varepsilon}_i - \tilde{\varepsilon}_m)/(\tilde{\varepsilon}_i + 2\tilde{\varepsilon}_m)$, $\tilde{\varepsilon}_i = \varepsilon_i + \sigma_i / j\omega$, $\tilde{\varepsilon}_m = \varepsilon_m + \sigma_m / j\omega$, ω is the frequency of the field, $j = \sqrt{-1}$, and σ_i and σ_m are the conductivity of particle *i* and the medium. The time average of the energy can be evaluated as $U_{ij} = -1/2\,\mathrm{Re}[\mathbf{p}_i^* \cdot \mathbf{E}_j]$. Here $\mathbf{p}_i^*$ denotes complex conjugate of $\mathbf{p}_i$. The induced field, $\mathbf{E}_j$, due to the dipole $\mathbf{p}_j$ is $\mathbf{E}_j(\mathbf{r}) = \left(3\mathbf{n}(\mathbf{p}_j \cdot \mathbf{n}) - \mathbf{p}_j\right) / \left(4\pi\,\mathrm{Re}[\varepsilon_m]|\mathbf{r}|^3\right)$ [91]. Consequently, we have a similar expression as the Eq. (3.1) for the effective dipolar interaction between lossy particles,

$$U_{ij}(\mathbf{r}_{ij}) = \mathrm{Re}[\tilde{\alpha}_i^* \tilde{\alpha}_j]\left(1 - 3\cos^2\theta\right)/(4\pi\,\mathrm{Re}[\varepsilon_m]|\mathbf{r}_i - \mathbf{r}_j|^3)E_{rms}^2 \qquad (3.2)$$

where E_{rms} indicates the root mean square of $|\mathbf{E}|$. Here, one important feature to note is that the factor, $\mathrm{Re}[\tilde{\alpha}_i^* \tilde{\alpha}_j]$, can be positive, negative, or zero depending on the frequency. In Figure 3.5(a), $\mathrm{Re}[\tilde{\alpha}_i^* \tilde{\alpha}_j]$ is plotted for a strontinum-titanate nanoparticle ('A') and a zeolite nanoparticle ('B'). A negative value of $\mathrm{Re}[\tilde{\alpha}_i^* \tilde{\alpha}_j]$ means that the energy is lower

when $\theta = 90^{\circ}$, which is similar to the case of Figure 3.2(c). Two different particles would prefer to be in a plane perpendicular to the applied field and attract each other. In a specific frequency range, which is shown in Figure 3.5(a) with a shaded box area in the region II, the interaction between two different particles is very weak. At those frequencies, the two different nanoparticles form chains independently. The structures in Figure 3.5(b) are the result of shifting the frequency from range II to range III. Initially they grow and form columns independently, then, those different kinds of columns attract each other after shifting the frequency. These structures are different from those of Figure 3.2(c). The thick columns are alternating in Figure 3.5(b), while single chains are alternating in Figure 3.2(c).

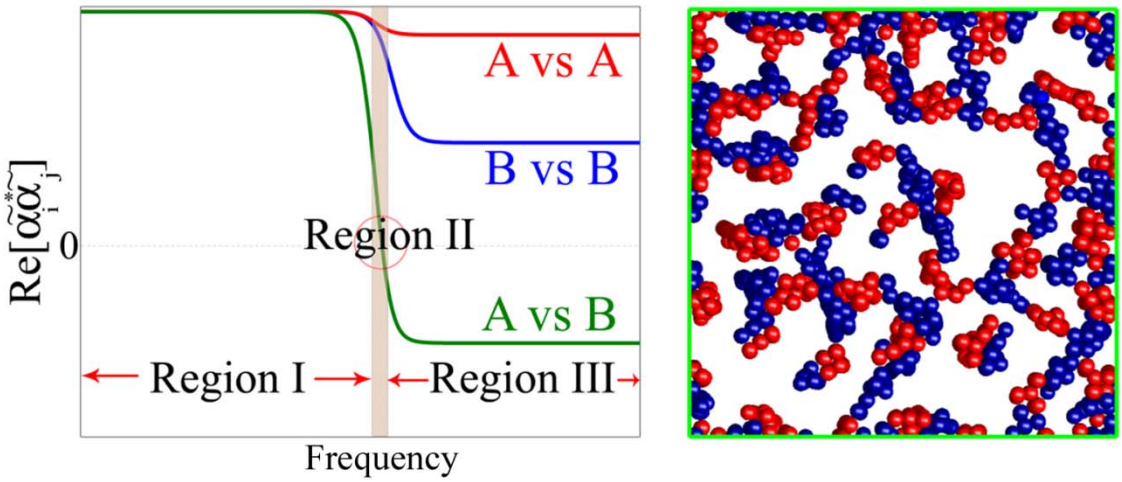

Figure 3.5 The frequency effect (a) Re[$\tilde{\alpha}_i^* \tilde{\alpha}_j$] for strontinum-titanate nanoparticle ('A') and zeolite nanoparticle ('B') (b) Top view of the final structure after shifting the frequency from region II to region III , $\beta_1 = 294$, $\sigma_1 / \sigma_m = 2 \times 10^5$, $\beta_2 = 23.7$, $\sigma_1 / \sigma_m = 1.5 \times 10^8$, $\Lambda = 50$, $N = 2000$

3.3 SELF-ASSEMBLY OF NANOPARTICLES CONCLUSIONS

In summary, our model shows several essential features of the structures formed by binary nanoparticle system under an electric field. Those structures may have different physical properties, for instance, electric conductivities and optical properties. Consequently, organizing different nanoparticles systematically into ordered binary superlattices can lead to functional materials. The predicted structures may provide some critical insight into designing materials indispensible for making such engineered structures feasible.

CHAPTER 4

INTERACTION OF POLY (AMIDOAMINE) DENDRIMERS WITH LIPID BILAYERS

Poly (amidoamine) dendrimer nanoparticles are used extensively in diverse areas of biology and medicine such as gene and drug delivery to disrupt cell membranes and allow the transport of material into cells. The size and surface chemistry of the nanoparticle have a strong influence on the interaction between a dendrimer and a membrane. Theoretical models and computer simulations have provided useful tools to elucidate these interactions between dendrimers and membranes. Atomistic molecular

dynamics [92, 93] have revealed maximum details but are restricted to small length and time scale. To overcome those limitations, Lee *et al.* [94] employed a coarse-grained (CG) model for the interactions between G3 and G5 PAMAM dendrimers and lipid bilayers. However, the simulation time is only 0.5 μs, which is still not enough to cover the experimental observation time ranges of a few minutes. Furthermore, the calculation for a larger system including G7 dendrimer and explicit water solvation is currently too computationally demanding. Our objective in the present work is to elucidate the interactions between dendrimers and a membrane with less of a limitation on the length and time scale. We also seek a way to provide the physical understanding for the mechanism from the fundamental principles of thermodynamics. For this purpose, we adopt the phase-field approach, which has recently emerged as a powerful computational approach to modeling and predicting nanoscale morphological and microstructure evolution in materials [95, 96] and biology [97]. The system evolution takes place to reduce the total free energy that may include the chemical bulk energy, interfacial energy, and elastic strain energy. The dendrimer nanoparticles presented in this research include the G7-dendrimer and G5-dendrimer, which have two types of end-groups: one is an amine-terminated (R-NH_2) dendrimer which has positive charges at the surface, and another is an acetamide-terminated (R-$NHC(O)CH_3$) dendrimer which has a neutral surface.

4.1 MODELING

In this section we propose a three-dimensional phase field model for the interaction between a dendrimer and a membrane. This interaction can be ascribed to minimizing the free energy in the system. The total free energy of the system depends on the phase configurations. Here, we incorporated the energy of phase separation, interfacial energy, and elastic energy such as bending energy and stretching energy. We denote the volume fraction of dendrimer and membrane in the water by c_1 and c_2 respectively. Consequently, the water site is $1-c_1-c_2$. Here, c_1 and c_2 are spatially continuous and time dependent functions, namely, $c_1 = c_1(\mathbf{x},t)$ and $c_2 = c_2(\mathbf{x},t)$, where $\mathbf{x}$ is a position vector. Note that $c_1(\mathbf{x},t) = 1$ and $c_2(\mathbf{x},t) = 0$ for the dendrimer, $c_1(\mathbf{x},t) = 0$ and $c_2(\mathbf{x},t) = 1$ for the membrane. The total free energy of the system is the sum of the four types of energy which comprise the system,

$$G = G_{\text{che}} + G_{\text{gra}} + G_{\text{bd}} + G_{\text{st}} \tag{4.1}$$

where G_{che} is the chemical bulk energy, G_{gra} is the phase interfacial (gradient) energy, G_{bd} is the elastic bending energy, and G_{st} is the elastic stretching energy. The chemical bulk energy, G_{che}, is given by

$$G_{che} = \int_{\Omega} f(c_1, c_2) d\Omega \tag{4.2}$$

where Ω represents the whole domain of the system. This energy drives the separation of each phase. For the ternary material system, we adopt Muggianu's equation[98] given by,

$$f = c_1 f_d + c_2 f_m + (1-c_1-c_2) f_w + \overline{f} \tag{4.3}$$

where $\overline{f} = f_0\{c_1 \ln c_1 + c_2 \ln c_2 + (1-c_1-c_2)\ln(1-c_1-c_2) + c_1c_2\left[\Omega_{12}^0 + \Omega_{12}^1(c_1-c_2)\right]$

$+c_2(1-c_1-c_2)\left[\Omega_{23}^0 + \Omega_{23}^1(c_1+2c_2-1)\right] + c_1(1-c_1-c_2)\left[\Omega_{13}^0 + \Omega_{13}^1(2c_1+c_2-1)\right]\}$

Here, f_d, f_m, and f_w represent the excess energy when the system is composed of only the dendrimer, the membrane, or the medium. The average concentration is constant due to the mass conservation; hence the linear term of excess energy does not affect diffusion and can be neglected. In the equation, k_B is Boltzmann's constant and T is the absolute temperature. The interface energy, G_{gra}, among the dendrimer, the membrane, and the medium can be established through gradient terms of c_1 and c_2.

$$G_{\text{int}} = \int_\Omega \left(h_{11}(\nabla c_1)^2 + h_{12}\nabla c_1 \cdot \nabla c_2 + h_{22}(\nabla c_2)^2\right) d\Omega \tag{4.4}$$

where h_{11}, h_{12}, and h_{22} are the material constant. The elastic bending energy is given by Helfrich [99], $G_{bd} = \int_S 0.5K_B(2H)^2 dA$, where S represents the surface of each phase and K_B are elastic constant for bending, and H is the mean curvature. The elastic stretching energy is given by Helfirich [99], $G_{st} = \int_S 0.5K_S\left(\Delta S / S_0\right)^2 dA$, where K_S is stretching elasticity modulus and $\Delta S / S_0$ represents the excess area.

The phase field variable $c(\mathbf{x},t)$ can be expressed as a functional of a signed-distance function, $di(\mathbf{x})$, satisfying $di(\mathbf{x}) = 0$ for $\mathbf{x} \in \Gamma$, and $di(\mathbf{x})$ is negative distance for inside domain and is positive distance for outside domain. Here Γ represents the surface of the domain. Also, when the interfacial thickness is very small, the functional is approaching to a 'tanh' function form[97],

$$c(\mathbf{x}) = \frac{1}{2}\left(\tanh\left[\frac{di(\mathbf{x})}{\sqrt{2}\tau} \right] + 1 \right) = g\left(\frac{di(\mathbf{x})}{\sqrt{2}\tau} \right) \tag{4.5}$$

where τ denotes the thickness of an interface. From the relationship $\tanh'(x) = 1 - \tanh^2(x)$, $\tanh''(x) = -2\tanh(x) \times \left(1 - \tanh^2(x)\right)$,

$$g'(x) = \frac{1}{2}\left[1 - 4\left(g(x) - \frac{1}{2} \right)^2 \right],\ g''(x) = -2\left(g(x) - \frac{1}{2} \right)\left[1 - 4\left(g(x) - \frac{1}{2} \right)^2 \right] \tag{A.6}$$

Also, from Eq. (4.5)

$$\nabla c(\mathbf{x}) = g' \frac{\nabla di(\mathbf{x})}{\sqrt{2}\tau}, \nabla^2 c(\mathbf{x}) = g'' \frac{\left(\nabla di(\mathbf{x})\right)^2}{2\tau^2} + g' \frac{\nabla^2 di(\mathbf{x})}{\sqrt{2}\tau} \tag{4.7}$$

The normal vector $\mathbf{n}$ is express as $\mathbf{n} = \nabla di(\mathbf{x})$, which yields $(\nabla di(\mathbf{x}))^2 = \mathbf{n} \cdot \mathbf{n} = 1$. From Eq. (4.7),

$$\nabla^2 di(\mathbf{x}) = \frac{\sqrt{2}\tau}{g'}\left(\nabla^2 c(\mathbf{x}) - \frac{g''}{2\tau^2} \right) \tag{4.8}$$

The mean curvature H can be written in terms of the phase field variable $c(\mathbf{x})$ as

$$H = \frac{1}{2}\nabla^2 di(\mathbf{x}) = \frac{\sqrt{2}\tau}{2g'}\left[\nabla^2 c(\mathbf{x}) - \frac{g''}{2\tau^2} \right] = \frac{\sqrt{2}\tau}{1 - 4(c - \frac{1}{2})^2}\left[\nabla^2 c + \frac{(c - \frac{1}{2})}{\tau^2}\left(1 - 4(c - \frac{1}{2})^2 \right) \right] \tag{4.9}$$

The bending energy is

$$G_{bd} = \int_\Gamma \frac{K_B}{2}(2H)^2 dA \tag{4.10}$$

Using the relationship $\int_{-\infty}^{+\infty}\left[1 - \tanh^2\left(\frac{x}{\sqrt{2}\tau} \right) \right]^2 dx = \frac{4\sqrt{2}\tau}{3}$,

$$G_{bd} = \frac{3}{4\sqrt{2}\tau}\int_{-\infty}^{+\infty}\left[1 - \tanh^2\left(\frac{x}{\sqrt{2}\tau} \right) \right]^2 dx \int_\Gamma \frac{K_B}{2}(2H)^2 dA \tag{4.11}$$

From the lemma [100],

$$G_{bd} = \frac{3}{\sqrt{2}}\tau K_B \int_\Omega \left[\nabla^2 c + \frac{(c-1/2)}{\tau^2}\left(1-4(c-1/2)^2\right)\right]^2 d\Omega \tag{4.12}$$

Similarly, the stretching energy can be obtained with the following steps. From Eq. (4.7),

$$\nabla di(\mathbf{x}) = \frac{2\sqrt{2}\tau}{\left[1-4\left(c-1/2\right)^2\right]}\nabla c \tag{4.13}$$

The excess area, $\Delta S / S_0$, can be written as

$$\frac{\Delta S}{S_0} = \frac{1}{2}\left(\nabla di(\mathbf{x})\right)^2 = \frac{4\tau^2}{\left[1-4\left(c-1/2\right)^2\right]^2}\left(\nabla c\right)^2 \tag{4.14}$$

The stretching energy is

$$G_{st} = \int_\Gamma \frac{1}{2} K_s \left(\frac{\Delta S}{S_0}\right)^2 dA \tag{4.15}$$

$$G_{bd} = \frac{3}{8\sqrt{2}\tau} K_s \int_\Omega \left[\frac{4\tau^2}{\left(1-4\left(c-1/2\right)^2\right)}\left(\nabla c\right)^2 \right]^2 d\Omega \tag{4.16}$$

Again, from the relations $\mathbf{n} = \nabla di$ and $\mathbf{n}\cdot\mathbf{n} = 1$,

$$\left[1-4\left(c-1/2\right)^2\right]^2 = 8\tau^2\left(\nabla c\right)^2 \tag{4.17}$$

From Eq. (4.16) we can rewrite the stretching energy,

$$G_{st} = \frac{3}{4\sqrt{2}}\tau K_s \int_\Omega \left(\nabla c\right)^2 d\Omega \tag{4.18}$$

Consequently,

$$G_{bd,i} = \frac{3}{\sqrt{2}}\tau K_{B,i} \int_\Omega \left[\nabla^2 c_i + \frac{(c_i-1/2)}{\tau^2}\left(1-4(c_i-1/2)^2\right)\right]^2 d\Omega \tag{4.19}$$

$$G_{st,i} = \frac{3}{4\sqrt{2}} \tau K_{s,i} \int_{\Omega} \left(\nabla c_i \right)^2 d\Omega \tag{4.20}$$

where the subscript i indicates the phase i (1 or 2). Here $K_{B,1}$ and $K_{B,2}$ are bending modulus, and $K_{S,1}$ and $K_{S,2}$ are stretching modulus for the dendrimer and the membrane, respectively. The phase field model constitutes sets of kinematics and kinetics. The mass conservation requires that the time rate of the concentration c_i compensates the divergence of the flux vector, $\mathbf{J}_i(\mathbf{x},t)$, namely,

$$\frac{\partial c_i(\mathbf{x},t)}{\partial t} = -\nabla \cdot \mathbf{J}_i(\mathbf{x},t) \tag{4.21}$$

Following Cahn and Hilliard [101], we assume that the atomic flux is linearly proportional to the driving force, $\mathbf{F}_i$. The corresponding driving force is $\mathbf{F}_i = -\nabla \mu_i$, where μ_i is the chemical potential for each phase. Diffusion flux from the mass transport is given by $\mathbf{J}_i = M_i \mathbf{F}_i$ where M_i is the mobility of species i. This relationship combined with the mass conservation yields the diffusion equations,

$$\frac{\partial c_1}{\partial t} = \nabla \left(M_1 \nabla \mu_1 \right) \tag{4.22}$$

$$\frac{\partial c_2}{\partial t} = \nabla \left(M_2 \nabla \mu_2 \right) \tag{4.23}$$

Here, the chemical potential for each phase can be calculated from the definition, $\mu_1 = \delta G / \delta c_1$ and $\mu_2 = \delta G / \delta c_2$,

$$\mu_1 = f_1 - 2h_{11}\nabla^2 c_1 - h_{12}\nabla^2 c_2 + K_{B,1} g_{1,1} + K_{B,1}\nabla^2 g_{1,2} - \frac{3}{2\sqrt{2}} \tau K_{S,1} \nabla^2 c_1 \tag{4.24}$$

$$\mu_2 = f_2 - 2h_{22}\nabla^2 c_2 - h_{12}\nabla^2 c_1 + K_{B,2} g_{2,1} + K_{B,2}\nabla^2 g_{2,2} - \frac{3}{2\sqrt{2}} \tau K_{S,2} \nabla^2 c_2 \tag{4.25}$$

$$f_1 = f_0\Big[\ln(c_1/(1-c_1-c_2)) + \Omega_{12}^0 c_2 + \Omega_{12}^1(2c_1c_2 - c_2^2) - \Omega_{23}^0 c_2 + \Omega_{23}^1(-2c_1c_2 - 3c_2^2 + 2c_2) + \Omega_{13}^0(1-2c_1-c_2)\Big)$$
$$+\Omega_{13}^1(1-6c_1+6c_1^2-2c_2+6c_1c_2+c_2^2)\Big]$$

$$f_2 = f_0\Big[\ln(c_2/(1-c_1-c_2)) + \Omega_{12}^0 c_1 + \Omega_{12}^1(c_1^2 - 2c_1c_2) + \Omega_{23}^0(1-c_1-2c_2)$$
$$+\Omega_{23}^1(-1+2c_1-c_1^2+6c_2-6c_1c_2-6c_2^2) - \Omega_{13}^0 c_1 + \Omega_{13}^1(3c_1^2+2c_1c_2-2c_1)\Big]$$

$$g_{1,1} = 6\sqrt{2}\left(1-6c_1+6c_1^2\right)\left(2c_1-6c_1^2+4c_1^3-\tau^2\nabla^2 c_1\right)/\tau^3$$

$$g_{2,1} = 6\sqrt{2}\left(1-6c_2+6c_2^2\right)\left(2c_2-6c_2^2+4c_2^3-\tau^2\nabla^2 c_2\right)/\tau^3$$

$$g_{1,2} = 3\sqrt{2}\left(-2c_1+6c_1^2-4c_1^3+\tau^2\nabla^2 c_1\right)/\tau\,,\ g_{2,2} = 3\sqrt{2}\left(-2c_2+6c_2^2-4c_2^3+\tau^2\nabla^2 c_2\right)/\tau$$

4.2 NUMERICAL PROCEDURES

We normalize the Eq. (4.22), (4.23), (4.24) and (4.25) with a characteristic length L_c and time t_c. We select the characteristic length as the interface thickness, τ, in Eq. (4.5). A time scale is defined by $t_c = L_c^2/(M_1 f_0)$, where M_1 is the mobility of the dendrimer. The mobility of the dendrimer and the membrane are also normalized by that of the dendrimer. Dropping the index for normalization gives,

$$\frac{\partial c_1}{\partial t} = \nabla\cdot(M_1\nabla\mu_1) \tag{4.26}$$

$$\frac{\partial c_2}{\partial t} = \nabla\cdot(M_2\nabla\mu_2) \tag{4.27}$$

$$\mu_1 = p_1 - 2C_{h,11}^2\nabla^2 c_1 - C_{h,12}^2\nabla^2 c_2 + \kappa_1 q_{1,1} + \kappa_1\nabla^2 q_{1,2} - \frac{3}{2\sqrt{2}}\lambda_1\nabla^2 c_1 \tag{4.28}$$

$$\mu_2 = p_2 - 2C_{h,22}^2\nabla^2 c_2 - C_{h,12}^2\nabla^2 c_1 + \kappa_2 q_{2,1} + \kappa_2\nabla^2 q_{2,2} - \frac{3}{2\sqrt{2}}\lambda_2\nabla^2 c_2 \tag{4.29}$$

where $p_1 = f_1 / f_0$, $p_2 = f_2 / f_0$, $q_{1,1} = 6\sqrt{2}\left(1 - 6c_1 + 6c_1^2\right)\left(2c_1 - 6c_1^2 + 4c_1^3 - \nabla^2 c_1\right)$,

$q_{1,2} = 3\sqrt{2}\left(-2c_1 + 6c_1^2 - 4c_1^3 + \nabla^2 c_1\right)$, $q_{2,1} = 6\sqrt{2}\left(1 - 6c_2 + 6c_2^2\right)\left(2c_2 - 6c_2^2 + 4c_2^3 - \nabla^2 c_2\right)$,

$q_{2,2} = 3\sqrt{2}\left(-2c_2 + 6c_2^2 - 4c_2^3 + \nabla^2 c_2\right)$, $C_{h,11} = \sqrt{h_{11} / f_0} / \tau$, $C_{h,12} = \sqrt{h_{12} / f_0} / \tau$,

$C_{h,22} = \sqrt{h_{22} / f_0} / \tau$, $\kappa_1 = K_{B,1} / \left(f_0\tau^3\right)$, $\kappa_2 = K_{B,2} / \left(f_0\tau^3\right)$, $\lambda_1 = K_{S,1} / \left(f_0\tau\right)$, $\lambda_2 = K_{S,2} / \left(f_0\tau\right)$.

In order to track the evolution of Equations (4.26) and (4.27), we conduct a numerical simulation. The explicit forward-Euler method for the time variables in the equations requires a very small time step to maintain its stability. Instead, we adopt the semi-implicit scheme proposed by Chen *et al.* [102]. The key idea of this scheme is to treat the linear term implicitly and the nonlinear term explicitly to allow for larger time steps without losing numerical stability. The right hand side of Equations (4.26) and (4.27) can be rewritten as

$$\nabla\cdot(M_1\nabla\mu_1) = A\nabla^2\mu_{1lr} + s_{1\mu} \tag{4.30}$$

$$\nabla\cdot(M_2\nabla\mu_2) = A\nabla^2\mu_{2lr} + s_{2\mu} \tag{4.31}$$

where A is a constant, μ_{1lr} and μ_{2lr} are linear components of μ_1 and μ_2 respectively, and $s_{1\mu} = \nabla\cdot(M_1\nabla\mu_1) - A\nabla^2\mu_{1lr}$, $s_{2\mu} = \nabla\cdot(M_2\nabla\mu_2) - A\nabla^2\mu_{2lr}$. Here, the linear terms $A\nabla^2\mu_{1lr}$ and $A\nabla^2\mu_{2lr}$ are treated implicitly, and the terms $s_{1\mu}$ and $s_{2\mu}$ are treated explicitly. We have obtained numerical stability in the simulation by taking $\mu_{1lr} = c_1 - C_{h11}^2\nabla^2 c_1$,

$\mu_{2lr} = c_2 - C_{h22}^2 \nabla^2 c_2$ among different choices[103] and $A = 1$. Note that the stability is achieved in conjunction with the extrapolated gear (SBDF) scheme [104] for time integration. SBDF has the strongest high modal decay among the second order multi-step methods. This provides the required damping for the very high frequencies in the diffusion equation without a severe time-step constraint. Applying the semi-implicit method and the SBDF time integration scheme, we obtain the following discrete form for Equations (4.26), (4.27), (4.30), and (4.31),

$$\frac{3}{2}c_1^{n+1} - 2c_1^n + \frac{1}{2}c_1^{n-1} = A\Delta t \nabla \cdot A\left(\nabla^2 c_1^{n+1} - C_{h11}^2 \nabla^4 c_1^{n+1}\right) + 2Q_1^n - Q_1^{n-1} \tag{4.32}$$

$$\frac{3}{2}c_2^{n+1} - 2c_2^n + \frac{1}{2}c_2^{n-1} = A\Delta t \nabla \cdot A\left(\nabla^2 c_2^{n+1} - C_{h22}^2 \nabla^4 c_2^{n+1}\right) + 2Q_2^n - Q_2^{n-1} \tag{4.33}$$

where

$$Q_1^n = \Delta t\left(\nabla \cdot M \nabla \mu_1^n - A\nabla^2 c_1^n + AC_{h11}^2 \nabla^4 c_1^n\right), \quad Q_2^n = \Delta t\left(\nabla \cdot M \nabla \mu_2^n - A\nabla^2 c_2^n + AC_{h22}^2 \nabla^4 c_2^n\right) .$$

These equations can be solved with high spatial resolution efficiently in Fourier space. Applying a Fourier transform to the equations, we obtain

$$\hat{c}_1^{n+1} = \frac{4\hat{c}_1^n - \hat{c}_1^{n-1} + 4\hat{Q}_1^n - 2\hat{Q}_1^{n-1}}{3 + (2A\Delta t)(k^2 + C_{h11}^2 k^4)} \tag{4.34}$$

$$\hat{c}_2^{n+1} = \frac{4\hat{c}_2^n - \hat{c}_2^{n-1} + 4\hat{Q}_2^n - 2\hat{Q}_2^{n-1}}{3 + (2A\Delta t)(k^2 + C_{h22}^2 k^4)} \tag{4.35}$$

where

$$\hat{Q}_1^n = \Delta t\left[\sqrt{-1}\mathbf{k} \cdot \left\{M_1\left(\sqrt{-1}\mathbf{k}\hat{\mu}_1^n\right)_r\right\}_k + Ak^2\hat{c}_1^n + Ak^4 C_{h11}^2 \hat{c}_1^n\right],$$

$\hat{Q}_2^n = \Delta t\left[\sqrt{-1}\mathbf{k}\cdot\left\{M_2\left(\sqrt{-1}\mathbf{k}\hat{\mu}_2^n\right)_r\right\}_k + Ak^2\hat{c}_2^n + Ak^4C_{h22}^2\hat{c}_2^n\right]$. Here the caret ^ and subscript k denote a Fourier transform, and the subscript *r* denotes an inverse Fourier transform. The vector $\mathbf{k}$ denotes the wave vector in Fourier space with $k^2 = k_1^2 + k_2^2 + k_3^2$.

4.3 SIMULATIONS AND RESULTS

4.3.1 Simulation parameters

All the simulations are performed on a domain of $64\times64\times32$ grids with a grid space of L_c. First, a simulation with only a lipid layer is conducted, then a dendrimer is added to final configuration from the first simulation. Initially, the dendrimer touches the lipid bilayer. The diameter of the dendrimer is 8 nm and 5 nm, which represent a G7-dendrimer and a G5-dendrimer respectively. The thickness of lipid layer is about 5 nm, which is consistent with the dimyristorylphospatidylchonline (DMPC) membrane. The dimensionless numbers for the chemical bulk energy are set as $\Omega_{12}^0 = \Omega_{23}^0 = \Omega_{31}^0 = 3.5$ and $\Omega_{12}^1 = \Omega_{23}^1 = \Omega_{31}^1 = 1.0$. These parameters represent a function with three wells shown in Figure 4.1, which derives the phase separation.

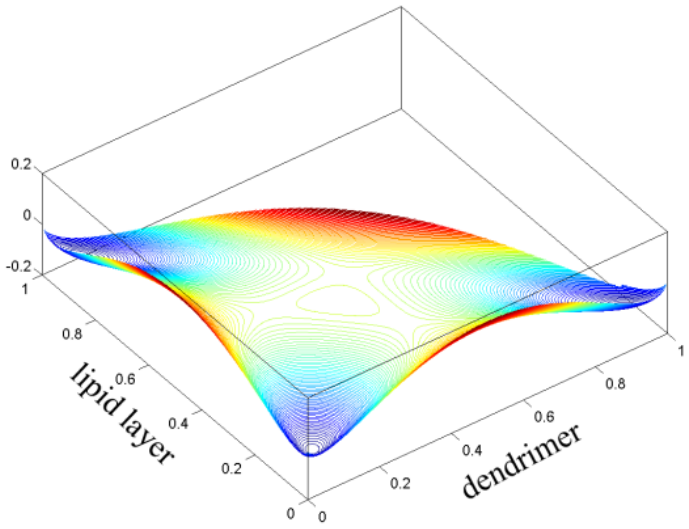

Figure 4.1 The chemical bulk energy function with three wells. It derives the phase separation.

The interface thickness, δ, in terms of the model parameters can be obtained as $\delta \sim \sqrt{h/W}$ [105], where h represent the constant in the gradient energy term. Here, W represent the height of the barrier between wells in the free energy density, f. In our model, $W \sim 0.18 f_0$. Then the surface energy can be obtained from a simplified interface profile. From Eq. (4.5) with an assumption of a flat interface, the surface energy, σ_{DM}, can be calculated from

$$\sigma_{DM} = \int_{-\infty}^{\infty} h\left(\frac{\partial c}{\partial x}\right)^2 dx \sim \frac{h}{\delta} \sim 0.43\sqrt{hf_0} \tag{4.36}$$

The surface energy for the dendrimer [106] and the membrane [107] are approximately $\sigma_{dend} \sim 7.3\times10^{-2}\, J/m^2$ and DMPC lipid layer $\sigma_{memb} \sim 4.2\times10^{-2}\, J/m^2$. In this model, we select an average value of the interface thickness for the dendrimer and the membrane to

be 1 nm. We estimate the parameters to be, $h_{11} \sim 9.15\times10^{-11} J/m$, $h_{22} \sim 3.03\times10^{-11} J/m$, $f_0 \sim 3.15\times10^{8} J/m^3$, and $\tau = 1nm$, which give $\mathrm{Ch}_{11} = 0.54$ and $\mathrm{Ch}_{22} = 0.31$. For the dendrimer [97], $K_{B,1} = 8\times10^{-19} J$ and $K_{S,1} = 2.6\times10^{-1} J/m^2$, which yield $\kappa_1 = 2.5$, $\lambda_1 = 0.83$. For a DMPC lipid layer [108], $K_{B,2} = 5.6\times10^{-20} J$ and $K_{S,2} = 1.45\times10^{-1} J/m^2$, which give $\kappa_2 = 0.2$ and $\lambda_2 = 0.46$.

Depending on the surface termination, the dendrimer can carry charges. The PAMAM dendrimer with amine- terminated (R-NH_2) branches carries a positive charge because its surface primary amines are protonated at pH <7 [109, 110], while an acetamide- terminated (R-$NHC(O)CH_3$) dendrimer has a neutral surface charge. The lipid bilayer in this research is dimyristoylphosphatidylcholine (DMPC). This particular lipid is zwitterionic, which means it has both a positive and negative charge, yielding a net neutral charge on its head. The negative charge of the head-group dipole is linked to the lipid chains that are firmly anchored in the hydrocarbon core of the lipid layer. Hence, this charge can be considered immobile as compared to the positively charged end of the head-group dipole which can move according to the conformational freedom of the headgroup [111]. Consequently, the dendrimer and membrane attract each other due to the attraction between the positive charge at the surface of the dendrimer and the negative charge at the membrane. The elastic stiffness of the membrane is smaller than that of dendrimer. As a result, the membrane near the dendrimer wants to encircle the dendrimer to reduce the electrostatic energy. This may be considered as minimizing the surface energy between the dendrimer and membrane. From this point of view, in this work, we vary the parameters, C_{h12}, to mimic the role of the dendrimers surface charge instead of

solving the electric field directly. We vary it from 0.9 (amine-terminated) to 1.7 (acetamide-terminated). This variation is expected to mimic experiments involved amine-terminated dendrimers carrying positive charges.

4.3.2 Simulation results

Representative results of the G7-amine PAMMA dendrimer are shown in Figure 4.2. From experiments, adding G7-amine PAMAM dendrimers to the lipid bilayer caused the formation of small, isolated holes. In our simulations, shown in Figure 4.2, the formation of a small hole is observed. As the dendrimer and the lipid layer interact, the strong attraction between the surface of the dendrimer and the lipid layer causes for the lipid layer to move to the dendrimer, then start to enclose the dendrimer. During this process, the elastic energy increases due to the bending and stretching of the membrane. Over the limit of the elastic (or plastic) deformation, the bonding between the membrane molecules is broken, then a large number of membrane molecules are pulled away from the original membrane. As a result, a hole is generated. This result is similar to a proposed model by Mecke *et al.* [56]. They argued that dendrimers pull lipid molecules off the substrate, leading to formation of dendrimer-filled vesicles. In the experiment, the particles are no longer attached to the substrate, so cannot be imaged by an AFM tip. From our simulation, we verify that the lipid layer forms stabilizing bonds with the dendrimer functional group. Consequently, the dendrimers-filled vesicle is able to self-assemble. A G7-acetamide PAMAM dendrimer, which is neutrally charged, similarly

caused a hole formation but resulted in a lower density of holes than for G7-amine from the experiments. This is also verified from the simulation. The hole generated from the G7-acetamide (Figure 4.3) is smaller than that from the G7-amine (Figure 4.2). Even thought there is no strong interaction such as the charge interaction, if the size of the dendrimer is large enough, the adhesive force from the van der Waals interaction can defeat the elastic energy and the cohesive forces, then pull the molecules off of the membrane. However, the number of the pulled-off molecules is smaller than in the case of the G7 amine-terminated dendrimer.

Next, from the experiment, the size of the dendrimer is also an important factor in the interaction between dendrimers and lipid bilayers. A lower generation G5-amine dendrimer had a greatly reduced ability to remove lipid molecules from the surface. Although G5-amine dendrimer removed the lipid layer, it did so more slowly and mostly from the edges of existing bilayer defects. Our simulation results also show these tendencies. As can be seen in Figure 4.4, the hole formation for the G5-dendrimer starts later than the case of the G7-dendrimer. Also, the size is much smaller than that of the G7-dendrimer. In order to form enough stabilizing bonds between the end-group of the dendrimer and the lipid molecules, the average number of lipid head groups per dendrimer end-group should be small[56]. It means that the number of lipid head group for one dendrimer end-group to pull off should be small. For a G7 PAMAM dendrimer, from the reference[56], this value is between 1 and 3; however, it reaches 6 for the G5 PAMAM dendrimer. This implies that a lower generation cannot remove the lipid molecules from the surface. Figure 4.5 shows the effect of a pre-existing bilayer defect.

The size of the hole generated from the edges of defect is larger than that from intact part of layer.

A G5-acetamide PAMAM dendrimer barely caused the formation or expansion of defects in the lipid layer. Instead, they caused the formation of ledges. In the simulations, as shown in Figure 4.6, the size of hole is very small and there is a well near the dendrimer.

The interaction between a single dendrimer and the lipid layer would not be strong enough to create a large hole in the bilayer, while the size of a hole in the experiment is larger than the size of a dendrimer. It is, however, possible that multiple dendrimers combined are able to remove lipids by forming larger aggregates. From the simulation results shown in Figure 4.7, we can verify this hypothesis. Here, we assumed the dendrimers are well distributed by the repulsive forces between the charges at the surface. The results of combined dendrimers are much larger than the hole from a single dendrimer.

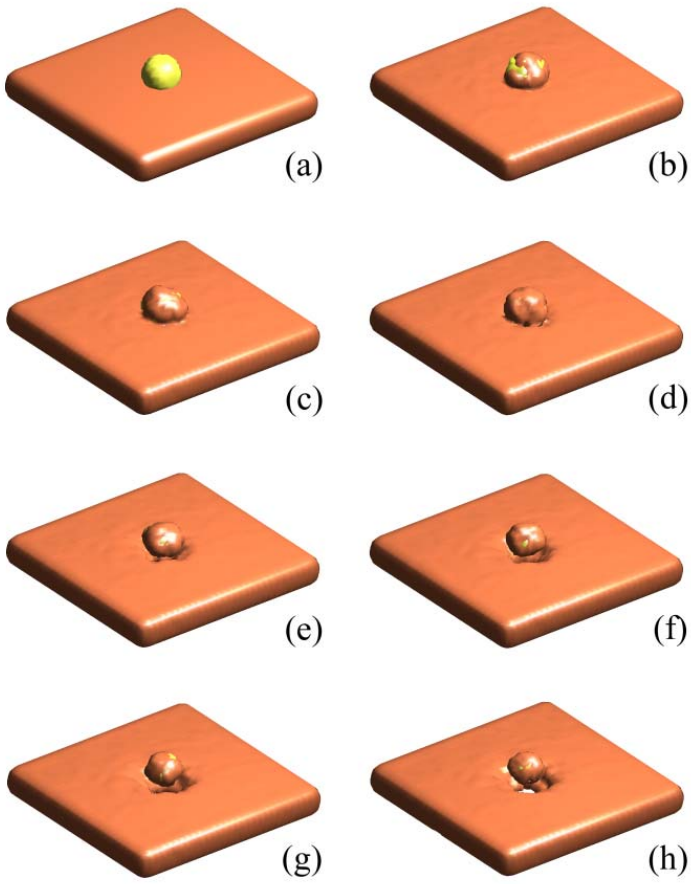

Figure 4.2 Evolution of the membrane with a G7 amine-terminated dendrimer. Each time step is $2t_c$.

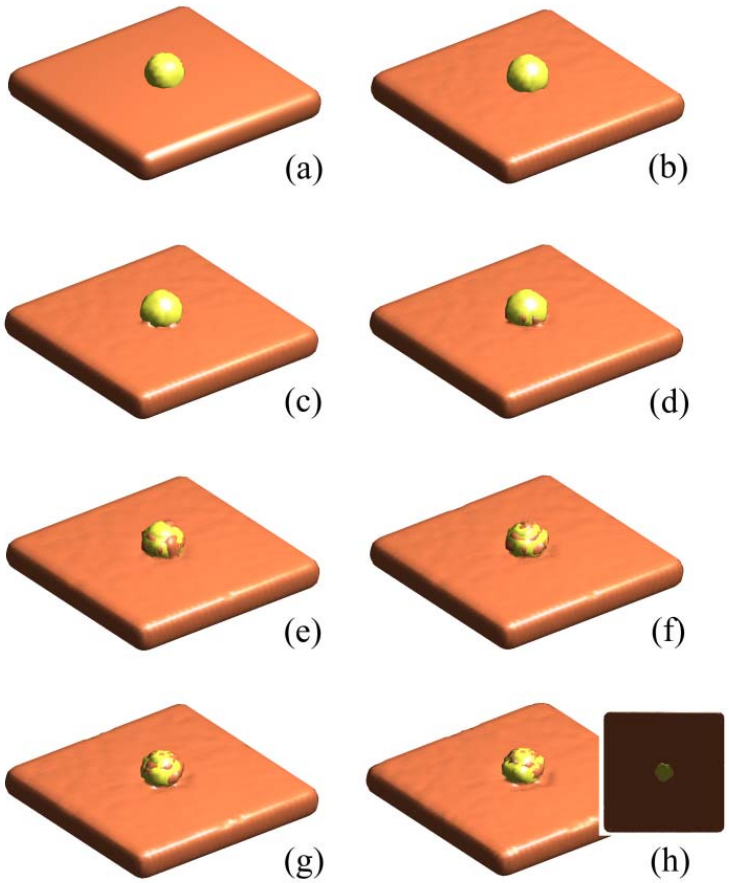

Figure 4.3 Evolution of the membrane with a G7 acetamide-terminated dendrimer. The right part of (h) shows a hole viewed from the bottom. Each time step is $2t_c$.

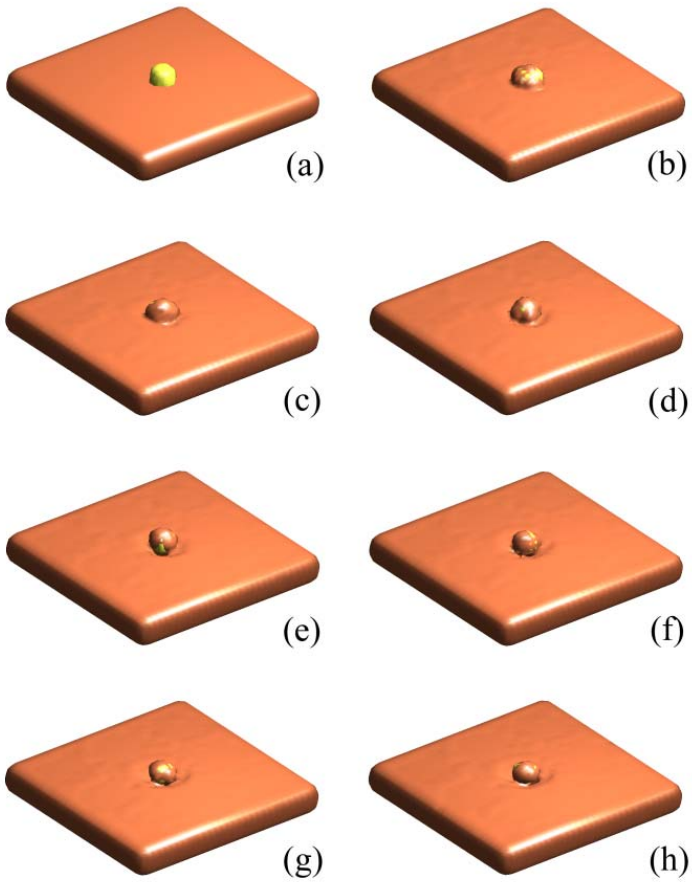

Figure 4.4 Evolution of the membrane with a G5 amine-terminated dendrimer. Each time step is $2t_c$.

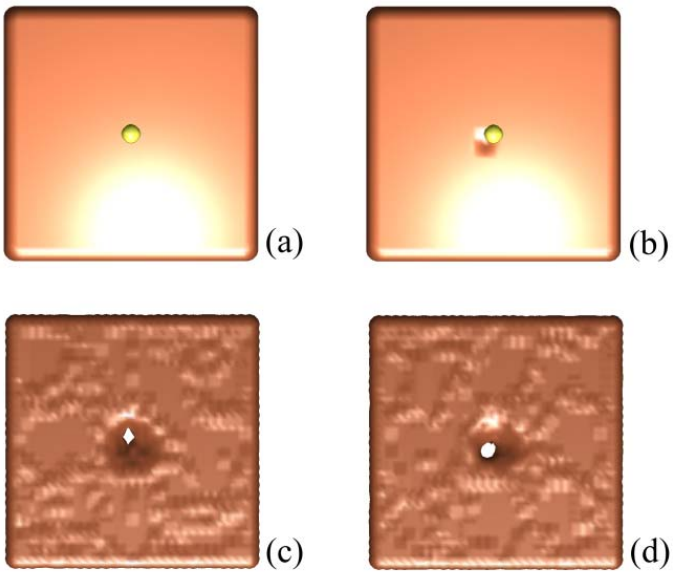

Figure 4.5 The effect of an existing bilayer defect. (a) and (b) are initial configurations. After $6t_c$, the generated hole from a pre-existing defect (d) is larger than the hole from a intact membrane (c).

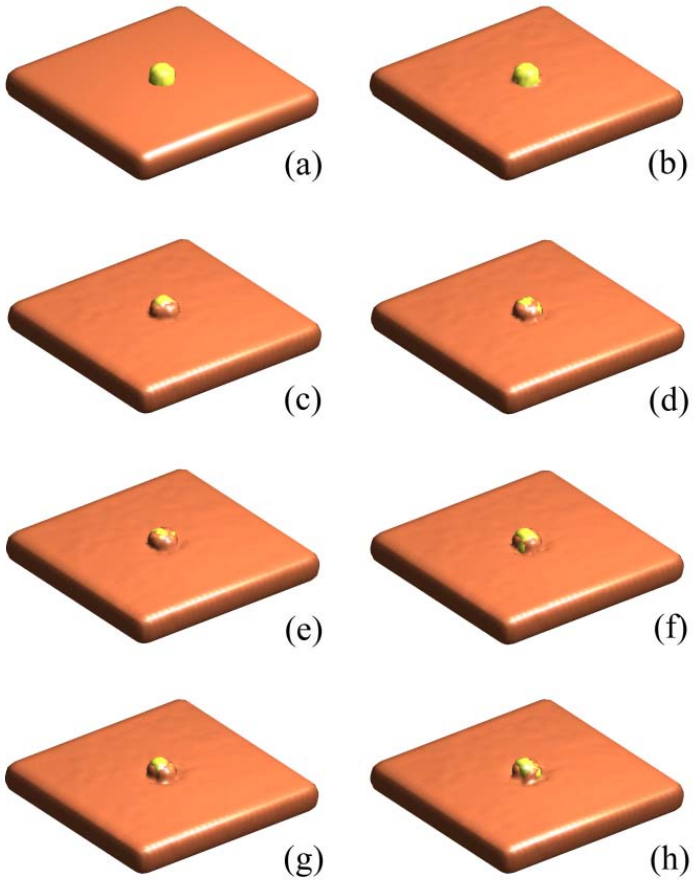

Figure 4.6 Evolution of the membrane with a G5 acetamide-terminated dendrimer. Each time step is $2t_c$.

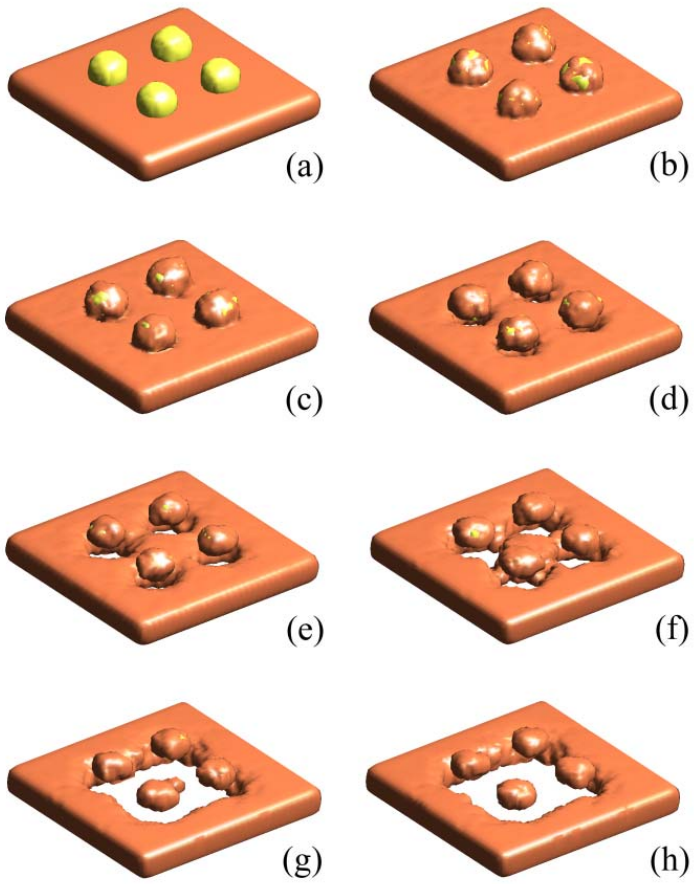

Figure 4.7 A larger hole formation from multiple dendrimers (each time step is $4t_c$). The generated hole is larger than a single dendrimer particle.

4.4 DENDRIMER INTERACTION CONCLUSIONS

This chapter has developed and implemented a phase field model for the interactions between a PAMAM dendrimer and a lipid bilayer. Simulations have shown that the G7-amine PAMAM dendrimer, which is positively charged, had caused the formation of a small hole in the membrane. The G7-acetamide PAMAM dendrimer, which is neutrally charged, similarly caused a hole formation but resulted in a smaller hole than that from G7-amine PAMAM dendrimer. Those conclusions agree well with experimental observations. Also, from the experiment, the size of the dendrimer is another important factor on the interactions. The simulation results showed that the lower generation dendrimer had a greatly reduced ability to remove lipid molecules from the surface. Furthermore, the simulation results demonstrated that a pre-existing defect on a lipid layer could be expanded by a dendrimer, which is also observed from the experiment. Finally, it is also demonstrated that multiple dendrimers form a larger hole which may not be induced by a single dendrimer. In summary, the simulation results agree with the results from experimental observations. Furthermore, it provides us with a mechanism for the formation of a hole. Consequently, the results may be useful in the design of nanoparticles for various biological and medicine applications.

CHAPTER 5

ELECTROWETTING OF A DROPLET PARTICLE ON A DIELECTRIC

Electrowetting originates from the observation of Lippmann [112], where the capillary depression of mercury in contact with electrolyte solutions could be varied by applying an electric field. However, there was an obstacle to broaden the application: electrolytic decomposition of water on high voltages. Recently, Berge [113] used a thin insulating layer to separate the conductive liquid from a metallic electrode in order to eliminate the problem of electrolysis. This approach is referred to as electrowetting on dielectric (EWOD). Electrowetting has been investigated by researchers using diverse approaches. Also experimental studies [114-117] have been conducted and have revealed saturation/instability of the contact angle when the applied voltage is raised above a

critical value. Welters *et al.* [118] and Sondag-Huethorst *et al.* [119] calculated effective interfacial tension, which was reduced by an applied voltage. Berge [113] performed a minimization of the free energy, in this case, the corresponding thermodynamic potentials are related by a Legendre transformation. In order to provide a picture including forces exerted on the droplet, Jones *et al.* [120, 121] and Zeng *et al.* [122] introduced the Maxwell stress tensor and obtained the net force acting on the droplet. Verheijen *et al.* [115] suggested the charge trapping is responsible for the saturation. Vallet *et al.* [114] and Mugele *et al.* [123] reported similar results that the contact line became unstable at high voltages, leading to the ejection of small droplets from the mother droplet with a characteristic lateral spacing. While the above models seem to capture the essential physics, there is still a need for a thorough understanding of the mechanism to maximize its potential. In this chapter, we present the results of computational simulations related to the instability phenomenon. A phase field model combining thermodynamics and hydrodynamics provides us with a useful tool for predicting the electrowetting phenomena from the various experimental environments. It enables us to extend our system to the complex droplet morphologies, patterned electrodes, and topographical surface patterns. Moreover, it provides the dynamic aspects of the electrowetting phenomenon, which is important for practical applications, while most of the theories and experiments were focused on static properties. Based on these advantages, we seek to elucidate why the instability occurs and how to suppress this obstacle.

5.1 MODELING

5.1.1 Phase field model

The phase field model is described by a set of field variables, which characterize the spatial distributions in different phases. The field variables are updated as the system evolves to reduce the free energy. The wetting phenomenon can be ascribed to the minimization of free energy in the system; the interfaces between the two immiscible matters are free to change their morphology to minimize the free energy. The phase interface is considered to be a region of finite width in which the phase field variable varies rapidly, but smoothly, from one phase value to another.

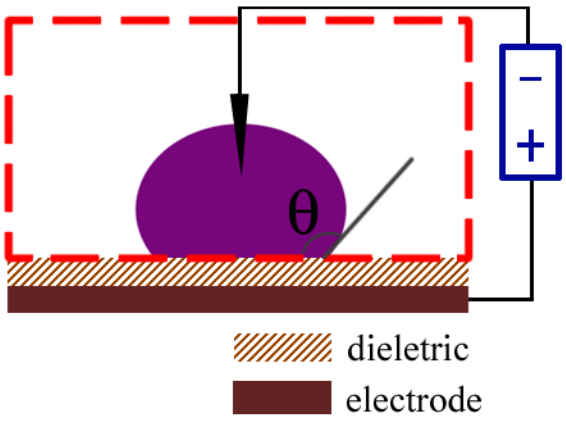

Figure 5.1 A schematic diagram for the system. The droplet is partially wetting on a dielectric layer and the field is generated by an electrode and an electro-rod. Here, the red dotted line represents the phase field model, and the dielectric layer is added for the calculation of electric field. Here, θ denotes the contact angle.

Figure 5.1 shows a droplet of partial wetting on a dielectric layer. In our phase field model, the 2-dimensional system is confined to the droplet and the medium because we ignore the evolution of the layer. We may define the concentration of each phase by its volume fraction. Treat the concentration of the droplet, $c(\mathbf{x},t)$, as a spatial continuous and time dependent function. Here, $\mathbf{x}$ is a position vector; note that $c(\mathbf{x},t)=1$ for the droplet and $c(\mathbf{x},t)=0$ for the medium. The total free energy of the system depends on phase configurations and electric field distributions, namely,

$$G=\int_{\Omega}\left(f(c)+\frac{1}{2}h(\nabla c)^2-\frac{1}{2}\varepsilon_0\varepsilon_r(c)\left|\nabla\phi\right|^2\right)dS+\int_{\partial\Omega}[\sigma_{SD}+(\sigma_{SM}-\sigma_{SD})\rho(c)]dl \quad (5.1)$$

The first three terms of energy functional approximate the total energy in the area of the system and the last integration represents the surface energy on the boundaries. The $f(c)$ term represents the chemical energy, which drives phase separation. We use a double-well function, $f(c)=f_0c^2(c-1)^2$, where f_0 is a positive constant. The function has two minima corresponding to the droplet and medium phases, respectively. The interface energy between the droplet and the medium can be established through a gradient term of c in the Eq. (5.1), where h is a material constant. The third term represents the electrostatic energy. Here, $\varepsilon_0=8.85\times10^{-12}$ F/m is the vacuum permittivity, ε_r is the dielectric constant of the material, and ϕ is the applied field. The dielectric constant may be interpolated using a transition function, $\rho(c)=1/2\left(1+\tanh(5-10c)\right)$, to make a rapid and smooth variation in the value, namely, $\varepsilon_r(c)=\varepsilon_r^{droplet}\left(1-\rho(c)\right)+\varepsilon_r^{medium}\rho(c)$. Note, $\rho(c_{droplet})=0$ and $\rho(c_{medium})=1$. The negative sign in the electrostatic energy is due to a constant applied voltage. The surface energy at the boundaries is also expressed using a

transition function. Here σ_{SD} and σ_{SM} represents the surface energy difference between the solid and the droplet, the solid and the medium, respectively. Consider a variation in G from the Eq. (5.1),

$$\delta G = \int_{\Omega}\left(f'(c)\delta c + h(\nabla c)\delta(\nabla c) - \frac{1}{2}\varepsilon_0\varepsilon_r'(c)\left|\nabla\phi\right|^2 \delta c \right) dS + \int_{\partial\Omega}(\sigma_{SM} - \sigma_{SL})\rho'(c)\delta c dl \quad (5.2)$$

The variation in G can be simplified by taking into account a boundary condition,

$$h\mathbf{n}\cdot\nabla c + (\sigma_{SM} - \sigma_{SL})\rho'(c) = 0 \quad (5.3)$$

The diffusion is the only mass transport mechanism which is given by $\mathbf{J} = -M\nabla\mu$, where M is the mobility and $\mathbf{J}$ is the flux. Viscous flow adds a convective term, $c\mathbf{v}$, to the flux, where $\mathbf{v}$ is the flow velocity. Here, we consider incompressible flow so that $\nabla\cdot\mathbf{v} = 0$. The chemical potential is defined by $\mu = \delta G / \delta c$, then, the variation in G can be expressed as $\delta G = \int_{\Omega}\mu\delta c dS$. Also, a variation in c combined with mass conservation relation gives, $\delta c = (\partial c/\partial t)\times dt = -dt\nabla\cdot\mathbf{J}$. Applying the divergence theorem results in,

$$\delta G = dt\int_{\Omega}\nabla\mu\cdot\mathbf{J}dS - dt\int_{\partial\Omega}(\mathbf{n}\cdot\mathbf{J})\mu dl \quad (5.4)$$

The boundary integral vanishes by taking, $\mathbf{n}\cdot\mathbf{J} = 0$ on $\partial\Omega$. From the above equations, we have a governing equation set,

$$\begin{aligned} &\left(\frac{\partial c}{\partial t} + (\mathbf{u}\cdot\nabla)c = \nabla(M\cdot\nabla\mu)\right)\Big|_{\Omega} \\ &\left(\mu = f'(c) - h\nabla^2 c - \frac{1}{2}\varepsilon_0\varepsilon_r'(c)\left|\nabla\phi\right|^2\right)\Big|_{\Omega} \\ &(\mathbf{n}\cdot\nabla\mu = 0)\Big|_{\partial\Omega}, (h\mathbf{n}\cdot\nabla c + (\sigma_{SM} - \sigma_{SL})\rho'(c) = 0)\Big|_{\partial\Omega} \end{aligned} \quad (5.5)$$

With the presence of a diffusive interface, the modified Navier-Stokes equation describes the viscous flow,

$$\rho\left(\frac{\partial \mathbf{v}}{\partial t}+\mathbf{v}\cdot\nabla\mathbf{v}\right)=-\nabla p+\nabla\cdot\left(\eta\nabla\mathbf{v}\right)+\mu\nabla c \tag{5.6}$$

Here, ρ is the density, η the viscosity, and p is the pressure that enforces the incompressibility constraint $\nabla\cdot\mathbf{v}=0$. The last term $\mu\nabla c$ accounts for the sum of all the given forces at the interface. Eq. (5.5) and (5.6) need to be solved simultaneously as well as the electric field to obtain evolution sequences of the system. The electric potential satisfies the Laplace equation,

$$\nabla\cdot\left(\varepsilon_r\nabla\phi\right)=0 \tag{5.7}$$

The geometry of the system for an electric field calculation is shown in Figure 5.1. We applied a constant potential at the droplet boundary and on the bottom electrode. For outer boundaries in the system, the Neumann boundary conditions were applied. We normalize Eq. (5.5), (5.6) and (5.7) with a characteristic velocity V_c, length L_c, and time $t_c=L_c/V_c$. Eq. (5.7) retains the same form after normalizing, and dropping the index of the normalization of Eq. (5.5) and Eq. (5.6) gives,

$$\begin{aligned}&\left(\frac{\partial c}{\partial t}+\mathbf{v}\cdot\nabla c=\frac{1}{\mathrm{Pe}}\nabla\cdot(\nabla\mu)\right)\Big|_{\Omega}\\&\left(\mu=f'(c)-\mathrm{Ch}^2\nabla^2 c-\frac{1}{2}\frac{\partial\varepsilon_r(c)}{\partial c}\left|\nabla\phi\right|^2\right)\Big|_{\Omega}\\&\left(\mathbf{n}\cdot\nabla\mu=0\right)\Big|_{\partial\Omega},\left(\mathbf{n}\cdot\nabla c+\beta\rho'(c)=0\right)\Big|_{\partial\Omega}\end{aligned} \tag{5.8}$$

$$-\nabla p+\nabla\cdot\left(\eta\nabla\mathbf{v}\right)+\frac{1}{\mathrm{Ca}}\mu\nabla c=0 \tag{5.9}$$

The mobility M and viscosity η are dimensionless numbers normalized by the mobility and viscosity of the droplet, M_0 and η_0. The potential field ϕ is normalized by $\phi_c=L_c\sqrt{f_o/\varepsilon_0}$. In Eq. (8), the Péclet number $\mathrm{Pe}=V_cL_c/\left(M_0f_0\right)$ reflects the ratio of the

diffusive time scale and the convective time scale. The significance of the interface energy is described by the Cahn number, represented by $\mathrm{Ch} = \sqrt{h / f_0} / L_c$. The Reynolds number, $\mathrm{Re} = \rho V_c L_c / \eta_0$, reflects the ratio of inertial and viscous forces. We consider a viscous fluid at moderate velocities, for example, a low Reynolds number. In Eq. (5.9), we ignore the inertia term, the left-hand side of Eq. (5.6). Thus, the velocity is instantaneously inferable from the concentration. The capillary number $\mathrm{Ca} = \eta_0 V_c /(L_c f_0)$ affects the relative magnitude of viscous force and interface force. The parameter $\beta = L_c \left(\sigma_{SM} - \sigma_{SL}\right) / h$ possesses the information about the surface energy differences, which determines the contact angle without an electric field.

5.1.2 Finite element method

The numerical approach needs to have high spatial resolution to resolve the high-order derivatives in the diffusion equation, as well as the large gradients at the interface. In this work, we combine the Galerkin finite element method for Eq. (5.8) and semi-implicit Fourier spectral method for Eq. (5.9). We follow the standard procedure for setting up the variational formulation, taking a weighted integral residual projection of the governing equation with the test function w, and through integrating by parts. Hence, our problem becomes one of finding a function of c such that

$$\left(\frac{\partial c}{\partial t}, w\right)_\Omega + \left(\mathbf{v}\cdot\nabla c, w\right)_\Omega + \left(\frac{1}{\mathrm{Pe}}\nabla\mu, \nabla w\right)_\Omega = 0 \tag{5.10}$$

$$\left(\mu, w\right)_\Omega = \left(4c^3 - 6c^2 + 2c, w\right)_\Omega + C_h^2\left(\nabla c, \nabla w\right)_\Omega - \frac{1}{2}\left(\Delta\varepsilon_r \left|\nabla\phi\right|^2, w\right)_\Omega + C_h^2\left(\beta\rho'(c), w\right)_{\partial\Omega} \tag{5.11}$$

where the usual inner product notation is used for the respective interior and boundary integrals. Now, we partition off Ω into a number of finite elements Ω_e, then solve the corresponding discrete system of the equations. A variable can be expressed by using the basis of the shape function ψ_j^e, for one example of the variable c in Ω_e,

$$c^e(\mathbf{x},t) = \sum_{j=1}^{N_e} c_j^e(t)\psi_j^e(\mathbf{x}) \tag{5.12}$$

where N_e is the number of nodes in Ω_e, and c_j^e is the value of c^e at node $\mathbf{x}_j^e$ of the element. The finite element approximation of Eq. (5.12) leads to a system of N ordinary differential equations in the N unknown functions $c_j(t)$ in the form,

$$\mathbf{A}_1 \frac{dc(t)}{dt} + \mathbf{A}_2 c(t) = \mathbf{a}(t), 0 \le t \le T \tag{5.13}$$

where $A_{1,ij} = \int_{\Omega_e} \psi_i \psi_j d\Omega$, $A_{2,ij} = \int_{\Omega_e} \psi_i \left(\mathbf{v}\cdot\nabla\psi_j\right) d\Omega$, and $a_i = -\int_{\Omega_e} \frac{1}{\mathrm{Pe}} \nabla\mu\cdot\nabla\psi_i d\Omega$. In order to solve Eq. (5.13), we first partition the time domain $0 \le t \le T$ into equal intervals of length Δt. At $t = 0$, the solution is known from the initial configuration. To advance the solution in time from $t = n\Delta t$ to $(n+1)\Delta t$, we use the forward finite difference approximation,

$$\frac{dc(n\Delta t)}{dt} \approx \frac{c^{n+1}(t) - c^n(t)}{\Delta t} \tag{5.14}$$

Then, Eq. (5.13) and (5.14) lead to the algorithm,

$$c^{n+1}(t) = \Delta t \cdot \mathbf{A}_1^{-1}\left[\mathbf{a}^n - \mathbf{A}_2 c^n(t)\right] + c^n(t) \tag{5.15}$$

where $\mathbf{a}^n = \mathbf{a}(n\Delta t)$. Similarly, using the basis of the hat functions, we can solve the corresponding discrete system of the Eq. (5.11) for the chemical potential. The finite

element approximation of Eq. (5.11) leads to a system of N ordinary differential equations in the N unknown functions $\mu_j(t)$ in the form

$$\mathbf{B}\mu(t) = \mathbf{b} \tag{5.16}$$

where $B_{ij} = \int_{\Omega_e} \psi_i \psi_j d\Omega$, $b_{i,1} = \int_{\Omega_h} \left(4c^3 - 6c^2 + 2c\right)\psi_i d\Omega$, $b_{i,2} = C_h^2 \beta \int_{\partial\Omega_h} \rho'(c)\psi_i d\Omega$, $b_{i,3} = C_h^2 \int_{\Omega_h} \nabla c \cdot \nabla \psi_i d\Omega$, $b_{i,4} = -\frac{1}{2}\Delta\varepsilon_r \int_{\Omega_h} |\nabla \phi|^2 \psi_i d\Omega$ and $b_i = b_{i,1} + b_{i,2} + b_{i,3} + b_{i,4}$. It is clear that the calculation of element stiffness matrices and load vectors for a curvilinear element Ω_e would be awkward if performed directly in terms of the global coordinates. Moreover, the character of such a calculation would change from element to element in the mesh. If we introduce an invertible transformation between a master element $\hat{\Omega}$ of simple shape and an arbitrary element Ω_e , it should be possible to transform the operations on Ω_e so that they hold on $\hat{\Omega}$. Then, we can perform the calculations conveniently on the master element. In this research, we use triangle elements. The shape function, $\hat{\psi}$, pertains to the master element, $\hat{\Omega}$. From the linear map, from arbitrary element Ω_e to master element, the shape functions are

$$\hat{\psi}_1 = 1 - \xi - \eta, \hat{\psi}_2 = \xi, \hat{\psi}_3 = \eta \tag{5.17}$$

where ξ , η are local coordinates on the master element. Thus, integrals of functions over element Ω_e can be evaluated using calculations on $\hat{\Omega}$ by simple relationship, for instance, $A_{ij} = \int_{\hat{\Omega}} \hat{\psi}_i \hat{\psi}_j \left|\mathbf{J}(\xi,\eta)\right| d\hat{\Omega}$. Here, the Jacobian $\left|\mathbf{J}(\xi,\eta)\right|$ represents the area ratio between two domains. The matrix computations were done with the preconditioned biconjugated-gradient method and the Jacobi pre-conditioner is adopted. The approach allows one to compute a large domain efficiently. We followed similar steps for the electric field

calculation with the finite element method. The velocity field is solved by Eq. (5.9) and the incompressibility condition. To treat the variable viscosity, we rewrite [124]

$$\nabla \cdot (\eta \nabla \mathbf{v}) = B\nabla^2 \mathbf{v} + \mathbf{r}(\mathbf{v}) \tag{5.18}$$

where $r(v) = \nabla \cdot (\eta \nabla \mathbf{v}) - B\nabla^2 \mathbf{v}$ and B is a constant. We take $B = \max(\eta)$ in the simulations, and achieve numerical stability in all situations. Taking the divergence on both sides of Eq. (5.7) and applying the incompressibility constraint $\nabla \cdot \mathbf{v} = 0$, we obtain the pressure at the nth time step

$$\nabla^2 p^n = \nabla r(\mathbf{v}^{n-1}) + \frac{1}{\mathrm{Ca}} \nabla \cdot (\mu^n \nabla c^n) \tag{5.19}$$

The velocity field is given by reorganizing Eq. (9), namely,

$$\nabla^2 \mathbf{v}^n = \frac{1}{B}\left(\nabla p^n - r(\mathbf{v}^{n-1}) - \frac{1}{\mathrm{Ca}} (\mu^n \nabla c^n) \right) \tag{5.20}$$

The equation (5.19) and (5.20) are solved to obtain the velocity. The following is the outline of the procedure to compute c^{n+1} from c^n. First, compute the electric field ϕ^n that corresponds to the concentration distribution c^n. Then substitute the solution of ϕ^n into the Eq. (5.11) to get μ^n. After solving the modified Navier-Stokes equation, it gives $\mathbf{v}^n$. Using this result, we compute the Cahn-Hilliard equation by Eq. (5.10) to obtain c^{n+1}.

5.1.3 Simulation parameters

Consider a water droplet as an example. The interface thickness, δ, in terms of the model parameters, can be obtained as, $\delta \sim \sqrt{h/W}$ [105]. Here, W represents the height of the barrier between wells in the free energy density, f. In our model, the value of W is $f_0/16$. Then the surface energy can be obtained from a simplified interface profile. If we assume a flat interface, the phase field variable $c(\mathbf{x},t)$ can be expressed as a function of $c = 1/2\tanh(4x/\delta)$. Then, the surface energy, σ_{DM}, can be calculated from,

$$\sigma_{DM} = \int_{-\infty}^{\infty} h\left(\frac{\partial c}{\partial x}\right)^2 dx \sim \frac{1.33333h}{\delta} = \frac{1}{3}\sqrt{hf_0} \tag{5.21}$$

We choose the characteristic length $L_c = 10\sqrt{h/f_0}$, which is around $10nm$ and it gives $C_h = 0.1$. The surface energy of a water droplet in the air is $70\times10^{-3}(J/m^2)$. From the relationship, we have $f_0 = 2.1\times10^8$ and $h = 2.1\times10^{-10}$. The capillary number, Ca, for a water droplet is about 10^{-3} [125]. The mobility M_0 is related to the diffusion coefficient, $D = 2M_o f_0$, which is approximately $0.2272(0.1nm^2\cdot ps^{-1})$. The viscosity of water in room temperature is $10^{-3}(Pa\cdot s)$. These values give $\mathrm{Pe} \sim 18$. From the Young's equation,

$$\cos\theta_c = \frac{\sigma_{SM} - \sigma_{SD}}{\sigma_{DM}} = \frac{3}{10}\beta \tag{5.22}$$

we estimate the range of β, which is approximately $|\beta| \le 3.3$.

5.2 SIMULATION RESULTS

5.2.1 Dynamic aspect

All the simulations are performed on a domain of 56×32 with an L_c length unit scale. We used 7163 isosceles triangular elements with the length of $0.25L_c$ and $0.17L_c$. The initial configuration of a droplet is a sphere with radius $8L_c$, which touches the solid surface. First, we predict the final contact angle without an electric field. Depending on the surface energy difference, the contact angle varies as demonstrated in Equation (5.23). Figure 5.2 shows the final configurations depending on β. A larger β, which represents a hydrophilic surface, shows a wettable surface, and a smaller β, which represents a hydrophobic surface, shows a non-wettable surface. The final contact angles are well-matched with Equation (5.22), as can be seen in Figure 5.2.

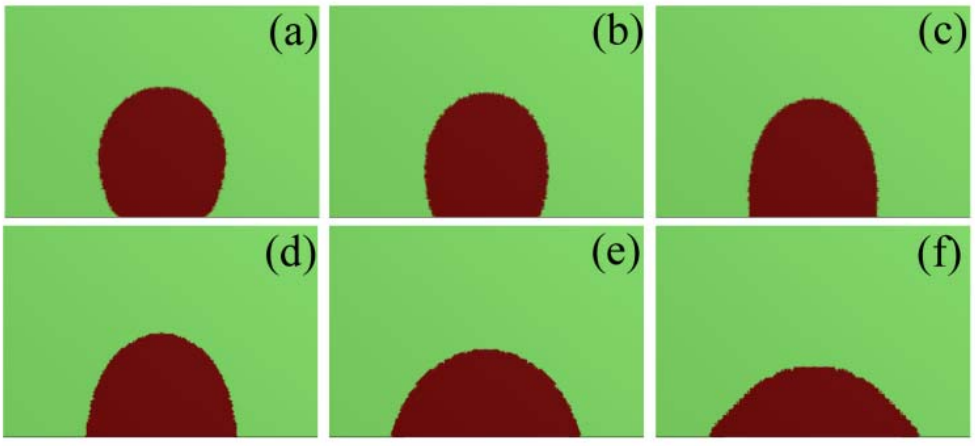

Figure 5.2 Critical angles for different βs without an electric field (a: $\beta=-2.5$, b: $\beta=-1.5$, c: $\beta=-0.5$, d: $\beta=0.5$, e: $\beta=1.5$, f: $\beta=2.5$)

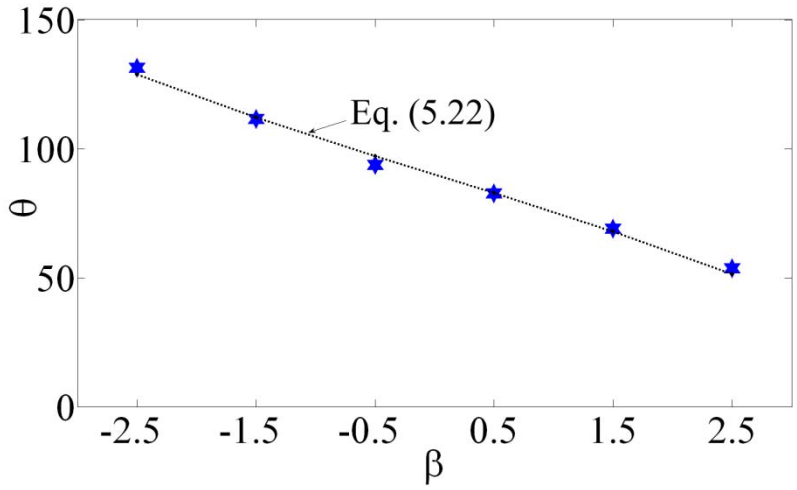

Figure 5.3 Comparison of the contact angle. The blue star marks represent the computational results and the dotted line represents the contact angle from Young's equation, Eq. (5.22).

The Equation (5.22) provides just static properties, whereas dynamic responses of the droplet are important for many practical applications. In addition, Equation (5.22) does not include the size of the droplet, which means the contact angle is independent on the size. A theoretical model [126] was developed to predict the effect of droplet size on contact angle for droplets on surfaces. The model takes into account the fact that the effect of gravity diminishes as the size of the droplet decreases, therefore, for small droplets, gravity becomes negligible and the droplet contact angle becomes more dependent on surface wettability than on gravity. Thus, the asymptotic contact angle depends only on material properties. However, the response time to the applied field may depend on the volume size. Figure 5.4 shows the variation of the contact angles of three droplets with the same material property in different sizes. The angle of smaller droplets becomes reduced more quickly than those of larger droplets. This may be due to the

difference in time for the molecules of the droplet to relocate by the diffusion and the convection.

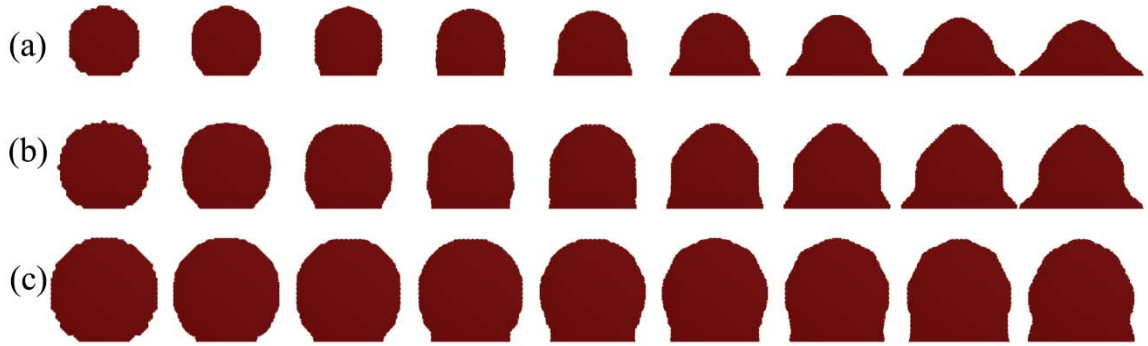

Figure 5.4 Time evolutions of three different size droplets under an electric field $\phi = 0.04$, $\beta = -2.5$, with each time step $100t_c$ (a) $r = 8L_c$ (b) $r = 10L_c$ (c) $r = 12L_c$

Now, we apply an electric field. The initial configuration is obtained from the result without an electric field. We increase the electric field from 0.01 to 0.04, with an increment of 0.01, and $\beta = -2.5$ for all cases. Note that as the electric field increases the velocity is also increased, and as a result, Ca and Pe vary. A relationship $v \propto \phi^2$, which is qualitatively well-matched with an experimental result [127], is used for the variation of the two parameters, Ca and Pe. Figure 5.5 shows the dynamic contact angles for each different applied field. The tendency is similar to the results from a molecular modeling simulation [128]. Above the critical angle in Young's equation, the net force, $\sigma_{SM} - \sigma_{SD}$, in the horizontal direction is larger than the horizontal component of the σ_{SM}, as a result, the time variation in the contact angle is larger than that around the critical angle.

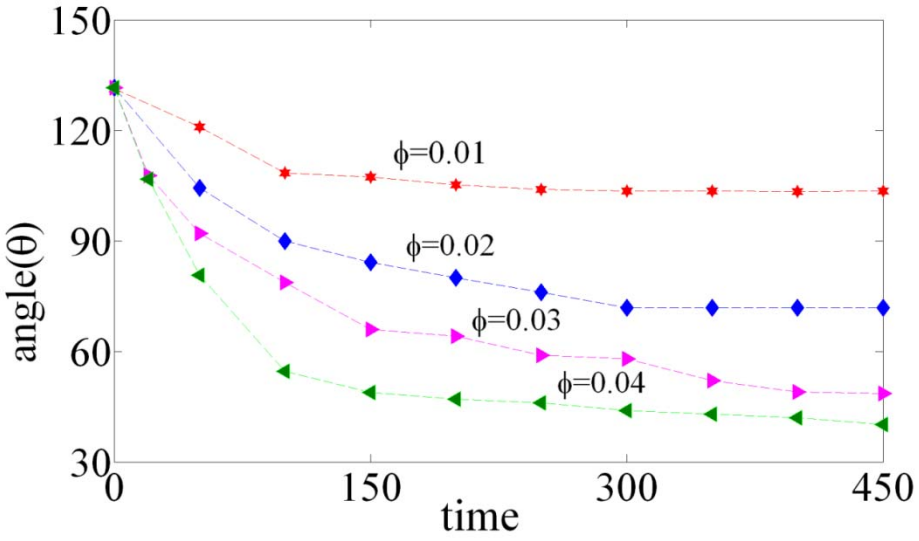

Figure 5.5 The dynamic contact angles for each voltage, where in all cases $\beta = -2.5$. The contact angles are decreased quickly, then slowly reach their final angles.

The lab-on-a-chip device performs entire analyses on a chip. For this purpose, it requires many steps of manipulation of the liquid sample. In many cases, it relies on pumping and pipetting, which need a large mechanical apparatus. Electrowetting is one solution for this problem. The principal idea for using electrowetting in the lab-on-a-chip is to provide a substrate with a series of individually addressable electrodes that allow for moving droplets around along the paths. Undoubtedly, diverse surface patterns of the electrodes and droplets may give rise to new opportunities in order to extend its application. Figure 5.6 shows one example of the partial wetting with an activated electrode (right side in red) and a deactivated electrode (left side in blue).

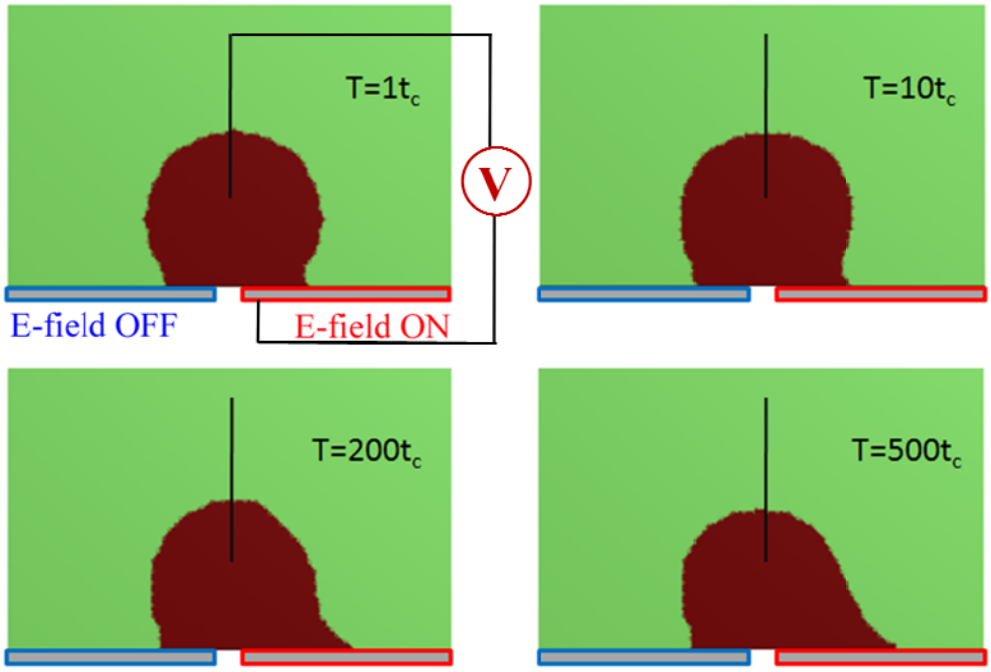

Figure 5.6 Partial wetting with an activated right electrode (red) and left deactivated electrode (blue)

5 2.2 Instability of electrowetting

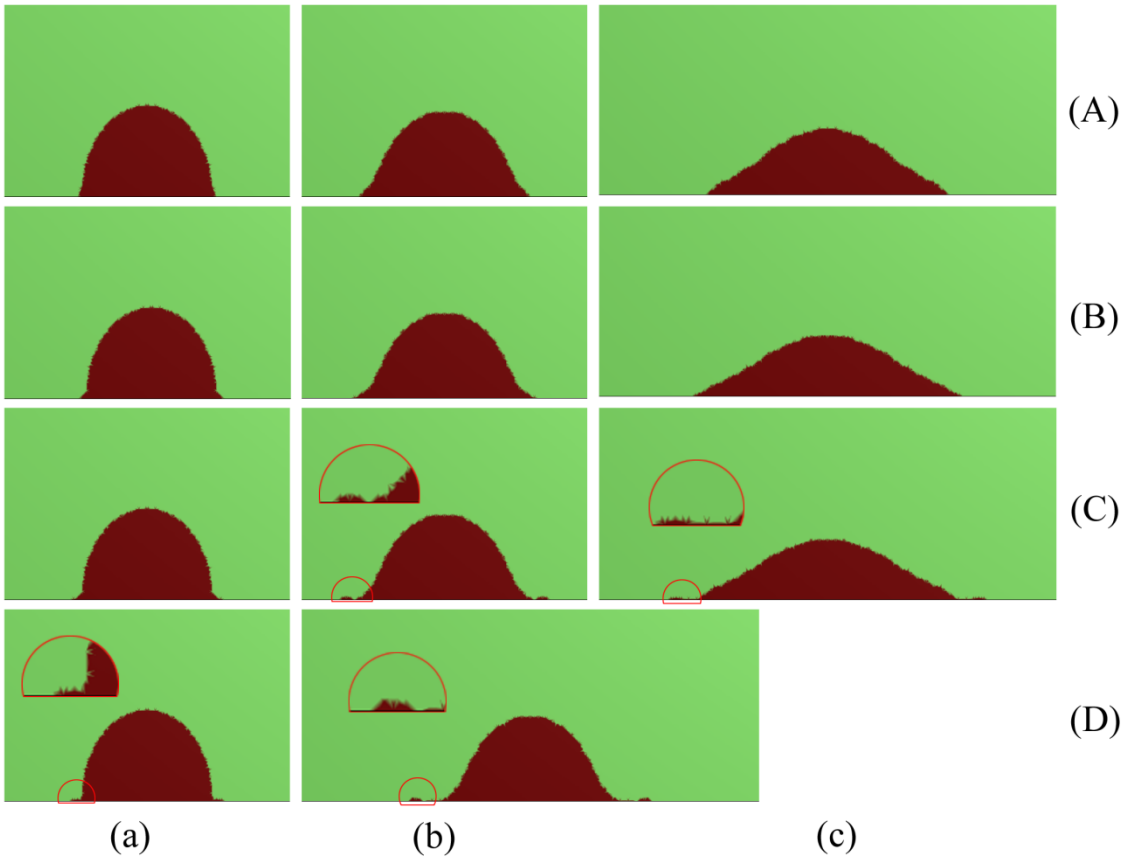

Figure 5.7 Droplet evolutions with different applied voltages (A: $\phi = 0.03$, B: $\phi = 0.04$, C: $\phi = 0.05$, D: $\phi = 0.06$, a: $t = 20$, b: $t = 200$, c: $t = 600$, unit: t_c, and $\beta = 0.5$)

Figure 5.7 shows representative results at selected time intervals from the computational experiments of increasing the voltage. As can be seen in the figure, the droplet becomes more wetted with increased voltage, which means the contact angle is reduced. This is a well-known phenomenon, referred to as EWOD (ElectroWetting On a Dielectric). However, in Figure 5.7(C), with a relatively high potential $\phi = 0.05$, ripples of the droplet occur on the solid surface at time $t = 200t_c$ (Figure 5.7 (c)). This instability

is similar to the experimental result; the contact line becomes unstable at high voltages which lead to the ejection of small droplets from the edge of the big droplet, with a characteristic lateral spacing. In Figure 4.7(D), when the external field is increased further, the instability starts more quickly at time $t = 20t_c$.

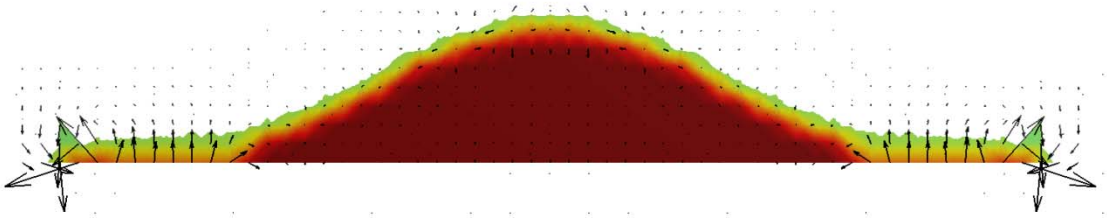

(a)

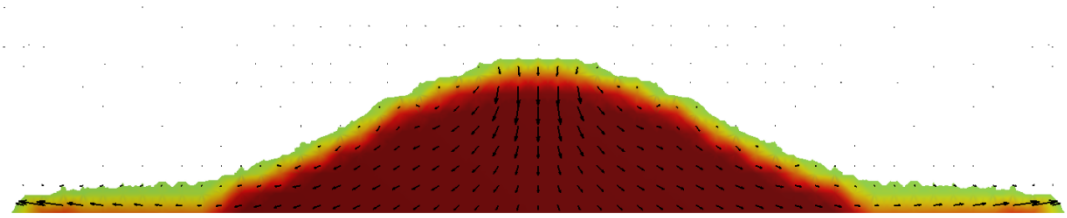

(b)

Figure 5.8 (a) Diffusion flow (b) Convection flow at one moment of an instability. The driving forces at the end of tail are very complicated.

The gradient of the chemical potential, $\mu = f'(c) - h\nabla^2 c - 1/2\varepsilon_0\varepsilon_r'(c)\left|\nabla\phi\right|^2$, represents the driving force for the diffusion process. An electromechanical approach [129], where a total force exerted on the droplet was calculated using the Maxwell stress tensor, cannot predict an instability phenomenon. However, the localized driving forces, as can be seen in Figure 5.8(a), show a physical picture. The force at the tail is strong compared to other regions, and it causes alternating compression/tension and

pressing/releasing which breaks the contact line and leads to the instability. This picture demonstrates that the surface tension, beyond a certain critical voltage, cannot resist a strong electrostatic force, and as a result, the emission of small droplets occurs. Figure 5.8(b) shows the convection flow at the same time with Figure 5.8(a). A thin liquid bridge is connecting the departing droplet with the mother droplet.

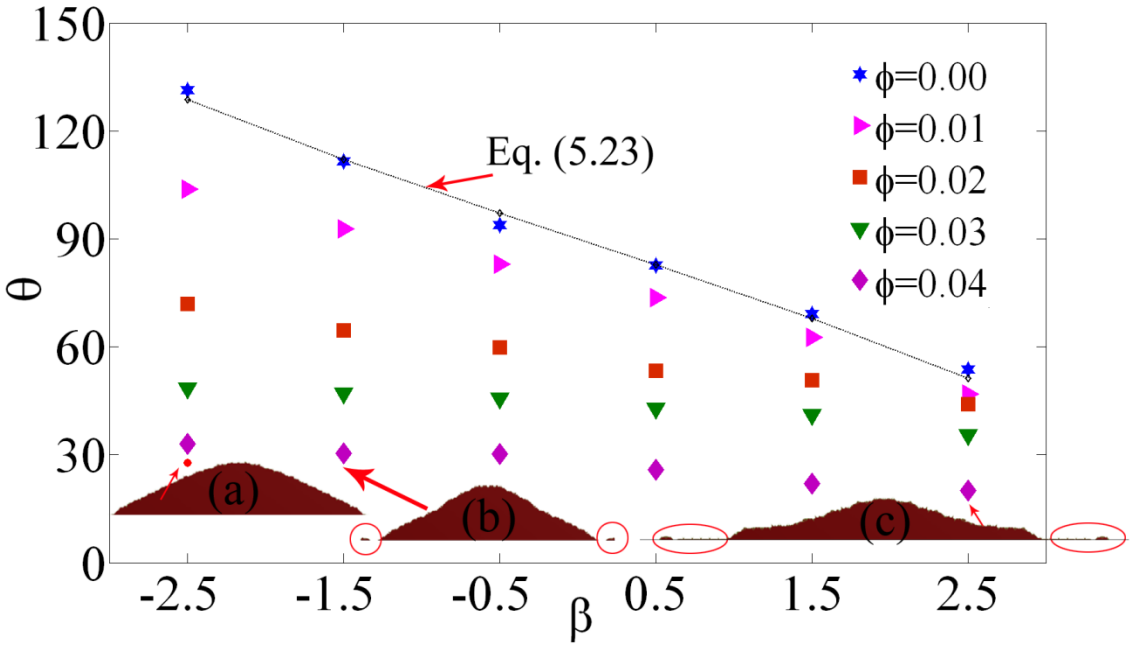

Figure 5.9 Results of a parametric study. It shows the final contact angles for different β and ϕ.

In order to verify that the instability of electrowetting is related to some other physical parameter more than the strength of the applied electric field, we conduct a parametric study. We select β as the independent variable because it is a function of the surface energies of the droplet, the solid, and the medium. By varying the value of β, different materials, including hydrophobic ($\beta<0$) and hydrophilic ($\beta>0$) surfaces, can

be involved in the simulations. The value of β is changed from -2.5 to 2.5 with an increment of 1. For each value of β, the electric field is applied from 0.01 to 0.05, with an increment of 0.01. Fig. 5.9 shows contact angle variations with β and ϕ. In all situations, the contact angle is decreased with the strength of the field which is similar to Figure 5.7. The incrementation of the angle is almost quadratic in relation to the applied voltage. This is consistent with the relationship from the effective interfacial energy method [119],

$$\cos\theta = \cos\theta_Y + \frac{\varepsilon_0 \varepsilon_d V^2}{2d\sigma_{LM}} \tag{5.23}$$

where θ_Y is the Young's equilibrium contact angle from Eq. (5.23), ε_0 and ε_d is the permittivities for vacumm and dielectric, respectively, d is the thickness of the dielectric layer, and V is the applied voltage.

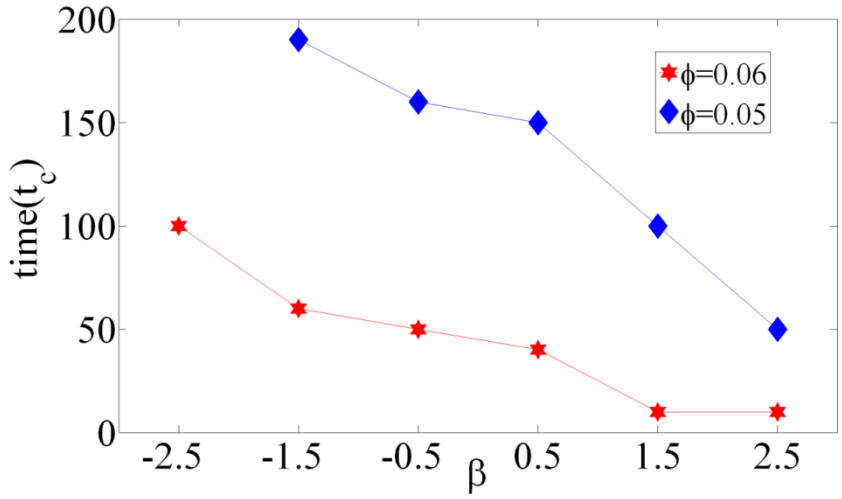

Figure 5.10 Starting time of an instability. Note that there is no instability for $\beta = -2.5$ case when $\phi = 0.05$ is applied.

The strength of the field where the instablity occurs is increased for a smaller β. The droplet ($\beta = -2.5$) in Figure 5.9 (a) is at $\phi = 0.05$, which has a stable contact angle. However, the two representive droplets (b: $\beta = -1.5$, c: $\beta = 2.5$) in the figure show the occurrence of the instability at $\phi = 0.05$. The other droplets ($\beta = -0.5, 0.5, 1.5$) also show instabilities; this behavior provides us with a clue for understading experimental observations [114]. It was observed that the droplet ejection is suppressed when salt is added to the water droplet. It has long been known that adding salt to water generally increases the surface energy of the solution. The ion-dipole bond formed between the water molecule and ions is stronger than the hydrogen bond formed between the water molecules. The additional energy needed to break the stronger bond raises the surface energy. As a result, a decreased β increases the field strength for the instablity. Figure 5.9 also indicates that the angle at the beginning of instable motion is smaller for a larger β. It means that hydrophilic materials can be more wettable without any instability.

Figure 5.10 represents the time it took to reach the set point of the instability after applying an electric field. Note that there is no instability for $\beta = -2.5$ case when $\phi = 0.05$ is applied. An instability begins more quickly for large values of β, and ϕ. We perform one more computational experiment to verify the previous discussion. From Figure 5.9, in all cases for $\beta > -2.5$, the instability occurs at $\phi = 0.05$ and the droplet is stable at $\phi = 0.04$, so we apply $\phi = 0.045$. As we can expect from the discussion, in the case of a smaller $\beta = -1.5$, the droplet is still stable (Figure 5.11(a)). However, in the case of $\beta = 1.5$, the droplet becomes unstable (Figure 5.11(b)).

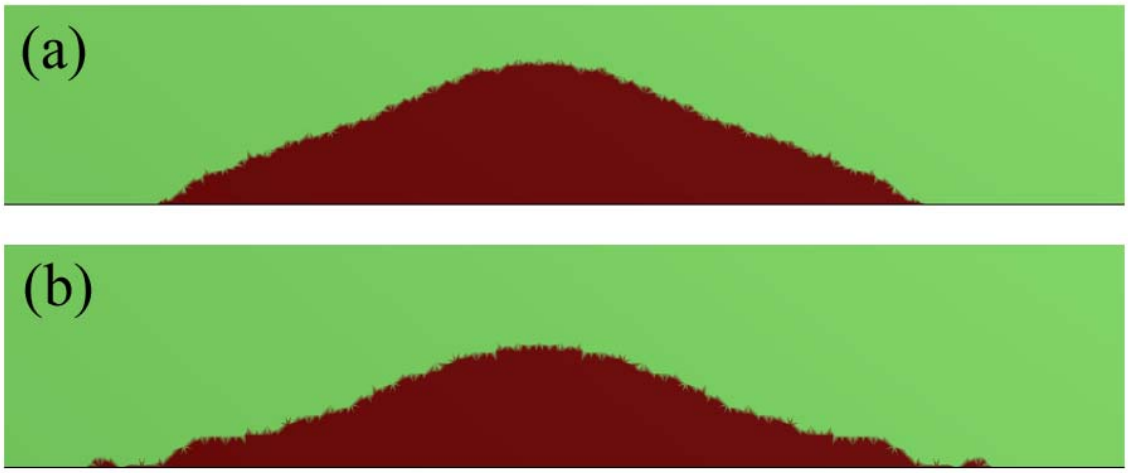

Figure 5.11 Droplet evolutions with different β parameters (a) $\beta = -1.5$, (b) $\beta = 1.5$ with an applied field $\phi = 0.045$.

5.3 STABILITY ANALYSIS

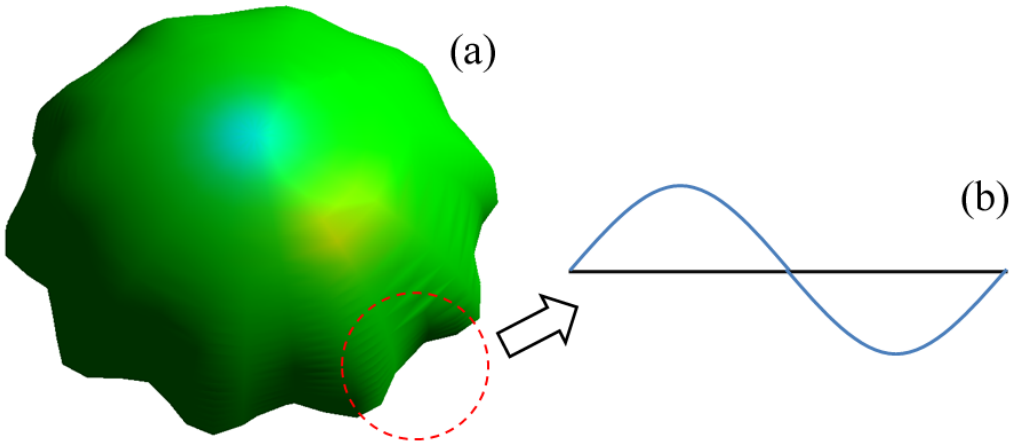

Figure 5.12 a) the schematic diagram of a perturbed droplet, b) one segment of the deformation

In order to verify the result of the parametric study, we conducted an instability analysis by considering a variation of the free energy after imposing a perturbation of small amplitude on the contact line between the solid, the medium and the droplet. The perturbed contact line has a larger length than the flat line, so the surface energy increases with the perturbation. Also an increment of perimeter length of the droplet results in an increment of electric capacitance, so the electrostatic energy decreases even under a constant applied potential. According to thermodynamic law, the surface energy favors the flat surface, but the electric field favors the perturbed line. From the net change in the free energy, we can investigate the stability of the system in equilibrium.

Figure 5.12 (a) shows a schematic droplet shape after perturbation. We slightly perturbed the contact line by $\eta = A\cos(kx)$, where A and k are the amplitude and the wavenumber of the perturbation. The wavenumber relates to the wavelength λ by $k = 2\pi / \lambda$. Here, we assumed the perturbation dies exponentially with the distance to the edge[130]. For the contribution from the surface energy between the droplet and the medium depends on the contact angle θ_G. The surface energy per unit length of the line is [131]

$$\Delta G_{sur} = \sigma_{DM} \frac{kA^2}{4} \sin^2 \theta_G \tag{5.24}$$

The increased length of the perturbed wetting line per unit length on the solid surface is calculated by

$$\Delta L = \frac{1}{\lambda}\int_0^{\lambda} \sqrt{1+\left[-Ak\sin(kx)\right]^2}\,dx - 1 \approx \frac{1}{\lambda}\int_0^{\lambda} 1 + \frac{1}{2}\left[-Ak\sin(kx)\right]^2 dx - 1 = \frac{k^2A^2}{4} \tag{5.25}$$

The change of the perimeter length of the droplet induces the variation of the electric capacitance C [114], as a result, the electrostatic field contribution to the energy can be calculated from $E_{elec} = -1/2CV^2$,

$$\Delta E_{elec} = -\frac{\varepsilon_r \varepsilon_0}{2}\left(\frac{1}{\pi - \theta_G}\ln\left(\sqrt{S}/d\right) + p(\theta_G)\right)e^{-k\xi}\phi^2\left(\frac{k^2A^2}{4}\right) \tag{5.26}$$

where ξ is a screening length, S is the surface area of the droplet facing the solid, d is thickness of dielectric layer, and $p(\theta_G)$ is a smooth function. Note that the electric charge distribution close to the line is modified. The roughening of the contour line leads to an electrostatic screening which tends to cancel the effect of its increased length [114]. The net change in the free energy is the sum of each contribution of Eq. (5.24) and (5.25), after normalizing,

$$\frac{\Delta G}{\left[\frac{(\sigma_{SM} - \sigma_{SL})A^2}{L_c}\right]} = \frac{5\pi}{\beta}\left(\frac{L_c}{\lambda}\right)\sin^2\theta - \frac{50\pi^2\varepsilon_r}{\beta}\left(\frac{1}{\pi - \theta_G}\ln\frac{\sqrt{S}}{d} + p(\theta_G)\right)\left[\left(\frac{L_c}{\lambda}\right)^2\right]e^{-\frac{L_c}{\lambda}\frac{2\pi\xi}{L_c}}\phi^2 \tag{5.27}$$

The contact angle, in Eq. (5.23), which is from the effective interfacial energy can be re-expressed in normalized parameters,

$$\cos\theta_E = \frac{3}{10}\beta + 15\varepsilon_r\frac{L_c}{d}\phi^2 \tag{5.28}$$

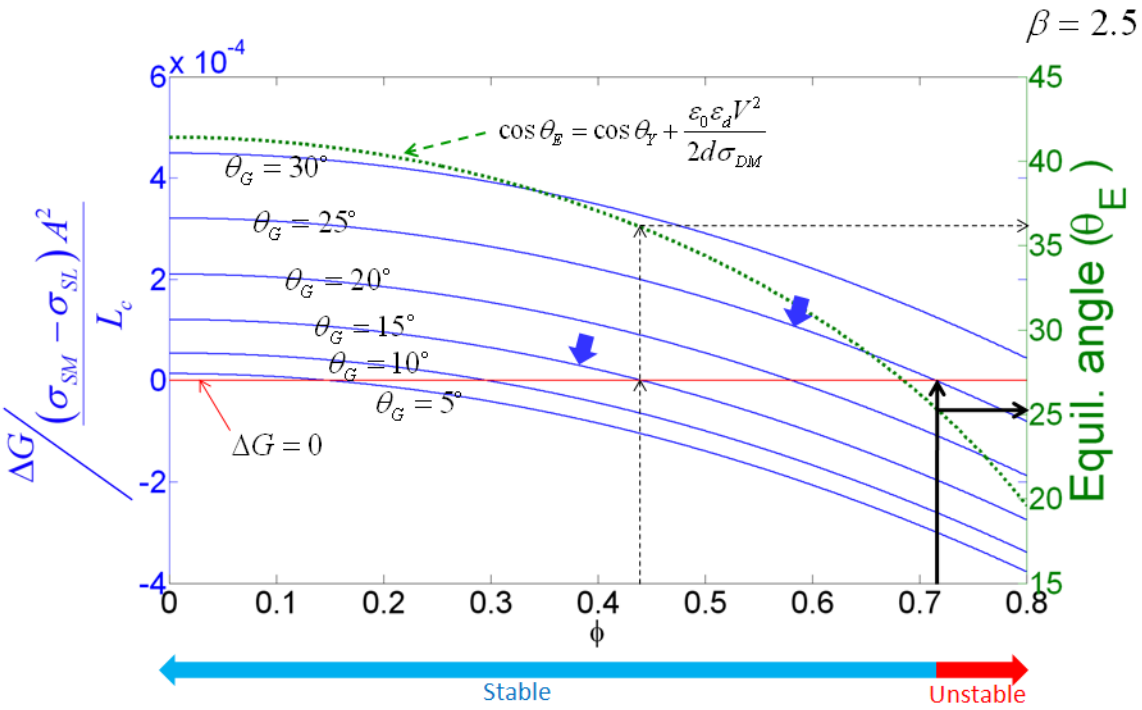

Figure 5.13 A stability analysis for $\beta = 2.5$. The black lines represent ΔG (the left ordinate) and the green dotted line represents the contact angle (the right ordinate).

Figure 5.13 plots the net change in the free energy, ΔG, as a function of the applied voltage and the angle between the contact lines. Relevant parameters are approximated from experimental data [114] ($\xi = 20\mu m$, $\lambda = 35\mu m$, $d = 50\mu m$). In Figure 5.13, where $\beta = 2.5$, the black lines represent ΔG for each specific angle. For each angle, if ΔG is negative, then the system becomes unstable. However, the final contact line follows the green dotted line which is from Eq. (5.28). In order to check the stability of the droplet, we need to compare both angles. For instance, when $\theta_G \le 15^\circ$, the system becomes unstable around $\phi = 0.43$. However, the contact angle at this voltage is over $\theta = 35^\circ$, as a result, the system is stable. For the $\theta = 25^\circ$ line, the system unstable at

around $\phi = 0.7$, where the final contact angle is also around $\theta = 25^{\circ}$. Consequently, the instability may occur at around $\phi = 0.7$. Similarly, when $\beta = 0.5$ as can be seen in Figure 5.14, the droplet may begin the instability at $\phi = 1.2$. It means that the instability can be suppressed by decreasing β. This is consistent with the result of the parametric study in Figure 5.9. It also demonstrates the experimental results [114]; the droplet ejection was suppressed, or at least, the threshold voltage increased substantially when salt was added.

In addition, the contact angle, when an instability begins, becomes smaller with increased β. This is matched with the results of the parametric studies.

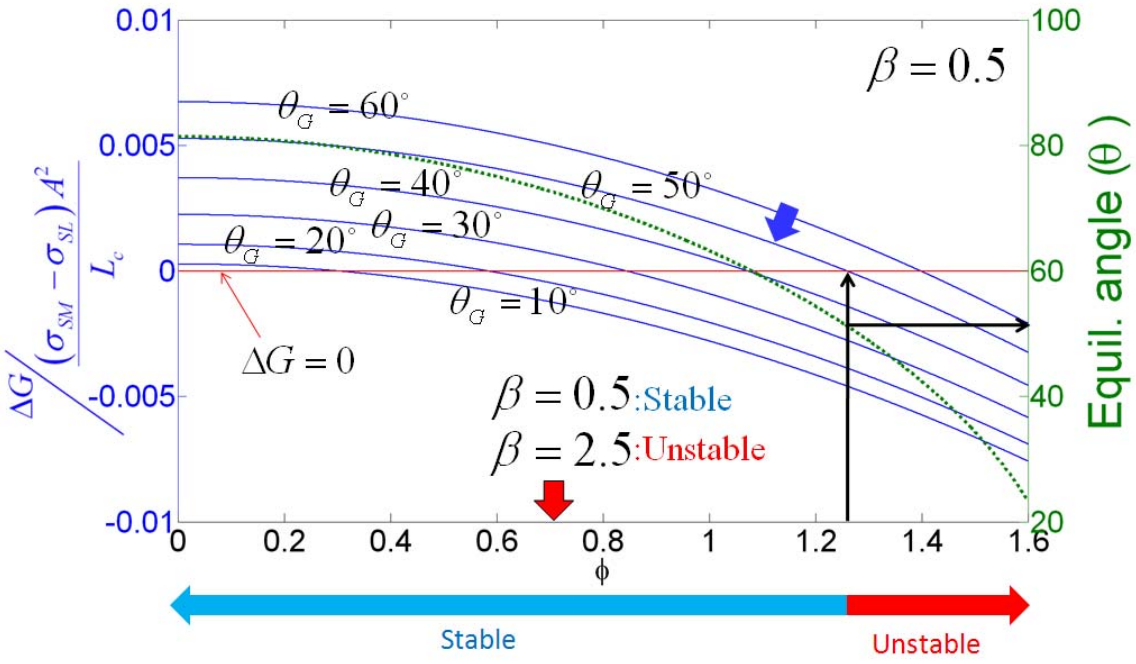

Figure 5.14 A stability analysis for $\beta = 0.5$. The black lines represent ΔG (the left ordinate) and the green dotted line represents the contact angle (the right ordinate).

5.4 ELECTROWETTING CONCLUSIONS

In summary, the computational approach provides useful information on the electrowetting phenomenon, such as dynamic responses and complex geometry. Furthermore, it shows the essential feature of the instability of electrowetting on a dielectric. Beyond a certain critical voltage, the surface tension cannot resist the strong electrostatic forces, therefore, the contact line becomes unstable. The onset of the emission of a small droplet is also related to the surface energies between the three phases. From the results of the analyses, we find that the instability can be suppressed by changing parameters, such as the surface energy of the droplet. This result may be a useful guide for designing novel devices, where the instability will be an obstacle to extend one's applications.

CHAPTER 6

CONCLUDING REMARKS

This thesis studies the interaction and the self-assembly of nanoparticles. Nanoparticle research is currently an area of intense research of nanotechnology due to a wide variety of potential applications in optical, biomedical, and electronic fields. The purpose of this dissertation is to investigate the use of nanoparticles as a means of self-assembly into new functional nanostructures and to elucidate the interactions of nanoparticles with structures at a nano/micro scale in nanodevices and biomedical system.

In many applications nanoparticles are functionalized with a thin layer of coating, which forms a core-shell structure. A coating prevents agglomeration with each other and provides a possibility of fabrication of new nanocomposite materials combining the unique properties of the core and shell. When these core-shell nanoparticles are dispersed

in a fluid, the functional properties of the colloidal suspension can be tuned by controlling the orientation of the particles with an applied electric field. In this research, we achieve the following; 1) We obtained an analytical form of the electric field for a core-shell particle and rigorously calculated the torque induced by an electric field. 2) We developed a dynamic model for the processing of core-shell nanoparticles dispersed in a fluid. The above developments lead to the following findings; 1) The shell of a nanoparticle has an important effect on the rotational behavior, even when it is thin and takes only a small portion of the total volume. 2) For lossy dielectrics, the permittivities and conductivities of both the shell and core of a particle determine the magnitude and direction of the induced torque. The core-shell structure was found to lead to frequency dependent behavior that is quite different from that of bare nanoparticles. 3) A competition, between the rotational alignment due to electric field and randomization due to Brownian rotation, reveals the evolution of the orientation distribution function (ODF) of many Brownian core-shell nanoparticles suspended in a fluid.

We developed a computational model that predict self-assembly of binary nanoparticles in an electric field, without explicitly considering the solvent particles. The solvent influences the behavior of the nanoparticles through random collisions and through imposing a frictional drag force on the motion of the nanoparticles. From the simulations, 1) We elucidate how parameters including permittivity, volume fraction, particle size, and the frequency of the field can be utilized to control the morphology of the superlattice structures. 2) The study explores rich patterning dynamics and a wide range of superlattices from functional gradient columns to an alternating chain-network. 3) The ability to pattern nanoparticles into a target structure will provide a critical insight to

design for a new functional material. Recent experiments demonstrated the potential of new functional materials, which is similar to the structures we demonstrated. However, one significant feature of the structures observed from our simulations is a mixture of binary particles. These are first non-experimental observations and are not attainable from monodispersed particles.

Poly (amidoamine) dendrimer nanoparticles have been used extensively in diverse areas of biology and medicine, such as gene and drug delivery, to disrupt cell membranes and allow the transport of material into cells. The size and surface chemistry of the nanoparticle have a strong influence on the interaction between a dendrimer and a membrane. We proposed a three-dimensional phase field model to account for this interaction. Attention is focused on the hole-formation process on the membrane. The simulations lead to several findings. 1) An amine-terminated G7 dendrimer, which has positive charges on the surface, causes the formation of a hole in the membrane. The removed molecules of the membrane encircle the dendrimer and form a dendrimer-filled membrane vesicle. 2) This effect is significantly reduced for a smaller dendrimer. 3) An acetamide-terminated dendrimer, which has a neutral charge at the surface, does not cause holes effectively. These results are consistent with experimental observations from AFM. Furthermore, the simulations show the whole process for generation of a hole, where the interface energy and elastic energy play an important role in that process. This makes the fundamental mechanism clear for the formation of a hole in the membrane. In addition, this may provide a critical insight to the designing of nanoparticles for various biological and medicine applications.

Electrowetting, which means that the wettability of a structured surface can be controlled by applying an electric field, has become an especially successful mechanism to control the surface morphology of small structures. It has a variety of applications such as 'lap-on-chip', electrowetting display, and optical system. In this thesis, we have developed a three-dimensional phase field model combining thermodynamics and hydrodynamics. The model leads to the following achievements. 1) This model is capable of predicting the dynamic responses of electrowetting, which may not be obtained from the conventional thermodynamic equations, but it is very important for designing practical devices. 2) It enables us to extend the system to complex droplet morphologies and patterned electrodes. 3) The simulation predicts the instability phenomenon of electrowetting, which was observed from experiments. The simulations reveal that the driving force for the diffusion around the edge of the droplet is strong and alternating compression and tension, breaks the contact line and leads to the instability. 4) A parametric study combined with a stability analysis shows that the instability is also related to surface energy. This observation explains suppression of the instability by changing the surface energy. The presented results may provide a useful guide for controlling this phenomenon.

BIBLIOGRAPHY

[1] P. J. Herrero, J. A. v. Dam, and L. P. Kouwenhoven, Nature **439**, 953 (2006).

[2] K. K. Likharev, IBM J. Res. Dev. **32**, 144 (1988).

[3] M. R. Singh, and A. E. Botha, Physica Status Solidi (B) **222**, 569 (2000).

[4] D. Li *et al.*, J. Appl. Phys. **85**, 5285 (1999).

[5] T. M. Parker, L. K. Wison, and N. G. Condon, Phys. Rev. B **56**, 6458 (1997).

[6] W. Shenton *et al.*, Nature **389**, 585 (1997).

[7] K. W. Guarini, C. T. Black, and S. H. Yeung, Adv. Mater. **14**, 1290 (2002).

[8] P. R. L. Malenfant *et al.*, Nature nanotechnology **2**, 43 (2007).

[9] F. X. Redl *et al.*, Nature **423**, 968 (2003).

[10] J. P. Behr, Chimia **51**, 34 (1997).

[11] E. Tomlinson, and A. P. Rolland, J. Controlled Release **39**, 357 (1996).

[12] A. DeHon, IEEE Transactions on Nanotechnology **2**, 23 (2003).

[13] Gratzel, Nature **414**, 338 (2001).

[14] S. C. Jakeway, A. J. d. Mello, and E. L. Russel, J. Anal. Chem **366**, 525 (2000).

[15] J. W. Hong, and S. R. Quake, Nat. Biotechnol. **21**, 1179 (2003).

[16] F. Hussain *et al.*, J. Composite Mater. **40**, 1511 (2006).

[17] M. VI *et al.*, Appl. Phys. Lett **80**, 4816 (2002).

[18] Z. Cheng, P. M. Chaikin, and T. G. Mason, Phys. Rev. Lett. **89**, 108303 (2002).

[19] S. S. P, *Colloid Electro-optics: Theory, Techniques, Applications* (Academic, London, 1991).

[20] F. DL *et al.*, Appl. Phys. Lett **89**, 223115 (2006).

[21] J. Gimsa, Bioelectrochemistry **54**, 23 (2001).

[22] W. Wen *et al.*, Nature materials **2**, 727 (2003).

[23] J. Sun *et al.*, ChemPhysChem **6**, 2458 (2005).

[24] K. D. Hermanson *et al.*, Science **201**, 1082 (2001).

[25] S. R. L, and T. R. I, Inf. Display (New Display Technologies Section) (1996).

[26] T. Li, T. Kido, and J. H. Adair, Proceedings of the Ninth IEEE International Symposium (1994).

[27] E. M. Korenic *et al.*, Mol. Cryst. Liq. Cryst. **317**, 197 (1998).

[28] Y. M. Shkel, G. H. Kim, and R. E. Rowlands, International Symposium on Experimental Mechanics (2002).

[29] D. L. Fan *et al.*, Phys. Rev. Lett. **94**, 247208 (2005).

[30] X. Li, and R. J. L. Zhang, Polym. Adv. Technol. **10**, 90 (1999).

[31] J. H. Park, Y. T. Lim, and O. O. Park, Mac. Rap. Comm. **22**, 616 (2001).

[32] A. P. Alivisatos, Science **271**, 933 (1996).

[33] S. A. Maier, Nat. Mater. **2**, 229 (2003).

[34] J. Hoinville, J. Appl. Phys. **93**, 7187 (2003).

[35] X. J. Huang *et al.*, Nanotechnology **17**, 2988 (2006).

[36] M. Tanase *et al.*, J. Appl. Phys. **91**, 8549 (2002).

[37] W. Salalha, and E. Zussman, Phys. Fluids **17**, 063301 (2005).

[38] R. A. Richard *et al.*, J. Microelectromechanical systems **12**, 387 (2003).

[39] W. Lu, and D. Salac, Phys. Rev. Lett. **94**, 146103 (2005).

[40] W. Lu, H. Koerner, and R. Vaia, Appl. Phys. Lett. **89**, 223118 (2006).

[41] J. Park, and W. Lu, Appl. Phys. Lett. **91**, 053113 (2007).

[42] M. Parthasarathy, and D. J. Klingenberg, Mat. Sci. Eng. **R17**, 57 (1996).

[43] H. Zeng *et al.*, Nature **420**, 395 (2002).

[44] J. R. Baker *et al.*, Biomed. Microdevices **3**, 61 (2001).

[45] N. Malik, E. G. Evagorou, and R. Duncan, Anti-Cancer Drugs **10**, 767 (1999).

[46] T. P. Thomas, I. J. Majoros, and A. Kotlyar, J. Med. Chem **48**, 3729 (2005).

[47] I. J. Majoros *et al.*, J. Med. Chem **48**, 5892 (2005).

[48] S. Hong *et al.*, Chemistry and Biology **14**, 107 (2007).

[49] I. H. E. Sayed, X. Huang, and M. A. El-Sayed, Nano Lett. **5**, 829 (2005).

[50] A. Nel, T. Xia, and L. Madler, Scinece **311**, 622 (2006).

[51] N. Karoonuthaisiri, K. Titiyevskiy, and J. L. Thomas, Colloids Surf. B **27**, 365 (2003).

[52] M. F. Ottaviani *et al.*, Langmuir **18**, 2347 (2002).

[53] S. Hong *et al.*, Bioconj. Chem **15**, 774 (2004).

[54] S. Hong *et al.*, Bioconj. Chem **17**, 728 (2006).

[55] A. Mecke *et al.*, Chem. Phys. Lipids **132**, 3 (2004).

[56] A. Mecke *et al.*, Langmuir **21**, 10348 (2005).

[57] F. Vinet, P. Chaton, and F. Fouillet, Microelectronic Engineering **41**, 61 (2002).

[58] P. Gwynne, and G. Heebner, Science **298**, 5593 (2002).

[59] T. H. Cehn *et al.*, J. Micromech. Microeng. **17**, 489 (2007).

[60] A. Klinger, and F. Mugele, J. Appl. Phys. **95**, 2918 (2003).

[61] S. Kuiper, and B. H. W. Hendriks, Appl. Phys. Lett. **85**, 1128 (2004).

[62] B. Berge, and J. Peseux, Eur. Phys. J. E **3**, 159 (2000).

[63] S. Yang *et al.*, Adv. Mater. **15**, 940 (2003).

[64] R. A. Hayes, and B. J. Feenstra, Nature **425**, 383 (2003).

[65] C. Petrie, J. Non-Newtonian Fluid Mech. **87**, 369 (1999).

[66] R. R. A. Syms *et al.*, J. Microelectromechanical systems **12**, 387 (2003).

[67] V. I. Merkulov *et al.*, Appl. Phys. Lett. **80**, 4816 (2002).

[68] T. B. Jones, *Electromechanics of Particles* Cambridge, New York, 1995).

[69] G. Kim, and Y. M. Shkel, J. Mater. Res. **19**, 1164 (2004).

[70] H.-Y. Hsu *et al.*, Nanotechnology **16**, 312 (2005).

[71] Stratton, *Electromagnetic theory* New York and London, 1941).

[72] A. A. Teixeia-Pinto *et al.*, Experi. Cell. Res. **20**, 548 (1960).

[73] G. Schwarz, M. Saito, and H. P. Schwan, J. Chem. Phys. **43**, 3562 (1965).

[74] M. Saito, H. P. Schwan, and G. Schwarz, Biophy. J. **6**, 313 (1966).

[75] L. Landau, and E. Lifshitz, *Electrodynamics of Continuous Media* (Pergamon Press, Oxford, U.K., New York, 1960).

[76] F. A. Sauer, *Coherent Excitations in Biological Systems* (Springer, Berlin, 1983), p. 134.

[77] A. D. Gruzdev, Biophysics **10**, 1206 (1965).

[78] X. Wang, X.-B. Wang, and P. R. C. Gascoyne, J. Electrostatics **39**, 277 (1997).

[79] Y. Wang, R. N. Dave, and R. Pfeffer, J. of Supercritical Fluids **28**, 85 (2004).

[80] M. Kao, A. Yodh, and D. Pine, Phys. Rev. Lett **70**, 242 (1993).

[81] J. J. Newman, and R. B. Yarbrough, J. Appl. Phys. **39**, 5566 (1968).

[82] R. B. Bird, R. C. Armstrong, and O. Hassager, *Dynamics of Polymeric Liquid* (Wiley, New York, 1977).

[83] M. Doi, *The theory of polymer dynamics* (Oxford University Press Inc., Newyork, 2001).

[84] R. Tao, and J. M. Sun, Phys. Rev. Lett. **67**, 398 (1991).

[85] R. Tao, and Q. Jiang, Phys. Rev. Lett. **73**, 205 (1994).

[86] T. Chen, R. N. Zitter, and R. Tao, Phys. Rev. Lett. **68**, 2555 (1992).

[87] A. Hynninen, and M. Dijkstra, Phys. Rev. E **72**, 051402 (2005).

[88] M. P. Allen, and D. J. Tildesley, *Computer simulation of liquids* (Clarendon Press, Oxford, 1987).

[89] D. Frenkel, and B. Smit, *Understanding Molecular Simulation* (Academic Press, San Diego, 2002).

[90] J. J. Urban *et al.*, J. Am. Chem. Soc. **128**, 3248 (2006).

[91] J. D. Jackson, *Classical Electrodynamics* (John Wiley & Sons, Inc., New York, 1999).

[92] P. J. Bond, and M. S. P. Sansom, J. Am. Chem. Soc **128**, 2697 (2006).

[93] P. K. Maiti *et al.*, Macromolecules **38**, 979 (2005).

[94] H. Lee, and R. G. Larson, J. Phys. Chem. B **110**, 18204 (2006).

[95] W. Lu, and Z. Suo, J. Mech. Phys. Solids **49**, 1937 (2001).

[96] D. Kim, and W. Lu, Phys. Rev. B **73**, 035206 (2006).

[97] Q. Du, C. Liu, and X. Wang, J. Comp. Phys. **198**, 450 (2004).

[98] N. Saunders, and A. P. Miodounik, *CALPHAD (Calculation of Phase Diagram): A Comprehensive Guide* (Pergamon Press, New York, 1998).

[99] W. Helfrich, Z. Naturforsch. C **28**, 693 (1973).

[100] X. Wang, Ph. D. Thesis, The Pennsylvania State University (2005).

[101] J. W. Cahn, and J. E. Hilliard, J Chem Phys **28**, 258 (1958).

[102] L.-Q. Chen, and J. Shen, Comp. Phys. Commun. **108**, 147 (1998).

[103] J. Zhu, L. Q. Chen, and J. Shen, Phys. Rev. E **60**, 3564 (1999).

[104] U. M. Ascher *et al*., SIAM (Soc. Ind. Appl. Math) J. Numer. Anal. **32**, 797 (1995).

[105] J. W. Cahn, and J. E. Hilliard, J. Chem. Phys. **28**, 258 (1958).

[106] R. C. Triulzi *et al.*, Analyst **133**, 667 (2008).

[107] J. Henin, and C. Chipot, Chem. Phys. Lett. **425**, 329 (2006).

[108] E. Evans, and W. Rawics, Phys. Rev. Lett. **64**, 2094 (1990).

[109] M. F. Ottaviani *et al.*, J. Phys. Chem. **100**, 11033 (1996).

[110] R. C. v. Djijvenbode, M. Borkovec, and G. J. M. Koper, Polymer **39**, 2657 (1998).

[111] E. C. Mbamala, A. B. Shaul, and S. May, Biophysical J. **88**, 1702 (2005).

[112] G. Lippmann, Ann. Chim. Phys. **5**, 494 (1875).

[113] B. Berge, C. R. Acad. Sci **317**, 157 (1993).

[114] M. Vallet, M. Vallade, and B. Berge, Eur. Phys. J. B **11**, 583 (1999).

[115] H. J. J. Verheijen, and M. W. J. Prins, Langmuir **15**, 6616 (1999).

[116] B. Shapiro *et al.*, J. Appl. Phys. **93**, 5794 (2003).

[117] V. Peykov, A. Quinn, and J. Ralston, Colloid Polym. Sci **278**, 789 (2000).

[118] W. J. J. Welters, and L. G. Fokkink, Langmuir **14**, 1535 (1998).

[119] J. A. M. Sondag-Huethorst, and L. G. Fokkink, Langmuir **10**, 4380 (1994).

[120] T. B. Jones, Langmuir **18**, 4437 (2002).

[121] T. B. Jones *et al.*, Langmuir **19**, 7646 (2003).

[122] J. Zeng, and T. Korsmeyer, Lab Chip **4**, 265 (2004).

[123] F. Mugele, and S. Herminghaus.

[124] W. Lu, and D. Kim, Appl. Phys. Lett. **88**, 153116 (2006).

[125] A. Staicu, and F. Mugele, Phys. Rev. Lett. **97**, 167801 (2006).

[126] S. Vafaei, and M. Z. Podowski, Nuclear Eng. and Design **235**, 1293 (2005).

[127] R. Baviere, J. Boutet, and Y. Fouillet, Microfluid Nanofluid **4**, 287 (2008).

[128] M. J. d. Ruijter, T. D. Blake, and J. D. Coninck, Langmuir **15**, 7836 (1999).

[129] K. H. Kang, Langmuir **18**, 10318 (2002).

[130] J. F. Joanny, and P. G. d. Gennes, J. Chem. Phys. **81**, 552 (1984).

[131] M. O. Robbins, and J. F. Joanny, Europhys. Lett **3**, 729 (1987).